Freezing of droplets under mixed-phase cloud conditions

James David Atkinson

Submitted in accordance with the requirements for the degree of
Doctor of Philosophy

The University of Leeds

School of Earth and Environment

December, 2013

The candidate confirms that the work submitted is his own, except where work which has formed part of jointly-authored publications has been included. The contribution of the candidate and the other authors to this work has been explicitly indicated overleaf. The candidate confirms that appropriate credit has been given within the thesis where reference has been made to the work of others.

Summary of the author's contribution to published work

(Chapter 7) Murray, B.J., D. O'Sullivan, D., J.D. Atkinson and M. E. Webb, *Ice nucleation by particles immersed in supercooled cloud droplets*. Chem. Soc. Rev., **41**, 6519-6554, doi:10.1039/C2CS35200A, 2012.

JDA assisted with the writing of the manuscript, taking the lead on the Mineral dust nuclei section. BJM was lead author of the manuscript, with assistance from DOS. DOS led the Biological nuclei section with assistance from MEW.

(Chapter 7) Atkinson, J.D., B.J. Murray, M.T. Woodhouse, T.F. Whale, K.J. Baustian, K.S. Carslaw, S. Dobbie, D. O'Sullivan, and T.L. Malkin, *The importance of feldspar for ice nucleation by mineral dust in mixed-phase clouds.* Nature, 2013. **498**(7454): p. 355-358, doi: 10.1038/nature12278.

JDA wrote the manuscript, planned and performed picolitre experiments, acquired the minerals and direct their characterisation, and assisted with planning the modelling study. BJM acquired financial support for the project and oversaw it with assistance from SD the study. MTW planned and performed the modelling study. TFW assisted with developing the microlitre instrument in collaboration with DOS, and performed the microlitre experiments. KJB assisted with experiments. KSC oversaw the modelling study. TLM performed XRD of the mineral samples.

Acknowledgements

I would like to thank many people for their support during this project. Without them, I wouldn't have got through. I would specifically like to thank my supervisors Ben Murray and Steve Dobbie for their direction and support. I would also like to thank everyone who has helped at some point during this project from the inside of the research group: Tamsin Malkin, Sarah Broadley, Theo Wilson, Ross Herbert, Danny O'Sullivan, Sam Peppe, Nsikanabasi Umo, Tom Whale, Kelly Baustian, Hannah Price and Tom Mangan.

There are a number of people who haven't been able to come up with excuses to get away from me during this project: Becky for being patient, impatient, calm, worried, and loving and always supportive, I couldn't have done it without you; Mum and Dad for pretending to understand what I was doing and always willing to have us round for a chat no matter how short the notice; the lizards for deciding in the end that I'm not edible; Becky's family for their patient interest and freely given support especially in the time leading up to the start of my PhD; and anyone who shared office 10.128 with me and couldn't find a desk somewhere else.

I would also like to thank various people in the university for their contribution while I've been there the people that the School of Earth and Environment paid to put up with me, specifically Sam Allshorn, Michelle Lesnianski, Tony Windross, Jim McQuaid for his Northern hospitality, Ken Carslaw for his patience, everyone in reception for supplying near constant tea and milk, and Richard Rigby for helping me even though I am one of those windows lot. Thanks also to the helpful people over in Chemistry who put up with my bumbling, specifically Dave Fogarty, Andy Goddard and the staff at the workshops and stores.

Everyone at ICAS football must be thanked for letting me kick them without excessive recriminations, as well as the 11am coffee gang, and everyone at Archery for putting up with me and giving me something else to think about, especially Andy Arnold for his fellow-Northernerness and patience in the face of my ineptness, and everyone who was on the committee with me.

I would like to thank Ulrike, Berko and Zamin at ETH Zürich for turning stress into motivation for this last month by offering me a job. I am also very grateful to the European Research Council for providing the grant funding that paid my stipend.

Abstract

Mixed-phase clouds contain both liquid and ice particles. They have important roles in weather and climate and such clouds are thought to be responsible for a large proportion of precipitation. Their lifetime and precipitation rates are sensitive to the concentration of ice. This project focuses upon the formation of ice within clouds containing liquid droplets colder than 273 K. A new bench-top instrument has been developed to study ice nucleation in liquid droplets.

Pure water droplets of sizes relevant to clouds in the lower atmosphere do not freeze homogeneously until temperatures below ~237 K are reached. However, literature measurements of nucleation rates are scattered over two kelvin and there is uncertainty over the actual mechanism of ice formation in small droplets. The freezing of droplets with diameters equivalent to ~4 – 17 μm has been observed. It was found that ice nucleation rates in the smallest droplets of this size range were consistent with nucleation due to the droplet surface, but that surface nucleation does not occur at fast enough rates to be significant in the majority of tropospheric clouds.

Water droplets can be frozen at higher temperatures than relevant for homogeneous freezing due to the presence of a class of aerosol particles called ice nuclei. Field observations of ice crystal residues have shown that mineral dust particles are an important group of ice nuclei, and the ice nucleating ability of seven of the most common minerals found in atmospheric dust has been described. In comparison to the other minerals, it was found that the mineral K-feldspar is much more efficient at nucleating ice. To relate this result to the atmosphere, a global chemical and aerosol transport modelling study was performed. This study concluded that dust containing feldspar emitted from desert regions reaches all locations around the globe. At temperatures below ~255 K, the modelled concentration of feldspar is sufficient to explain field observations of ice nuclei concentrations.

Contents

List of tables

List of figures

List of abbreviations

Abbreviation	Meaning
ATD	Arizona Test Dust
BET	Brunauer, Emmett and Teller method of measuring the specific surface area of a powder
CA	The mineral calcite
CCN	Cloud Condensation Nuclei
CFDC	Continous Flow Diffusion Chamber
CH	The mineral chlorite
cm	Constant Mean
ic	Cubic ice 1
ih	Hexagonal ice 1
IL	The mineral illite
IPCC	Intergovernmental Panel on Climate Change
I-S	Illlite - Smectite mixed layer clay
isd	Stacking-disordered ice 1
KA	The mineral kaolinite
KF	The mineral K-feldspar
MCS	Multiple Component Stochastic ice nucleation model
MI	The mineral mica
MO	The mineral montmorillonite
NCF	The sodium-calcium group of feldspar minerals
ND	Not Detected (in an XRD spectra)
OT	Other minerals
PRT	platinum resistance thermometer
QU	The mineral quartz
RH	Relative Humidity
RH_{ice}	Relative Humidity with respect to ice
RH_{liq}	Relative Humidity with respect to liquid water
RMS	Root-Mean-Square
S	Water vapour Saturation
SA	Surface Area
S_{ice}	Water vapour Saturation with respect to ice
S_{liq}	Water vapour Saturation with respect to liquid water
SSA	Specific Surface Area, for example measured by BET
Tsp.	Transported; denoting observations of atmospheric mineral dust which have been transported a distance from source
um	Updating Mean
XRD	X-Ray Diffraction

Chapter 1. Introduction

The weather and climate are subjects of great interest to society and the ability to predict the weather is of general importance to the public. For example, weather forecasts on all time scales are financially significant for industries such as retail[1], agriculture[2], insurance[3] and energy[4]. It also impacts upon personal safety in the form of preparedness, immediate response and policy making to deal with extreme events such as droughts, heat waves, flooding and wind storms[5]. As well as predicting day-to-day and month-to-month weather, understanding the processes occurring in the atmosphere is essential for predicting future climate.

The main force driving weather and climate is the flow of energy around the atmosphere[6]. Solar radiation enters at the top of the atmosphere (Figure 1.1), with a large portion passing through to heat the surface at the bottom of the atmosphere. The warmed surface emits energy upwards in the form of infra-red radiation, the majority of which is absorbed by the atmosphere. Additional heat transfer from the surface to the atmosphere occurs through the upwards movement of warm air and water vapour. The atmosphere emits the absorbed energy as infra-red radiation, both toward the surface and out to space.

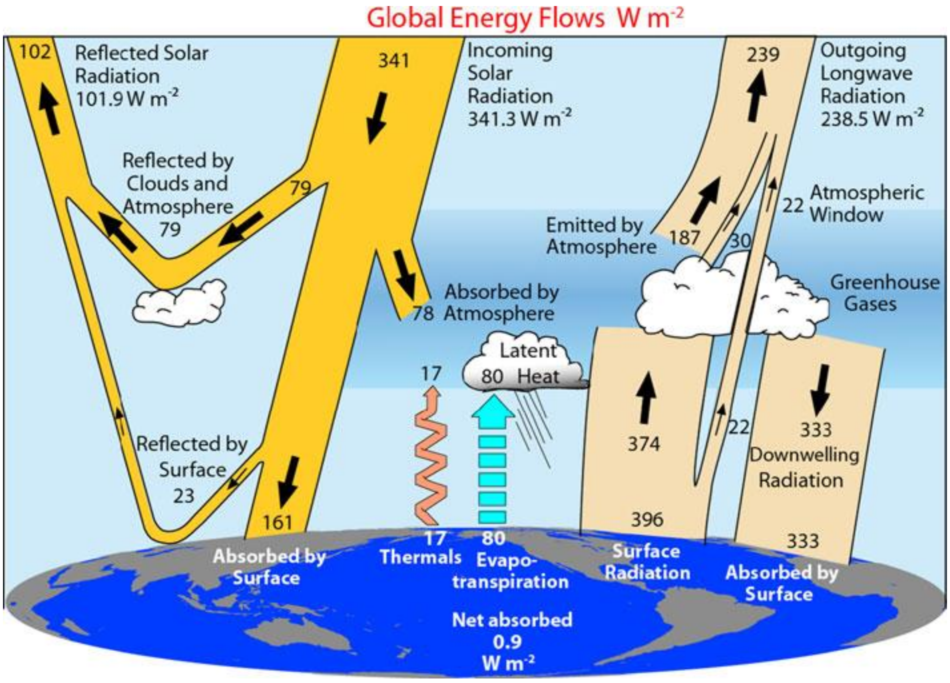

Figure 1.1. An estimation of the flow of energy around the Earth's atmosphere. Shown are globally and annually averaged energy flows, given in W m^{-2}. The top third of the chart represents energy flows through the top of the atmosphere, the middle third flows within the atmosphere, and the bottom third at the surface. The left half of the chart deals with solar radiation, the right with terrestrial radiation. From Trenberth and Fasullo[7].

By comparing the incoming and outgoing radiation, any energy imbalance can be estimated, potentially warming the planet and causing climate change. From the measurements in Figure 1.1 the difference between incoming and outgoing radiation at the top of the atmosphere was estimated to be 0.9 ±0.5 W m^{-2} (ref [7]). However, the uncertainties in estimations of the energy transfers in the rest of the atmosphere are significant. For example, Trenberth and Fasullo[7] estimated an uncertainty of ±14 W m^{-2} within the components of the hydrological cycle, due to a lack of direct measurements of elements such as surface evaporation. The change to the energy balance caused by perturbations to the atmosphere occurring since 1750 was estimated in the fourth Intergovernmental Panel on Climate Change (IPCC) report[8] at 1.6 (+0.8 -1.0) W m^{-2} (Figure 1.2). The report's conclusion was that the climate is warming and that it is 'extremely likely' that human activities are responsible for the majority of change[8].

These estimations give the global average energy flow in and out of the atmosphere. This average represents a homogeneous surface devoid of features such as oceans, mountains, fields and forests, and without variations in solar radiation due to the curvature of the Earth.

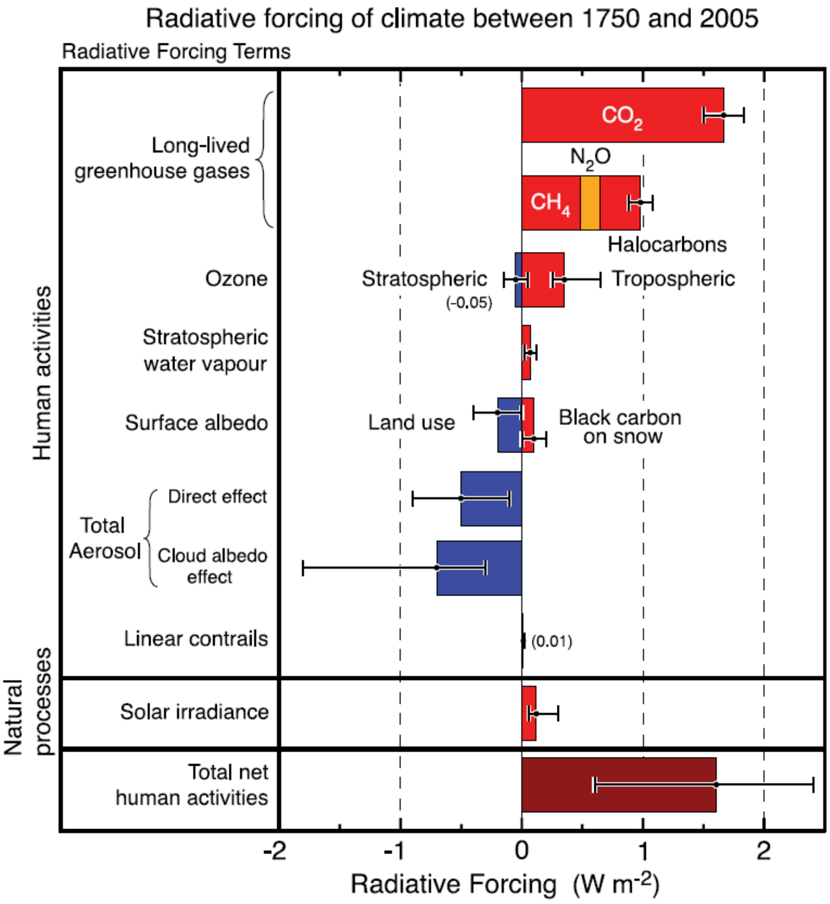

Figure 1.2. An estimation of the radiative forcing upon the climate by various effects, in W m^{-2}. The sources listed give the radiative forcing due to the change in that quantity, for example the CO_2 forcing is from the increase in CO_2 levels due to human activity, rather than the absolute CO_2 level. Taken from Chapter two of Working Group 1 of the fourth IPCC report[8].

The differences in surface heating rates due to these features, along with Earth's rotation, cause real world weather and climate patterns[6]. If a parcel of air is lifted upwards it cools due to expansion and after sufficient cooling water will condense from the air, forming clouds[9].

Clouds form an integral part of the climate system. As well as being responsible for precipitation[6,9], clouds and cloud processes have significant roles in the flow of energy in the atmosphere[7]. They scatter significant amounts of solar radiation back to space and are a major absorber/emitter of infra-red radiation in the lower atmosphere (for example see Ramanathan *et al.*[10] and Hartmann *et al.*[11]). Through this clouds directly influence surface temperatures, and through water transport and precipitation complete the hydrological cycle[12]. Therefore, to predict future climate trends and accurately forecast the weather and extreme events it is essential to understand the physics of clouds.

One of the main factors influencing the radiative impact of a cloud is the number and size of the particles it is made of - liquid droplets[13] and ice crystals[14]. These factors also influence the lifetime and extent of clouds, mainly through precipitation (section 2.2). While the mass of water in a cloud depends upon atmospheric conditions (e.g. ref [15]), the concentration of cloud droplets is closely related to the number of aerosol particles within the cloud which provide a nucleus for condensation[9]. These cloud condensation nuclei (CCN) include industrial pollution[16], dust[17,18], smoke[19], sea salt[20], volcanic particles[21] and organic particles from sources such as vegetation[22]. Clouds with many of these particles will contain larger numbers of small droplets and as smaller droplets have a higher surface area to volume ratio, such clouds are optically thicker with enhanced effects upon radiation[13]. Smaller droplets are also less efficient at forming precipitation and thus tend to have a longer atmospheric lifetime[23] (see section 2.2.2).

Human activities have changed, and continue to change, the amount of aerosol in the atmosphere[24], which has a cooling effect upon the atmosphere[8]. In Figure 1.2 there are two entries for aerosols: the direct effects of aerosol particles upon radiative transfer by scattering solar radiation to space and the varied 'indirect' effects aerosol has upon clouds (see Section 2.2), which include changes to precipitation. However, the uncertainty in this second radiative forcing was significant enough for the authors of the fourth assessment report of the IPCC to declare that[8]:

> *"only the aerosol interaction in the context of liquid water clouds is assessed, with knowledge of the interaction with ice clouds deemed insufficient."*

An important effect of aerosol upon the ice content of clouds is the called the Glaciation indirect effect[25], in which aerosol particles trigger the formation of ice. This effect is possible as pure water droplets of sizes typical to clouds (~5 – 20 μm diameter[26,27]) typically freeze at 237 K and below[28,29]. A sub-set of the aerosol, referred to as ice nuclei, can catalyse freezing, increasing the temperature at which ice can form[30,31]. Ice nuclei can have a strong impact upon precipitation[32], and hence the lifetime of clouds (section 2.2).

There are several different aerosol types known to be atmospherically relevant ice nuclei, such as volcanic ash, mineral dusts, soot and biological particles including bacteria[30,31], and a large proportion of nuclei are thought to be due to mineral dusts (**Error! Reference source not found.** and refs [33-36]). However, prior to the present study, of the eight most common minerals in the atmosphere only kaolinite, representing ~10 % of atmospheric dust (see Chapter 7), has been studied in detail[30,31] (i.e. sample composition/purity and surface area quantified as well as ice nucleating behaviour). As minerals have been shown to freeze at temperatures at least as high as 258 K[37] with considerable variability between different minerals[30,31,38-40] and between different samples of the same mineral[40-42], accurate modelling and prediction will be difficult without such a detailed study.

To adequately describe the nucleating ability of substances that are not efficient ice nuclei, as well as to accurately describe freezing in clouds which do not contain significant ice nuclei[43], it is necessary to have an accurate understanding of the freezing of pure water. However, the current certainty in measurement of homogeneous freezing nucleation rates is poor, with literature nucleation rate coefficients scattered over a range of two Kelvin and three orders of magnitude[28]. Even the exact mechanism through which ice nucleates homogeneously is in question[44-46].

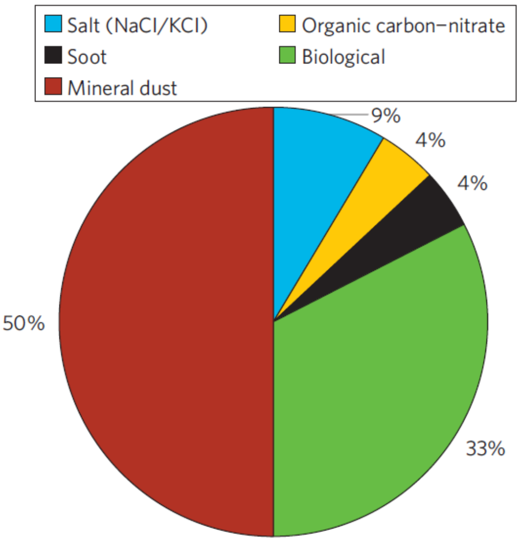

Figure 1.3. Classification of the main component of ice nuclei observed in a layer cloud over central USA. Ice nuclei were collected at an altitude of 8.3 – 8.7 km and measured using a continuous flow diffusion chamber (CFDC) operating at 242 – 239 K, with ice residues identified using aerosol time of flight mass spectrometry. From Pratt *et al.*[33].

A cold stage instrument for the investigation of ice nucleation has been used recently to study the freezing of pure water[29] and nucleation by different minerals[41,47]. However, to increase the accuracy of the study of ice nucleation, especially homogeneous nucleation, improvements in temperature measurement and control are necessary, as well as the ability to measure ice nucleation by smaller droplets.

1.1.Project objectives

Knowledge of how cloud droplets freeze is important for the accurate prediction of weather and climate, but our understanding of ice nucleation by some of the common atmospheric aerosol types is limited. The main objectives of this project are to improve that understanding through the following aims:

1. A) Develop the second generation of an existing bench-top instrument capable of measuring the nucleation of ice by pure water and droplets containing various atmospherically relevant species immersed in water droplets.

   B) Concurrently improve the statistical treatment of freezing data to produce more accurate nucleation coefficients.
2. Accurately determine the freezing behaviour of pure water droplets, to enable the description of low-efficiency ice nuclei and to test the hypothesis that nucleation at the droplet surface is responsible for freezing in small water droplets.
3. Acquire and characterise samples of the most common minerals found within atmospheric mineral dust and determine the ice nucleating ability of these minerals when immersed in water, to answer the question ‘does one mineral dominate ice nucleation by mineral dusts?’. If the result of this question is true, this may be able to provide a simple representation of ice nucleation by mineral dusts.

Chapter 2 provides an in-depth exploration of the background to this project. Chapter 3 then completes aim 1A by providing a detailed description of the second generation experimental equipment and updated processes, followed by Chapter 4, detailing the analysis of freezing data (aim 1B). Chapter 5 completes the description of the experimental process, covering the characterisation of mineral samples required for aim 3. Chapter 6 is an investigation into homogeneous nucleation, utilising the ability of the new equipment to observe freezing in droplets less than 10 μm diameter to test the droplet surface nucleation hypothesis in aim 2. Description of the ice-nucleating ability of a range of minerals common to the atmosphere is provided within Chapter 7, answering the question of mineral dominance in aim 3. The thesis culminates with a summary and important conclusions of the project.

Chapter 2. Background

Liquid clouds form when a parcel of air has a water vapour concentration sufficiently high to cause the condensation of excess water vapour[9]. Precisely how much excess water vapour is required depends upon the air temperature and the characteristics and concentration of CCN present for nucleating the condensation of liquid droplets[9] (section 2.2.2). This means that the number and size distribution of the resulting cloud droplets are controlled by the CCN concentration and the amount of excess water vapour in the air parcel. Some of these CCN, as well as other non-CCN aerosol particles in the cloud, may then initiate the freezing of cloud droplets[30,31]. In mixed-phase clouds, these ice particles grow as mass is transferred from liquid droplets to the ice crystals, as the equilibrium vapour pressure of liquid water is greater than that of ice (e.g. ref [32]). As ice nuclei are relatively rare in comparison to the number of CCN[48], at the time of freezing there is often sufficient liquid available for ice particles to grow large enough to fall from the cloud. These falling ice crystals then either evaporate below the cloud or reach the surface as liquid or ice precipitation. This ice-initiated precipitation is generally referred to as cold rain, whereas rain which has not resulted from the freezing of water is sometimes referred to as warm rain[9]. While the formation of ice is not a pre-requisite, precipitation due to freezing is frequent especially at higher latitudes[49,50]. As a precipitating cloud will generally have a shorter lifetime than a similar sized non-precipitating cloud[14], the initiation of the ice phase can have important consequences for the local and global radiation budget.

2.1. Atmospheric Water

Although the boiling point of water at standard atmospheric pressure is ~373 K, at temperatures below this water vapour is still present in air, tending to form an equilibrium with any liquid or ice present. The partial pressure of water vapour at equilibrium with a flat liquid or ice surface, referred to as the saturation vapour pressure, is different for ice and liquid and strongly depends upon temperature. Liquid water has a higher saturation vapour pressure than ice, and higher temperatures correspond to higher saturation vapour pressures. Equation 2.1 and 2.2 are parameterisations of the saturation vapour pressures over flat liquid and ice surfaces respectively, derived from experimental data[51]:

$$\begin{aligned}\ln(p_{\mathrm{liq}}) \approx\ & 54.842763 - \frac{6763.22}{T} \\ & - 4.210\ln(T) + 0.000367T \\ & + (\tanh\{0.0415(T - 218.8)\})\Big(53.878 \\ & - \frac{1331.22}{T} - 9.44523\ln(T) + 0.14025T\Big)\end{aligned}$$

Equation 2.1

$$\begin{aligned}\ln(p_{\mathrm{ice}}) =\ & 9.550426 - \frac{5723.265}{T} + 3.53068\ln(T) \\ & - 0.00728332T\end{aligned}$$

Equation 2.2

In a closed system at steady state the partial pressure of water vapour, or humidity, in the air will be the same as the saturation vapour pressure. However, in open and non-steady state systems equilibrium between the different phases of water is rarely reached. Such systems can be as simple as an open beaker of water, a sealed vessel containing both ice and liquid, or as complex as the Earth's atmosphere. The actual humidity in the atmosphere is usually at or below saturation, but is occasionally also above saturation. However, due to the dependence of the saturation vapour pressure upon temperature, knowing the absolute vapour pressure of an air parcel is not sufficient to describe conditions and it is often more convenient to use the ratio of the actual humidity to the saturation vapour pressure[6]. This ratio can be expressed as a percentage (relative humidity, RH) or a decimal (saturation, S, where $S = 1$ is equivalent to $RH = 100\%$) and depends upon whether it is with respect to the liquid or solid phase of water.

If $S \geq 1$ the formation of liquid droplets and/or ice particles is possible. A frequent mechanism that produces a high relative humidity is to cool a parcel of air, typically due to adiabatic expansion during lifting[9]. This lifting can be caused by flow over surface features such as mountains, or due to updrafts caused by heating air at a location. In atmospherically relevant time scales and conditions, the formation of liquid droplets in particle free air requires $S_{\mathrm{liq}} > \sim3$ and ice particles $S_{\mathrm{ice}} > \sim15$ (ref [9]). Droplets and ice can form at lower humidities than these if aerosol particles, referred to as nuclei, are present[9].

2.2. Aerosol-cloud interactions

The radiative impact of a cloud and the amount and timing of precipitation depend upon the mass of water in the cloud, how that mass is distributed between the ice and liquid phases, and the droplet/ice crystal size distributions. It is also related to the cloud's optical thickness, which can be conceptually viewed as being proportional to the sum of the cross-sections of the droplets/crystals the cloud is made of, the number and phase of which is largely controlled by the type and concentration of aerosol particles present. The ability and concentration of these particles increases with cooling and at higher humidities[9]. If the number of cloud particles were to increase with no change to the mass of the cloud, the total cross-section and optical thickness of the cloud will increase[13]. Likewise, as precipitation requires cloud particles that are large enough to fall from the cloud, a reduction in the average cloud particle size will reduce precipitation[23]. As previously described, the presence of ice within a cloud also strongly influences precipitation via the cold rain process[32].

2.2.1. Warm and cold rain

Precipitation can be categorised dependent upon the presence of ice within the cloud[9]: warm rain, cold rain, and ice precipitation. Warm rain is liquid precipitation formed without the formation of ice at any point[9,49], whereas ice precipitation, such as snow, hail and graupel, is caused by freezing within the cloud[9]. Cold rain is ice precipitation which has melted before reaching the observer[52].

If an air parcel super-saturated with respect to liquid already contains liquid, the droplets will attempt to reach equilibrium with the surrounding air by reducing the water vapour pressure through condensation[9]. However, growth by condensation rarely produces droplets large enough to result in precipitation and such droplets typically form by droplets colliding and coalescing[9]. Precipitation is also initiated by the freezing of droplets.

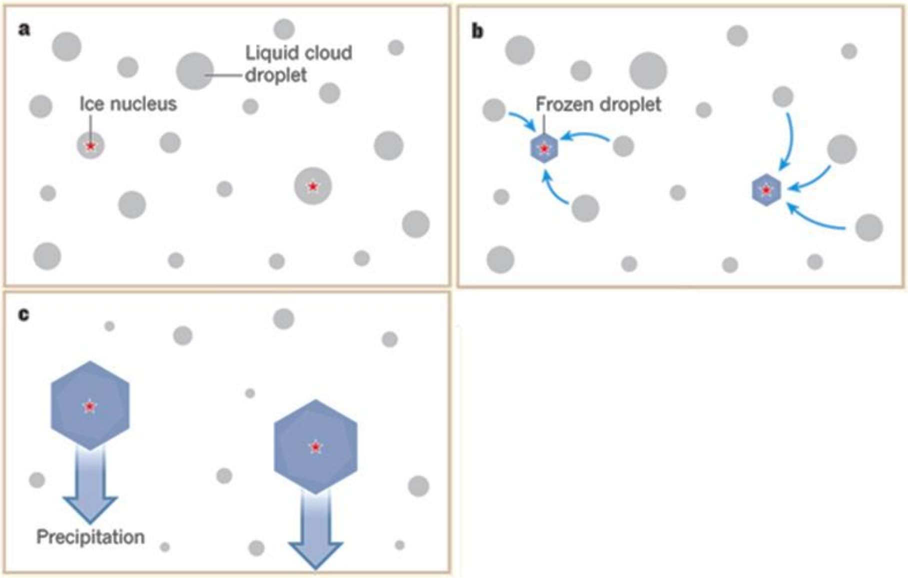

Figure 2.1. Schematic of the formation of precipitation by the Bergeron-Findeisen process. A) The presence of relatively rare ice nuclei results in the freezing of a minority of drops. B) Mass is then transferred from the droplets to the ice crystals via the vapour phase. C) The resultant large ice crystals then fall from the cloud. From Koop and Mahowald[53].

When a few droplets freeze, they will rapidly grow by the transfer of mass from the many liquid droplets to the few ice crystals via the Bergeron-Findeisen process[32,53], often called cold rain (Figure 2.1). This transfer arises from the different saturation vapour pressures over liquid and ice surfaces which are at the same temperature.

The relative global importance of warm and cold rain is difficult to estimate. Using satellite estimations of rainfall along with an estimation of cloud temperature, cold rain has been suggested to be responsible for ~70 % of rain in the tropics[49]. Observations made during a period in 2011, showed that in two-thirds of Californian winter storms precipitation due to warm rain was either in the minority or undetectable[50]. It was also estimated during this study that 74 % of all precipitation was due to ice processes, but the absence of significant warm rain may have been due to low cloud top temperatures which in all but one case were below ~255 K (ref [50]). These observations suggest that cold rain is an important mechanism for producing precipitation and as such is worthy of further study.

2.2.2. Cloud condensation nuclei

The majority of CCN are partially or wholly water soluble[9]. These particle’s ability to act as CCN is approximated by the combination of Raoult’s law and the Kelvin effect[9,54,55]. While insoluble particles can also act as CCN, they tend to be less efficient[9]. For example, the CCN activity of some mineral dusts is only comparable to that of soluble aerosol if the dust if it has reacted with atmospheric trace gases[17] or contains a soluble component[18].

CCN can originate from natural or anthropogenic sources. Notable CCN types include sea salt, some mineral dusts, organic particles usually originating from vegetation and pollution, sulphate particles due to volcanic eruptions and pollution, and soot particles originating from biomass burning and fuel burning[55]. Increases to the concentration of CCN, mainly due to anthropogenic activity, effect clouds through several mechanisms[8] (Figure 2.2).

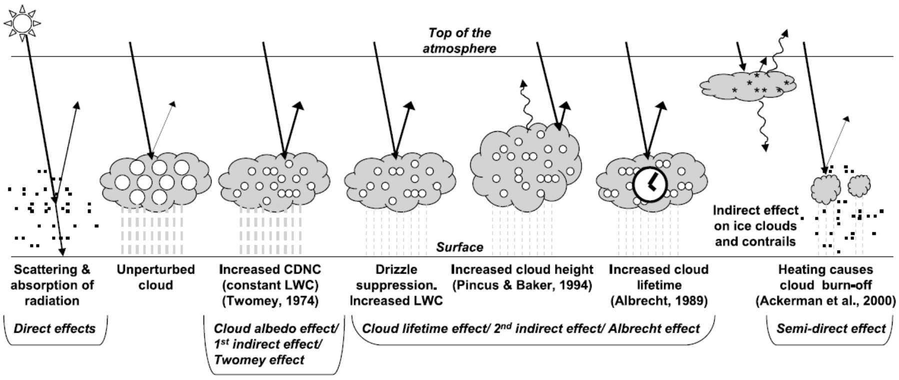

Figure 2.2. The direct and indirect effects of aerosol interactions with liquid clouds. Taken from Chapter two of Working Group 1 of the fourth IPCC report[8].

Adding CCN to a cloud will result in higher concentrations of droplets with a smaller mean size, increasing the scattering of solar radiation and absorption of terrestrial radiation[13], and reducing the probability of warm rain[23]. Human activities have added CCN to the atmosphere[10]. The effect of these additional CCN on the cloud optical thickness has been estimated to cool the lower atmosphere by an equivalent of -0.7 (-1.1 +0.4) W m^{-2} (ref [8]). For comparison, the effect of anthropogenic emissions of carbon dioxide has been estimated at +1.66 ±0.17 W m^{-2}, with the overall radiative forcing estimated as +1.6 (-1.0 +0.8) W m^{-2} (ref [8]). The radiative impact of the cloud lifetime effects in warm clouds (i.e. due to the suppression of warm rain) has a less certain estimate of -0.3 to -1.4 W m^{-2}, with a corresponding reduction in global mean precipitation of up to 0.13 mm per day[56].

2.2.3. Ice nuclei

At atmospheric pressure, ice will melt at 273.15 K but below this temperature the freezing of water is not necessarily spontaneous. At below 273.15 K liquid water can persist for long periods of time, especially in small volumes such as cloud droplets (~5 – 20 µm diameter). In droplets this size, homogeneous freezing (the freezing of pure water) starts to occur at around 237 K[28,29]. Similarly to cloud condensation nuclei, particles called ice nuclei exist which can be catalyse freezing in a process called heterogeneous nucleation.

2.2.3.1. Homogeneous ice nucleation

In supercooled water there are large numbers of water molecules forming into clusters; which have an ice-like configuration and molecules are constantly leaving and joining these clusters. The change in Gibbs free energy from the formation of an ice-like cluster large enough to be approximated as a sphere is[54,57]:

$$\Delta G_n = \underbrace{4\pi r_n^2 \gamma_{\mathrm{iL}}}_{(1)} - \underbrace{\left(\frac{4\pi r_n^3}{3v}\right)}_{(2)} kT \ln S \qquad \textbf{Equation 2.3}$$

where ΔG_n is the total energy change from the creation of a cluster of n molecules at a temperature T (in K). Term (1) of the right hand side is the energy required to create the ice-liquid surface – the surface area of a sphere of radius r_n multiplied by the ice-liquid surface energy, γ_{iL}. Term (2) is the energy released by bond creation within the volume of the ice cluster, where v is the molecular volume and k the Boltzmann constant. S is the saturation over the ice germ, which for pure water is given by[57]:

$$S = \frac{P_{\mathrm{L}}}{P_{\mathrm{i}}} \qquad \textbf{Equation 2.4}$$

with P_{i} and P_{L} being the saturation vapour pressure over ice over liquid respectively.

P_L is given by Equation 2.1, but calculating P_i is not straight forward. Equation 2.2 gives the vapour pressure over hexagonal ice I, the form of ice most commonly present in nature. However, it has recently been suggested that the phase of ice formed during homogeneous nucleation is cubic ice I rather than hexagonal[29,58]. As vapour pressure measurements for cubic ice at a range of temperatures are not readily available, Murray *et al.*[29] provided a method of conversion between the cubic and hexagonal vapour pressures:

$$\ln\left(\frac{P_{\mathrm{ic}}}{P_{\mathrm{ih}}}\right) = \frac{\Delta G_{\mathrm{h}\rightarrow\mathrm{c}}}{RT} \qquad \textbf{Equation 2.5}$$

where P_{ic} and P_{ih} are the saturation vapour pressures over cubic and hexagonal ice respectively, with P_{ih} specified by Equation 2.2. R is the ideal gas constant and $\Delta G_{\mathrm{h}\rightarrow\mathrm{c}}$ is the change in free energy due to the transformation from hexagonal ice to cubic ice. Measured values of $\Delta G_{\mathrm{h}\rightarrow\mathrm{c}}$ vary between 50.5 and 160 J mol^{-1} (ref [59]), with the different values ascribed to the presence of varying amounts of hexagonal ice in the starting cubic ice[29]. Tanaka and Okabe[60] have shown that the temperature dependence of $\Delta G_{\mathrm{h}\rightarrow\mathrm{c}}$ is small enough to be negligible (~0.1 J mol^{-1} K^{-1}). More recently, work by Malkin *et al.*[61] using X-ray diffraction determined the structure of the ice formed at temperatures relevant to homogeneous nucleation. This work concluded that the phase of ice that nucleates is neither cubic nor hexagonal ice, but a random mixture of cubic and hexagonal layers, which was referred to as stacking-disordered ice I (ref [61]). While Malkin *et al.* did not suggest a more suitable value of $\Delta G_{\mathrm{h}\rightarrow\mathrm{c}}$, its outcome implies that previous works calculating $\Delta G_{\mathrm{h}\rightarrow\mathrm{c}}$ were effectively measuring $\Delta G_{\mathrm{h}\rightarrow\mathrm{sd}}$. As such, in this work $\Delta G_{\mathrm{h}\rightarrow\mathrm{sd}}$ and $\Delta G_{\mathrm{h}\rightarrow\mathrm{c}}$ are assumed to be equivalent; for consistency with the work by Murray *et al.*[29] 155 J mol^{-1} is used.

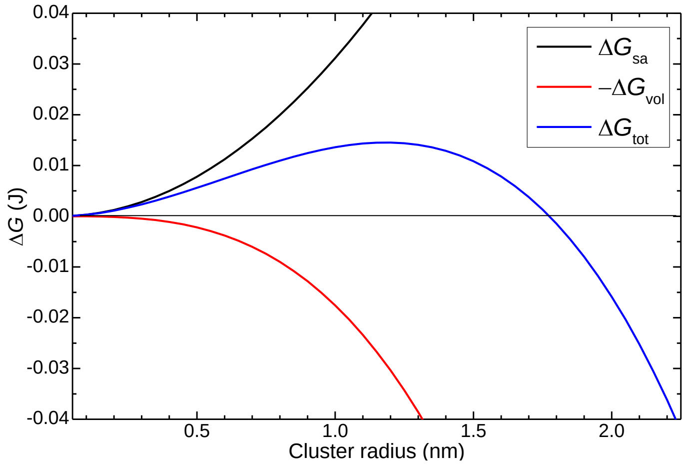

Figure 2.3. A comparison of the surface, volume and total Gibbs free energies for an ice cluster at 237 K. Once the cluster size reaches the maximum ΔG (~1.2 nm at this temperature) the addition of another molecule will cause a release of energy, leading to spontaneous crystal growth. ΔG_{tot} is the left hand side of Equation 2.3 and ΔG_{sa} and $-\Delta G_{\mathrm{vol}}$ are the first and second terms of the right hand side.

In Equation 2.3, the volume and surface terms have different radius dependencies. At very small radii (see Figure 2.3), the absolute volume term is smaller than the surface term. To increase the size of these small clusters energy needs to be added, inhibiting the growth of the ice germ. At every temperature the radius at which the cluster will grow spontaneously can be defined - when the addition of another molecule to the cluster will result in a release of energy. This is when $\mathrm{d}\Delta G/\mathrm{d}r = 0$, and at 237 K this is around 1.2 nm (Figure 2.3). Although the value of ΔG_{tot} is larger than if no cluster existed, at this radii adding another molecule to the cluster reduces ΔG_{tot}. Rearrangements of Equation 2.3 allow calculation of the radius, number of molecules and Gibbs free energy for a cluster where $\mathrm{d}\Delta G/\mathrm{d}r = 0$, referred to as a critical cluster and denoted with an asterisk:

$$r^* = \frac{2\gamma_{\mathrm{iL}}\nu}{kT\ln S} \qquad \textbf{Equation 2.6}$$

$$n^* = \frac{32\pi\gamma_{\mathrm{iL}}^3\nu^2}{3(kT\ln S)^3} \qquad \textbf{Equation 2.7}$$

$$\Delta G^* = \frac{16\pi\gamma_{\mathrm{iL}}^3\nu^2}{3(kT\ln S)^2} \qquad \textbf{Equation 2.8}$$

where r^*, n^* and ΔG^* are the radius, number of molecules and Gibbs free energy of formation of the critical cluster. The nucleation rate coefficient, with units of number per unit volume per unit time, is then derived via the Arrhenius equation[54,57]:

$$J_{\mathrm{hom}}(T) = A_{\mathrm{hom}}\mathrm{e}^{\left(\frac{-\Delta G^*}{kT}\right)} \qquad \textbf{Equation 2.9}$$

where $J_{\mathrm{hom}}(T)$ is the temperature dependent ice nucleation rate coefficient and A_{hom} is the pre-exponential, in cm^{-3} s^{-1}. A number of different formulations for the pre-exponential have been suggested in the literature:

$$A_{\mathrm{hom}} = \frac{2(\gamma_{\mathrm{iL}}kT)^{1/2}}{\nu^{5/3}\eta}$$

Equation 2.10 (Huang 95 A[58])

$$A_{\mathrm{hom}} = \left(\frac{5f}{c\nu^{2/3}}\right)\left(\frac{3\gamma_{\mathrm{iL}}}{m}\right)^{1/2}[1 - S]$$

Equation 2.11 (Huang 95 B[58])

$$A_{\mathrm{hom}} = \left(\frac{\rho_{\mathrm{L}}kT}{\rho_{\mathrm{ice}}h}\right)\left(\frac{\gamma_{\mathrm{iL}}}{kT}\right)^{1/2}$$

Equation 2.12 (Pruppacher 95[62])

$$A_{\mathrm{hom}} = \frac{N_{\mathrm{L}}kT}{h}$$

Equation 2.13 (Tabazadeh 02[44])

Equation 2.10 and Equation 2.11 are two forms of the pre-exponential proposed by Huang and Bartell[58], Equation 2.12 proposed by Pruppacher[62], and Equation 2.13 by Tabazadeh, Djikaev and Reiss[44]. ν is the molecular volume (calculated from the density of ice), η the viscosity of water (extrapolated from Hallett[63]), S the super-saturation (relative to stacking disordered ice, using pressures calculated as per Murphy and Koop[51] and Equation 2.5), ρ_{L}

and ρ_{ice} the density of the liquid and ice phases[64], h is the Planck constant and N_{L} the water molecule concentration (derived from ν). In Equation 2.11 c is the intermolecular spacing[58] (approximated here as double the radius of the molecular volume, assuming spherical), m is the molecular mass, and f is the fraction of collisions between liquid phase molecules and the growing ice cluster which result in the addition of that molecule to the cluster, taken to be a constant value of 0.27[58,65]. γ_{iL}, the ice-liquid surface energy is approximated by Huang and Bartell[58] as $\gamma_{\mathrm{iL}} = 20.14 + T/70$. Example values of these pre-exponentials are shown in Figure 4.4 in Chapter 4.

Over short temperature ranges, such as those experienced in typical homogeneous nucleation experiments, J can be approximated as log-linear[28,29]:

$$J_{\mathrm{hom}}(T) = A_{\mathrm{hom}}\,\mathrm{e}^{\frac{-16\pi\gamma_{\mathrm{iL}}^{3}\nu^{2}}{3k^{3}T^{3}(\ln S)^{2}}} = \mathrm{e}^{aT+b} \qquad \textbf{Equation 2.14}$$

in which a and b are empirically derived constants representing the temperature dependent and independent factors of both the exponential and pre-exponential in Equation 2.9.

Nucleation itself is a probabilistic process and Equation 2.9 and 2.14 provide the mean number of freezing events per unit volume per second. The probability of a nucleation event occurring is related to the nucleation rate coefficient via the Poisson distribution[66]:

$$P_x(\Delta t) = \frac{(JV\Delta t)^x}{x!}\mathrm{e}^{-JV\Delta t} \qquad \textbf{Equation 2.15}$$

where $P_x(\Delta t)$ is the probability of x nucleation events occurring in a droplet of volume V during a time period Δt. At values of J high enough to observe freezing events within experimental timescales, the probability that x is greater than one is non-zero. In practice this makes Equation 2.15 difficult to evaluate, as the majority of experimental instruments are only able to identify if a droplet is frozen or unfrozen. Therefore, it is more useful to define the probability of one or more event occurring in a droplet, via the definition of the probability of zero events ($x = 0$)[66]:

$$P_0(\Delta t) = \mathrm{e}^{-JV\Delta t}$$

$$P_{x>0}(\Delta t) = 1 - \mathrm{e}^{-JV\Delta t} \qquad \textbf{Equation 2.16}$$

This probability is equivalent to the fraction of droplets frozen[66-68], which can be independently calculated by observations of freezing events[28,29,54]:

$$\frac{n_{\mathrm{i}}}{n_{\mathrm{L}}} = 1 - \mathrm{e}^{-J(T)V\Delta t} \qquad \textbf{Equation 2.17}$$

in which n_{i} is the number of droplets frozen during Δt, at the start of which n_{L} drops are liquid. This method of calculation has the effect of turning the analysis into a series of short constant-temperature (isothermal) experiments, which requires the assumption that the mean droplet volume, V, and J do not change significantly during Δt. A detailed analysis of the validity of this assumption about J appears in Chapter 4; the relevance of the assumption of a constant volume during the time step has been minimised by only calculating nucleation coefficients using droplets of the same measurement size.

Rearrangement of Equation 2.17 allows the calculation of J from experimental data:

$$J(T) = -\frac{\ln\left(1-\frac{n_{\mathrm{i}}}{n_{\mathrm{L}}}\right)}{V\Delta t} \qquad \textbf{Equation 2.18}$$

In the calculation of the Gibbs free energy of the creation of the critical ice cluster, there is a term for the ice-liquid surface energy. The standard methods for estimating this surface energy are only valid for the bulk substance and are not suitable at ice germ size scales. The ice-water surface energy γ_{iL} can be estimated from experimental values of J by inserting Equation 2.8 into Equation 2.9 and taking the natural logarithm[29]:

$$\ln J_{\mathrm{hom}}(T) = \ln A_{\mathrm{hom}} - \frac{16\pi\gamma_{\mathrm{iL}}^{3}\nu^{2}}{3k^{3}T^{3}(\ln S)^{2}} \qquad \textbf{Equation 2.19}$$

In cloud sized droplets (~5 – 20 μm diameter[26,27]), homogeneous freezing occurs at ~234 K – ~237 K. Within this range, experimental results from a number of authors are present in the literature (Figure 2.4).

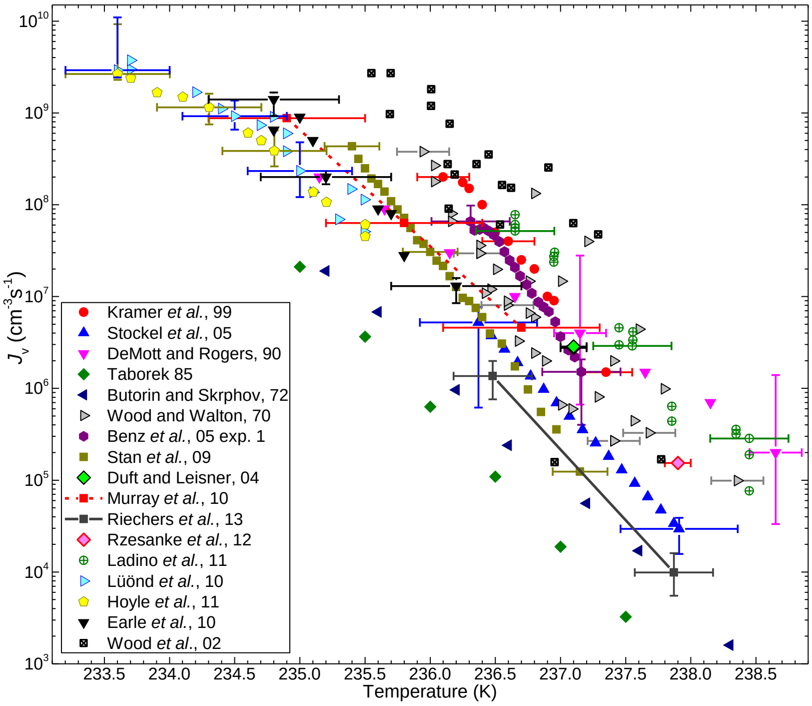

Figure 2.4. Summary of homogeneous nucleation rate coefficients from the literature. Sample error bars are provided when available. Note the spread in the data of around 2 K, larger than the quoted temperature uncertainties. Data are from a range of techniques such as aerosol flow tubes, electro-dynamic traps, hydrophobically supported and emulsion experiments[28,29,42,69-82].

While the literature works agree on the value of J there is a spread in the temperature of the results of ~2 K, equivalent to three orders of magnitude. Uncertainties have been provided by some authors, it is likely that the principle cause of temperature scatter is due to the absolute accuracy of temperature measurements rather than uncertainty in the calculation of J (ref [28]). In comparison to temperature measurements volume measurements are relatively accurate. For example, the smallest droplets discussed in Chapter 6 cover a range of 5 ±1.25 µm diameter, which corresponds to volumes between 95 % larger and 58 % smaller.

2.2.3.1.1. Homogeneous nucleation at the droplet surface

In 2002, it was suggested that homogeneous nucleation may be occurring due to the droplet surface as well as the droplet volume[44,83]. This conclusion came from the discovery that for some experimental setups, the scatter in the nucleation rate coefficient was reduced if the results were normalised to the droplet surface area rather than volume[44]. It has been hypothesised that surface nucleation can occur in one of two ways; either as a genuinely two dimensional surface based process, or as a process which occurs within the volume of a thin surface layer[46]. The volume of this layer can then be approximated by multiplication of the droplet surface area by the thickness of the layer[46].

Two different effects may encourage nucleation at the surface: firstly, a reduction in the overall ice cluster surface energy due to part of the cluster being in contact with the droplet surface[83], resulting in a smaller critical cluster and a shallower temperature dependence (Figure 2.5, in Equation 2.14 γ_{iL} is reduced). Secondly, changes to the molecular characteristics near the droplet surface, such as charge distribution, density and molecular ordering[84,85]. A reduction in density would increase the molecular volume, steepening the temperature dependence (in Equation 2.14 v is increased).

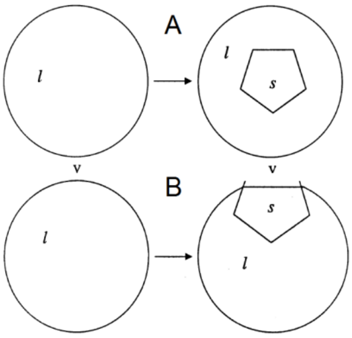

Figure 2.5. Schematic representing volume and surface based nucleation. A) volume nucleation, B) surface nucleation. The area marked v represents the vapour phase, l the liquid phase and s the initial solid cluster. Adapted from Figures 1 and 3 of ref [83].

However, the small volume of a near-surface layer means that the pre-exponential needs to be several orders of magnitude larger for surface nucleation than for volume nucleation[46]. In all forms of the pre-exponential listed previously (Equation 2.10 to Equation 2.13) increasing ν causes a reduction. This implies that either the descriptions of the pre-exponential derived for volume nucleation do not correctly represent surface based nucleation, or that properties other than ρ_L and ν need change to result in a larger pre-exponential.

The overall homogeneous nucleation rate can be calculated by the summation of the surface and volume rates:

$$J_{\text{tot}} = J_V V + J_s s \qquad \textbf{Equation 2.20}$$

Where J_{tot} is the total nucleation rate, J_V and J_s are the droplet volume (V) and droplet surface (s) nucleation rate coefficients respectively. Using the total nucleation rate in Equation 2.20 to revise Equation 2.17 allows calculation of the number of droplets frozen[44,77,86]:

$$\frac{n_i}{n_L} = 1 - \mathrm{e}(-J_{\text{tot}}(T)\Delta t) \qquad \textbf{Equation 2.21}$$

Equation 2.20 suggests that the relative importance between the surface and volume nucleation rates will depend upon the droplet radius[44,77,86]. This allows for the definition of a specific radius at which the nucleation rates due to the volume and surface of a spherical droplet are equivalent (referred to in the literature as the critical radius, but referred to here as the equivalent radius r_{eq} to prevent confusion with Equation 2.6)[44,77,86]:

$$r_{\text{eq}}(T) = \frac{3J_s(T)}{J_V(T)} \qquad \textbf{Equation 2.22}$$

From the comparison of nucleation rates in 19 and 49 µm radius droplets, Duft and Leisner[77] concluded that, if surface nucleation is important, at 237.1 K r_{eq} is no greater than 4 µm. Recent experiments by Kuhn *et al.*[86] and Earle *et al.*[81] found values of r_{eq} of 3.4, 5.1 and 7.7 µm at ~236.15, ~235.5 and ~234.75 K. At significantly larger (smaller) radii nucleation by the droplet volume (surface) will dominate the observed nucleation rate. By the derivation of J_s and r_{eq}, the hypothesis that nucleation at the droplet surface is responsible for freezing in small water droplets will be tested (Chapter 6).

2.2.3.2. Heterogeneous ice nucleation

Within relevant time scales, freezing at temperatures above those for homogeneous nucleation freezing can be triggered by the presence of a particle, or nucleus, causing heterogeneous ice nucleation. This nucleus acts by providing a surface for ice clusters to form on, reducing the energy requirement, ΔG^*, in Equation 2.9. This increases the nucleation rate coefficient and hence the temperature at which ice formation occurs within observable time scales. There are several pathways, or modes, of freezing and which modes are active depends upon the humidity and presence/absence of liquid water and the location of the particle relative to this water.

2.2.3.2.1. Modes of heterogeneous ice nucleation

Deposition mode and condensation mode freezing are when water vapour deposits directly upon a dry aerosol particle, resulting in the formation of ice. In deposition mode nucleation, a critical ice cluster grows on the particle surface directly from vapour in the absence of any liquid[9,54,87]. Condensation mode is when a liquid water cluster condenses from vapour and freezes before a bulk liquid phase can form[87]. Experimentally, condensation mode and deposition mode are usually differentiated using humidity[31,35,54] – super-saturation with respect to ice but not liquid implies deposition freezing; super-saturation with respect to liquid implies condensation. Condensation and immersion freezing can be difficult to differentiate between, especially in laboratory equipment where the initial formation of the liquid phase is not explicitly observed, such as in continuous flow diffusion chambers operating at $S_{\text{liq}} \geq 1$ (ref [42]). Pruppacher and Klett differentiate condensation and immersion freezing using the temperature that condensation of the liquid occurred – above 273 K is immersion and below is condensation[9]. The alternative definition described by Vali[87] and Young[54] of condensation freezing occurring during the process of condensation and immersion freezing at some time after condensation is completed is used here.

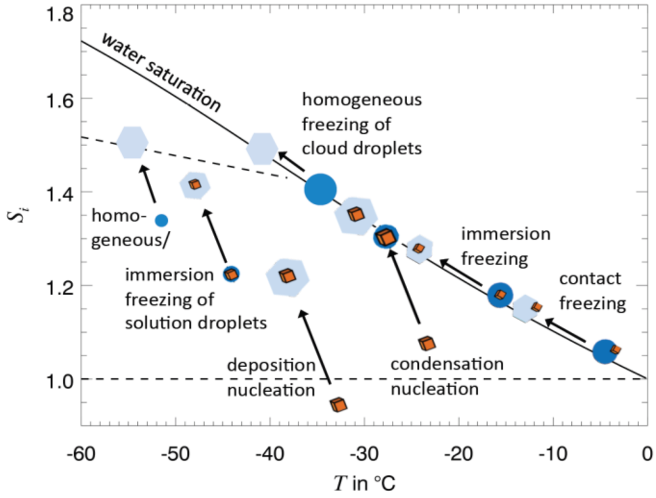

Figure 2.6. A summary of all the different heterogeneous nucleation modes, relative to the saturation ratio and temperature. See the text for a description of each nucleation mode. The homogeneous freezing of pure and solution droplets, along with immersion mode freezing of solution droplets are shown for reference. From Hoose and Möhler[31].

Condensation mode nucleation has been theorised to occur when liquid and ice-like clusters exist independently upon a dry particle[54]. At some point, an ice cluster is hypothesised to exist which is at a sub-critical size with respect to deposition nucleation but a super-critical size with respect to immersion freezing. If a liquid-phase cluster on this same particle then becomes super-critical and grows spontaneously, it will eventually come into contact with this ice cluster and condensation is quickly followed by freezing[54]. This rate-determining step of liquid condensation makes condensation freezing different to immersion freezing.

Aside from knowledge of the humidity of the ambient air, observational differentiation between these two types of nucleation is difficult[9]. At $S_{\mathrm{liq}} \geq 1$, it could be assumed that the mode of freezing is condensation, however this does not exclude the possibility that a critical ice germ formed without condensation of the liquid phase. Likewise, nucleation at $S_{\mathrm{liq}} < 1$ would suggest that freezing is due to the deposition mode, but sufficient liquid may be present in pores and cracks due to capillary condensation, allowing immersion/condensation freezing[88]. Additionally, Ostwald’s rule of stages implies that the liquid phase, the creation of which is energetically less demanding, will be present as a short lived intermediate step even in deposition mode freezing[57].

Immersion mode freezing requires a particle in direct contact with liquid water and the critical ice cluster forms upon the immersed particle surface[54,87]. This particle does not need to be a solid so long as there is defined boundary between the two phases (for example, an immiscible organic liquid[89]). Ice clusters then form at the phase boundary, causing a reduction in the energy requirement of nucleation. This is discussed in more detail in the following sections.

Contact mode nucleation is when a particle comes into contact with the surface of a liquid droplet causing freezing[9,54,87]. The particle typically originates from outside the droplet, and freezing is caused by the impact or the presence of the particle at the surface, rather than purely due to the liquid and particle surface touching as in the immersion mode. This results in droplets which freeze several degrees higher than the same particle freezes in the immersion mode. For example, kaolinite froze at less than 243 K in the immersion mode but exhibited contact freezing at above 253 K in a laboratory experiment[79].

Alternatively, the particle causing freezing can be on the inside of the droplet, which is referred to as inside-out contact freezing, as demonstrated by Durant and Shaw[90]. In experiments varying the position of sub-millimetre sized particles in droplets of about three millimetre diameter, particles were in contact with the droplet surface were observed to freeze at about 5 K warmer[90]. In similar experiments, Fornea *et al.*[91] observed a temperature shift of 5-10 K when a particle came into contact with the droplet surface. In experiments using atmospherically relevant droplet/particle sizes this method of freezing will be difficult to differentiate from immersion freezing. A potential method to differentiate between immersion and inside-out contact would be to repeatedly freeze the same droplet as it evaporates (the method used by Durant and Shaw[90]) to observe a significant change in freezing temperature as particles reach the surface.

The Relative importance of the nucleation modes in mixed-phase clouds can be determined from observations of ice in the atmosphere. For example, measurements of atmospheric ice in the south of England showed that 95 % of ice particles formed at above 253 K originated in clouds containing liquid water[92]. This finding is similar to observations of stratiform clouds at high latitudes, which indicated that for ice to form at temperatures above 243 K supercooled liquid droplets had to be present[93]. It was further observed that layers of ice-super-saturated air containing aerosol but not liquid droplets present did not produce ice[93]. Observations of ice nuclei in Alaska found that the number of nuclei active at above water super-saturation was eight times higher than below[94]. Additionally, in cloud layers in the dusty outflow from the Saharan Desert over Cape Verde observed by Ansmann *et al.*[95], 99 % of altocumulus clouds contained liquid water at cloud top, even though 20 – 70 % of clouds observed at below 263 K contained ice.

These observations do not categorically rule out the formation of ice by the deposition and condensation modes. However, the requirement that liquid water is present before ice formation strongly suggests the contact and immersion modes are important. Also, the infrequency of observations of ice-only clouds above 238 K, as in the four year observational record of Westbrook and Illingworth[92], suggests that these are the main methods of ice formation. This is further supported by cloud chamber experiments with mineral dust aerosol at above 233 K, in which the formation of liquid water always preceded the formation of ice[96]. Conversely, observations of smoke-affected altocumulus clouds in Alaska revealed the formation of ice prior to reaching liquid water saturation, suggesting that in this case deposition nucleation was active[97]. There have been a number of observations which suggested contact nucleation was a major cause of ice formation[98-100]. Some of the observations were in sections of evaporating cloud[98,99], and it has been suggested that contact nucleation is only favourable in evaporating clouds[101].

Modelling studies have attempted to determine the contribution of each ice nucleation mode but it is still not clear. In a global climate model study of mixed-phase clouds, Hoose *et al.*[102] found that the majority of ice was formed through the immersion mode, with contact and deposition mode of secondary importance. In a modelling study by Field *et al.*[103] attempting to simulate a layer cloud observed over central USA, it was concluded that the cloud was best described using immersion mode nucleation. The observational phase of this project did not see any evidence to suggest significant deposition or contact nucleation occurred[104]. In a modelling study of persistent Arctic strato-cumulus clouds, immersion and deposition ice nuclei were found to activate and sediment from the cloud early in its lifetime, with continuing ice formation provided by contact nucleation[105].

These observations and model results suggest that while in some circumstances contact and deposition nucleation are relevant, immersion mode nucleation is the most important pathway for the creation of ice in mixed-phase clouds.

2.2.3.2.2. Immersion mode ice nucleation – stochastic descriptions

In the literature, two main models have been proposed to describe immersion mode heterogeneous freezing. In the first, the stochastic description, the statistics of the process are assumed to conform to the classical theory derived for homogeneous freezing (section 2.2.3.1), with a reduced energy barrier. The second model simplifies nucleation by assuming that in a cooling experiment the temperature of freezing does not depend upon the cooling rate and time[68]. Therefore, each droplet has a single characteristic freezing temperature at which nucleation occurs, giving the model its name, the singular approximation[68].

As the stochastic description assumes that heterogeneous nucleation occurs in the same theoretical framework as homogeneous nucleation, the heterogeneous nucleation rate coefficient for a uniform material can be described similarly to Equation 2.14:

$$J_{\mathrm{het}}(T) = A_{\mathrm{het}}\,\mathrm{e}^{\frac{-16\pi\gamma_{\mathrm{iL}}^{3}\nu^{2}\varphi}{3k^{3}T^{3}(\ln S)^{2}}} \qquad \textbf{Equation 2.23}$$

Where $J_{\mathrm{het}}(T)$ and A_{het} are the heterogeneous analogues of $J_{\mathrm{hom}}(T)$ and A_{hom}, and φ is a heterogeneous enhancement factor representing the reduction in the energy barrier vs. homogeneous nucleation (i.e. a reduction to γ_{iL}). All other variables in this equation are as defined in Equation 2.8. $J_{\mathrm{het}}(T)$ is defined as the nucleation rate coefficient per unit surface area of immersed particle per second and A_{het} has the same units. As with homogeneous nucleation (Equation 2.14), over short temperature ranges Equation 2.23 is frequently approximated by an ln-linear temperature relationship. Following the same derivation as homogeneous nucleation via the Poisson distribution, $J_{\mathrm{het}}(T)$ is determined from the observed droplet freezing:

$$\frac{n_{\mathrm{i}}}{n_{\mathrm{L}}} = \left(1 - \mathrm{e}^{-J_{\mathrm{het}}(T)\sigma\Delta t}\right)$$ **Equation 2.24**

with the mean surface area of material immersed in each droplet, σ, replacing the droplet volume. As well as the same assumptions made in homogeneous nucleation (i.e. J and σ do not change significantly during Δt) there is the added assumption that the species responsible for nucleation in each droplet is the same and that the relationship between σ and this species is the same in every droplet. This extra assumption can break down in cases where the ice nuclei are at a low concentration[106], which can be due to the experiment being at a low concentration or if the sample contains a rare but active contaminant/impurity. For example, a kaolinite sample used in immersion mode experiments by Lüönd *et al.*[42] has been suggested to contain ~17 % of other minerals[107] which, due to their lower concentration, would probably fail this assumption if they were active as ice nuclei. Also, if the ice nuclei have a size distribution and a low concentration, the observed freezing may be affected by this distribution.

In some experimental methods, including the cold-stage method used here (Chapter 7), the surface area is typically calculated using the droplet volume. Therefore, it is not possible to take into account particle size/concentration distributions in the statistical process, which may result in the calculation of inaccurate nucleation rate coefficients. Experiments must be designed to avoid this problem, by using samples without rare impurities at concentrations high enough that each droplet contains sufficient particles that the variability in the surface area contained in the droplets is small.

The heterogeneous enhancement factor, φ, in Equation 2.23 is an empirical factor which can be used to relate the observed nucleation rate coefficient to the surface energy between the particle and ice cluster. If the spherical-cap upon a flat surface geometry is assumed then φ is calculated from θ, the contact angle between the ice cluster and particle [9,41,57]:

$$\varphi = \frac{(2 + \cos\theta)(1 - \cos\theta)^2}{4}$$ **Equation 2.25**

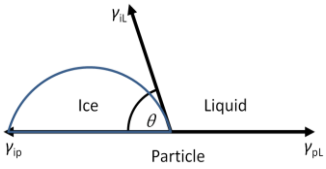

Figure 2.7. Idealised schematic of the surface tensions, or energies, between three phases. The surface energies between the three phases balance, as per Equation 2.26[9,54,57].

As the geometry of this formulation is idealised, the contact angle calculated from this is only suitable as a method of empirical and qualitative comparison between different nuclei[29]. The maximum and minimum values of φ correspond to contact angles for hypothetical wholly ineffective nuclei (θ = 0°, the surface has a tangential contact to the spherical cluster, equivalent to no contact at all) and wholly effective nuclei (θ = 180°, the 'spherical' cluster has an infinitely flat contact with the surface), with all known nuclei having $0 < \theta < 180°$, equivalent to $0 < \varphi < 1$.

While more complex surfaces such as spherical-caps interposed upon concave and convex surfaces have been considered, the formulations of φ resulting from them are complicated (e.g. Fletcher[108]). However, with the experimental instrumentation currently available it is not possible to know the morphology of the site of nucleation, which is not necessarily the same as the bulk surface of the particle.

The contact angle in Equation 2.25 is related to the surface energies of the ice-liquid-particle system by balancing the surface energies of these phases (Figure 2.7)[9,54,57]:

$$\gamma_{\mathrm{iL}} \cos\theta + \gamma_{\mathrm{ip}} = \gamma_{\mathrm{pL}}$$ **Equation 2.26**

where γ_{iL}, γ_{ip} and γ_{pL} are the surface energies of the ice-liquid, ice-particle and particle-liquid boundaries respectively. However, due to the large geometric uncertainties in calculating θ from φ (e.g. Equation 2.25), it is better to directly compare the nucleation rate coefficients of different nuclei, and this is the method which will be used throughout this project.

To provide a more robust description for situations where the assumption of droplet-to-droplet homogeneity breaks down, an extension to the stochastic model has been suggested[41,47,66]. This extended model, named the multiple component stochastic (MCS) model by Murray *et al.*[41] expands Equation 2.24 to incorporate the probability of freezing due to all of the nuclei potentially within the droplet. It is capable of handling both internally and externally mixed droplet populations. In an internally mixed droplet population, each droplet contains the same mixture and surface area of each material; in externally mixed populations there is droplet-to-droplet variability. This allows the model to explicitly account for the surface area distributions discussed above. To include the probability of freezing by the various nuclei, the probability of each nuclei not causing freezing is multiplied together. If there are x different ice nuclei, contained in y different droplet populations, then the fraction of droplets frozen in each population is[41,47,66]:

$$\frac{n_{\mathrm{i},y}}{n_{\mathrm{L},y}} = 1 - \prod_{x} \mathrm{e}^{\left(-J_x(T)\sigma_{x,y}\Delta t\right)}$$

$$\frac{n_{\mathrm{i},y}}{n_{\mathrm{L},y}} = 1 - \exp\left(-\Delta t \sum_{x} J_x(T)\sigma_{x,y}\right) \qquad \textbf{Equation 2.27}$$

where and $n_{\mathrm{L,y}}$ is the number of liquid droplets of population y at the start of time period Δt and $n_{\mathrm{i,y}}$ is the number of droplets frozen from the population during this time period. $J_{\mathrm{x}}(T)$ is the nucleation rate coefficient of ice nuclei x, which has a mean surface area per droplet in this population of $\sigma_{\mathrm{x,y}}$. Summing $n_{\mathrm{i,y}}$ then gives the number of droplets frozen in the overall population[41,47]. Rather than assuming that every droplet is equivalent, it is now assumed that the different nuclei contained in a droplet do not interact, such as by surfaces being occluded by agglomeration.

2.2.3.2.3. Immersion mode ice nucleation – singular approximations

For situations where the assumptions in the stochastic model are not appropriate an alternative model has been suggested - the singular approximation. In this model each droplet, and hence the particles within it, is assumed to have a characteristic temperature at which it will always freeze, regardless of the cooling rate the droplet experiences[67]. The probability of a droplet freezing then depends upon the characteristics of the nucleus, its surface area and the droplet temperature. It is assumed that the observed nucleation in the population is driven by droplet-to-droplet and particle-to-particle variability rather than quantities such as time and the absolute ability of individual particles. Following a Poisson distribution based derivation similar to Equation 2.17 and Equation 2.24, the singular nucleation coefficient is directly derived from observations of freezing. Vali[68] formulated two coefficients to describe the nucleation by unknown particles in water, one referred to as the differential nucleus spectrum, k, and the second the cumulative nucleus spectrum K:

$$\frac{n_{\mathrm{i}}}{n_{\mathrm{L}}} = \left(1 - \mathrm{e}^{-k(T)V(T)\Delta T}\right) \qquad \textbf{Equation 2.28}$$

$$\frac{n_{\mathrm{i}}(T)}{n_0} = \left(1 - \mathrm{e}^{-K(T)V}\right) \qquad \textbf{Equation 2.29}$$

where n_0 is the number of liquid droplets at the beginning of the experiment, $n_{\mathrm{i}}(T)$ is the cumulative number of droplets frozen upon reaching T, and ΔT is the absolute temperature change between observations and is positive. As k and K can be calculated from the same observations, they can be related[68]:

$$k(T) = \frac{[K(T-\Delta T) - K(T)]}{\Delta T} \qquad \textbf{Equation 2.30}$$

While these nucleus spectra are strictly empirical, the only assumption that is made in their use is that in Equation 2.29 the droplet volume is constant throughout the experiment. If this is not true, K cannot be calculated directly from Equation 2.29 as the volume used is associated with n_0 but the freezing probability is related to the volume of the remaining droplets. In these cases, K can be derived via the calculation of k using a temperature dependent droplet volume with Equation 2.28 and Equation 2.30 (see appendix of Vali[68] and Chapter 4).

This formulation of the singular approximation provided by Vali[67,68] used the droplet volume, as the concentration of material in Vali's experiments was not known. When the quantity of material is known, alternate descriptions of the singular nucleation coefficient in Equation 2.29 exist depending on which units of the material are known:

$$\frac{n_{\mathrm{i}}(T)}{n_0} = \left(1 - \mathrm{e}^{-n_{\mathrm{s}}(T)\sigma}\right)$$ **Equation 2.31**

$$\frac{n_{\mathrm{i}}(T)}{n_0} = \left(1 - \mathrm{e}^{-n_{\mathrm{m}}(T)C_{\mathrm{m}}}\right)$$ **Equation 2.32**

$$\frac{n_{\mathrm{i}}(T)}{n_0} = \left(1 - \mathrm{e}^{-n_{\mathrm{n}}(T)C_{\mathrm{n}}}\right)$$ **Equation 2.33**

where n_{s}, n_{m} and n_{n} are the singular nucleation coefficients normalised to particle surface area[30,41,47,109-111], mass[30,111,112], and number[30], with σ, C_{m} and C_{n} being the mean surface area, mass and particle number per droplet. These different coefficients are then intended for use in different scenarios. For example, n_{n} is suitable for describing the nucleation of droplets containing a known number of individual particles such as bacteria cells[113] or pollen[30], whereas n_{m} is suitable for describing the nucleation of a material with an unknown surface area, such as a filtered soil[111,114]. However, as both of these methods assume that the surface area per mass or molecule is not significantly different between samples, it is more common to estimate the surface area and use n_{s}[30,31,41,42,47,107,109-111]. As the specific surface areas of bulk mineral dust samples can be estimated using gas adsorption techniques (see Chapter 5), in this project the singular nucleation coefficient will be calculated using Equation 2.31.

2.2.3.2.4. Sources of heterogeneous ice nuclei

Observations to identify atmospheric ice nuclei have been occurring since the 1950's. The techniques for observing ice nuclei in the atmosphere tend to fall into two broad categories – the identification of ice crystal residues, and the analysis of the background aerosol at a range of temperatures. Measurements of ice nuclei concentrations and composition have been taken around the world and ice nuclei concentrations range from around 10^{-6} to up to 0.1 cm^{-3} (ref [115]), compared to CCN concentrations of 10 – 10000 cm^{-3} (ref [116]). However, identifying the composition of ice nuclei is a more complicated endeavour than measuring their concentration.

Early methods for identifying ice nuclei entailed collecting snow particles from the atmosphere, evaporating/subliming off the ice and then subjecting the residue to electron microscopy. Early observations by Kumai in Japan and northern USA found that 80 – 90 % of ice nuclei were of mineral/soil origin[117,118], a view supported by observations of high ice nuclei concentrations in Japan during periods of high dust outflow from China[119]. However, the collection and analysis of ice crystal residues is a time consuming method which produced just 43 residues over two winter campaigns[117]. Also, due to the need to evaporate off the ice component, this method has the drawback of removing any volatile component[120]. The presence of secondary solid particles in the crystals, as noted by Kumai[117,118], complicated analysis.

An alternative method is to sample the ambient aerosol and then activate them as ice nuclei at a specific temperature and relative humidity, typically using a continuous flow diffusion chamber[33,94,120-123]. The ice nucleating particles are then identified using mass spectroscopy[33,94,120-123]. This method is capable of automatically processing large quantities of aerosol and can be mounted either in an aeroplane[122] or at ground sites[121]. However, this technique is generally limited to particles in a certain size range (typically between ~0.3 and ~1 μm diameter) due to limitations in the mass spectrometer and as particles are classified as frozen if they exceed a certain size[33,120]. The same frozen-unfrozen particle size segregation can be used before analysis to allow for the direct measurement of cloud ice crystal residues[33], resulting in an instrument which successfully automates the earlier time consuming ice residue measurements of Kumai[117,118].

In observations of the composition of ice nuclei taken from ice and mixed-phase clouds and surface aerosols have shown that for America (North, Central and South) and Japan[33-35,94,117-119,123], mineral dusts are a very important ice nuclei type. There were also significant contributions from biological sources[33,35], especially at higher temperatures. There is significant variation with location, for example, observations of ice nuclei composition from near the surface in Brazil found that biological and mineral dust nuclei were each responsible for around half of all ice nuclei[35]. Ice nuclei measured in Alaska were 46 – 70 % mineral dust/metallic particles and 28 – 46 % biological[94] and observations of residues from ice cloud around the Caribbean and Central America showed that mineral dust/metallic particles dominate[34]. However, as authors operating different instruments classify nuclei differently (For example, DeMott *et al*.[123] reports mineral dust and metallic ice nuclei separately, whereas Prenni *et al*.[35] reports a combined measure of dust and metallic ice nuclei), a collation of ice nuclei data is difficult.

Observations of mineral dust ice nuclei currently do not resolve the mineralogical composition of the dust and the ice nucleating ability of the individual minerals which form atmospheric dust is not well known[30,31]. However, observations of mineral dust produced for other purposes have resolved the mineralogy and concentration of dusts around the globe. If the ice nucleating ability of the common dusts are investigated an estimation of the global distribution of mineral dust ice nuclei is possible. Specifically, with the aim of enabling the simple parameterisation of atmospheric mineral dust ice nuclei, in Chapter 7 this project will answer the question, does one mineral dominate ice nucleation by mineral dusts?

2.2.3.2.5. The effects of changing ice nuclei concentrations

Changing the number of CCN in a cloud has several effects which are relevant to precipitation and also radiative transfer, as discussed in Section 2.2.2. Increasing the number of CCN reduces the mean droplet size, meaning that more droplet collisions are required to create rain drops via coalescence and the cloud is optically thicker[13]. Similarly, the presence of ice in a mixed-phase cloud can cause precipitation (Section 2.2.1, ref [32]). This means that precipitation, the lifetime and extent of the cloud are sensitive to the number of ice nuclei[25].

In large convective clouds which are precipitating, the response of changing ice nuclei number is complicated by a sensitivity to the number of CCN (liquid droplets)[124]. For example, in a cloud simulation over Central Europe there was no precipitation response to increasing ice nuclei concentrations by an order of magnitude above normal if the CCN concentration was 100 cm^{-3}, but a 2.5 % increase in precipitation if the CCN concentration was 3200 cm^{-3}. However, in the same study it was found that reducing ice nuclei to an order of magnitude below the normal concentration reduced precipitation by ~5 %, regardless of the CCN concentration[124]. The authors identified the source of the sensitivity to CCN was due to changes in the amount of warm rain – lower CCN numbers had higher amounts of liquid precipitation which reduced the water mass in the cloud at the initiation of freezing, resulting in a low sensitivity to ice nuclei[124]. Ultimately, the changes to ice nuclei had a small effect on the mean precipitation rates in these clouds, likely as the mass of precipitable water in the cloud did not change. The principle effect of changing CCN and ice nuclei concentrations was to change the spatial distribution of precipitation[124]. Changes to the radiation balance still occurred, due to changes in factors such as ice/droplet size distributions and cloud lifetime[124].

There is a threshold number of ice nuclei in these clouds, below which there are insufficient ice nuclei to have an effect upon the cloud, resulting in significant homogeneous nucleation[43]. In a simulation of a cloud parcel in a 0.5 m s^{-1} updraft, at least ~0.1 % of droplets had to freeze heterogeneously before homogeneous nucleation became unimportant[43].

In persistent mixed-phase layer clouds, the effect of increasing ice nuclei concentrations is different. In such clouds, the rate of ice formation is slow enough that the loss of water and aerosol due to precipitation is balanced by addition due to updrafts and mixing from above and below. If the amount of ice in these clouds is increased, precipitation rates increase resulting in less convection and reduced cloud sizes or loss of the cloud altogether[125,126]. However, it has been suggested that changes to the lifetime of clouds is counteracted by increases to the cloud optical thickness due to a reduction in mean cloud particle sizes[127]. As persistent low stratus clouds have a strong cooling effect[11], the effect upon the radiative balance could be significant; this effect is referred to as the cloud glaciation indirect effect[25].

2.3.Summary

Clouds strongly affect the energy balance within the atmosphere and through precipitation they are responsible for the redistribution of water around the globe. Mixed-phase clouds are thought to be responsible for a large proportion precipitation, and persistent mixed-phase layer clouds have a strong radiation impact especially at higher latitudes. However, the characteristics and lifetimes of these clouds are sensitive to the amount of ice they contain, and the concentration of aerosol particles capable of nucleating the ice phase is an important source of ice particles within clouds. Therefore, to accurately predict weather and quantify the natural state of clouds and the effects of humans have upon them, a good understanding of ice nucleation processes and the global distribution of ice nuclei is required. There is significant uncertainty in the rate of ice formation in pure water and the ice nucleating ability of mineral dusts, an important class of ice nuclei, is poorly known.

Chapter 3. Experimental technique

Experiments were performed utilising a freezing assay methodology[29,41,47,67,112,128-131] with droplets of picolitre volume. In brief, an experiment proceeds by the creation of a sample suspension, which is then nebulised onto a hydrophobic slide and sealed from the environment. This slide is then transferred to an optical microscope which has an integrated cold stage, where it undergoes a controlled cooling cycle, typically to around 233 K – cold enough to ensure all droplets freeze. The progress of freezing is recorded via a digital camera for subsequent analysis. A complimentary experimental technique using microlitre size droplets, experiments from which appear in Chapter 7, was developed by others and is included in Section 3.2 for completeness.

3.1.Description of the modified instrument and methodology

The experimental technique used in this project is an evolution of one used previously to investigate ice nucleation[29,41,47,128] (Figure 3.1). During experiments performed before the ones described in this thesis, it became clear that there was scope for improving reliability and accuracy. Temperature gradients within the stage were reduced and cooling made more consistent by constructing a new stage with a cuboid shape. The quality of temperature measurements was improved by using more accurate measurement probes. Experimental efficiency was also increased by simplifying the experimental process, which in turn improved the consistency and reproducibility of experiments. The individual experimental steps are described in the following sections.

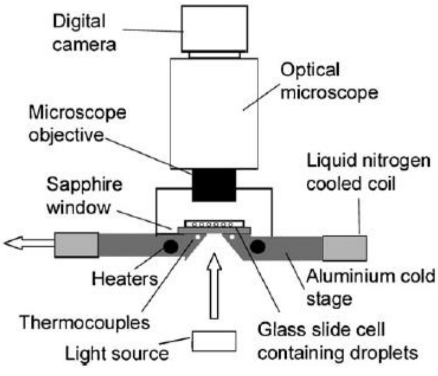

Figure 3.1. Schematic of the experimental setup used prior to this project. The aluminium cold stage was disc shaped with the radius perpendicular to this diagram. Liquid nitrogen flowed into a coil on the outside of the stage and then around the radius of the aluminium disc. From Murray *et al.*[29].

The water used throughout was distilled to 18.2 MΩ cm and filtered to 0.22 µm. Control experiments performed using pure water resulted in freezing temperatures consistent with the homogeneous freezing of water.

3.1.1. Sample suspension

For experiments in which a sample suspension was required its generation proceeded as follows. If necessary, coarse mineral samples were ground dry with an agate mortar and pestle (3 inch diameter mortar and ¾ inch diameter pestle) or an agate ball mill (a cylindrical vessel 2¼ inch diameter and 2¾ inch high, with two ½ inch balls) to obtain particles of an atmospherically relevant size. The mass of sample required for the suspension was accurately weighed out on a 4 point balance (manufacturer stated uncertainty of ±0.0002 g), according to the desired weight per cent and water quantity. The mineral dust was then added to between ~18 and 250 ml of water, measured gravimetrically below ~20 ml and volumetrically above. The amount of water was chosen to give a dust mass large enough that the uncertainty in the mass measurement was insignificant. Volumetric measurements were corrected to take into account the density of water (assuming standard conditions) and the volume taken up by the sample; volumes of 100 ±0.1 ml and 250 ±0.15 ml were used. The samples were then stirred with a Teflon coated magnetic stir bar for at least 16 hours, to distribute material evenly and break up aggregates. Stirring was maintained during droplet generation as well. The mineral weight per cent was used to convert the droplet volume into a sample mass, allowing calculation of the mineral surface area using its specific surface area determined using the gas adsorption technique (see Section 5.2).

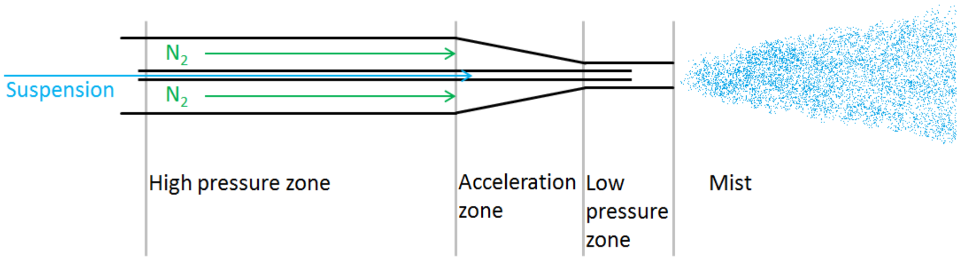

Figure 3.2. Schematic of a nebuliser in operation. The nebuliser is constructed from a thin Teflon pipe inserted into a glass pipette. A flow of nitrogen gas enters the top of the pipette and accelerates as it is forced through the pipette throat, creating a low pressure region in the pipette tip. This low pressure then draws fluid through the pipe and accelerates it out the tip, forming a mist of droplets.

3.1.2. Experimental substrate

A siliconised glass cover slip was cleaned of particles and organic residues by rinsing with water, methanol and chloroform. A thin brass spacer was cleaned in the same way and attached to this slip with vacuum grease, taking care not to get grease near the centre of the slip and to get a complete seal around the edge of the brass spacer. The cover slip was then placed on a large clean microscope slide for nebulisation.

The siliconised cover slips were commercially available and sourced from Hampton Research, USA (cat. no. HR3-278T, 12 mm diameter and 0.22 mm thick). As the manufacturer did not provide the water contact angle of these slides, it was necessary to perform measurements. To measure the water contact angle of the cover slips, water droplets tens of micrometres in diameter were deposited onto a slip and viewed with a magnified camera positioned approximately perpendicular to the slip. Due to the difficulty in determining the location where the droplet meets the substrate in the image, the whole image height, h, was combined with the width, w, to geometrically derive the contact angle (Figure 3.3). Assuming that the effect due to the deviation of the viewing angle from parallel is insignificant, h is double the actual droplet height and the contact angle in degrees is:

$$\theta = 90 + \sin^{-1}\left(\frac{h-w}{w}\right)$$ **Equation 3.1**

From measurements of 64 different droplets the mean contact angle was 100°16’ ± 2°50’ (±1 standard deviation).

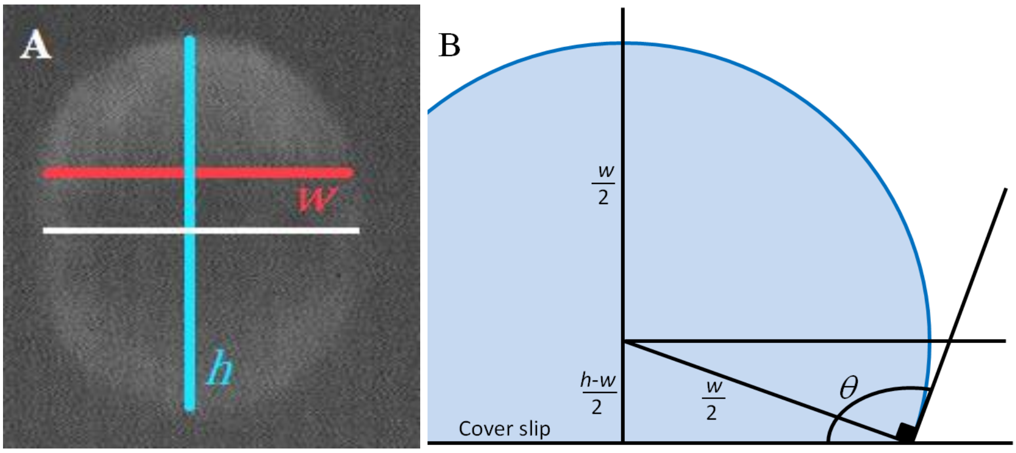

Figure 3.3. Methodology for calculating the substrate contact angle. A) Image of a droplet upon the substrate, a few tenths of seconds after droplet generation. The approximate location of the cover slip is marked by the white line. h and w are used in the calculation of the contact angle, and in this image w is approximately 50 µm. B) The geometry used to calculate the contact angle, θ.

3.1.3. Droplet generation

The cover slip and microscope slide were positioned in the main opening of a large three necked flask (Figure 3.4). The flask interior is kept at water saturation using a flow of humidified nitrogen from a bubbler. The bubbler was immersed in water slightly above room temperature as it will cool slightly due to evaporation during extended use. The pipe from the bubbler to the nebulisation chamber is long enough to ensure that there is no super-saturation in the flask, evidenced by the observation of condensation in the pipe near the bubbler but not near the nebulisation chamber. A plastic bag was attached to the chamber neck to reduce the diffusion of dry air from the environment.

The prepared suspension was then aerosolised into the chamber using a nebuliser through the second opening. The suspension droplets then exited the chamber through the neck, falling onto the slip in the process. The nebuliser was constructed from a small glass pipette and a 24 gauge Teflon pipe (Figure 3.2). It utilises Bernoulli's Principle to create a region of low pressure at the end of the Teflon pipe which draws suspension fluid along the pipe and into the stream of dry nitrogen gas. The sudden acceleration of suspension breaks it down into a mist of micrometre size droplets.

Nebulisation typically lasted for 2-4 minutes and consumed around 6 ml of liquid per minute, with a nitrogen pressure of 1.6 bars. At the end of this process the droplets were isolated from the environment by adding a drop of silicone oil. Examples of nebulised droplet distributions are shown in Figure 3.5.

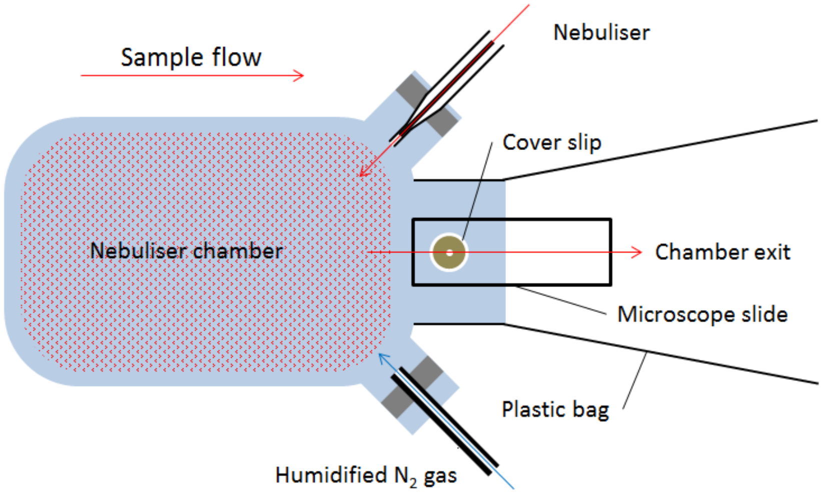

Figure 3.4. Schematic of the nebuliser chamber. The chamber is a large three necked flask maintained at liquid water saturation by a flow of N_2 gas from a bubbler (blue arrow). The nebulised sample (red arrows) flows over the cover slip as it exits through the neck. A plastic bag is attached to the chamber to reduce the diffusion of air from the environment.

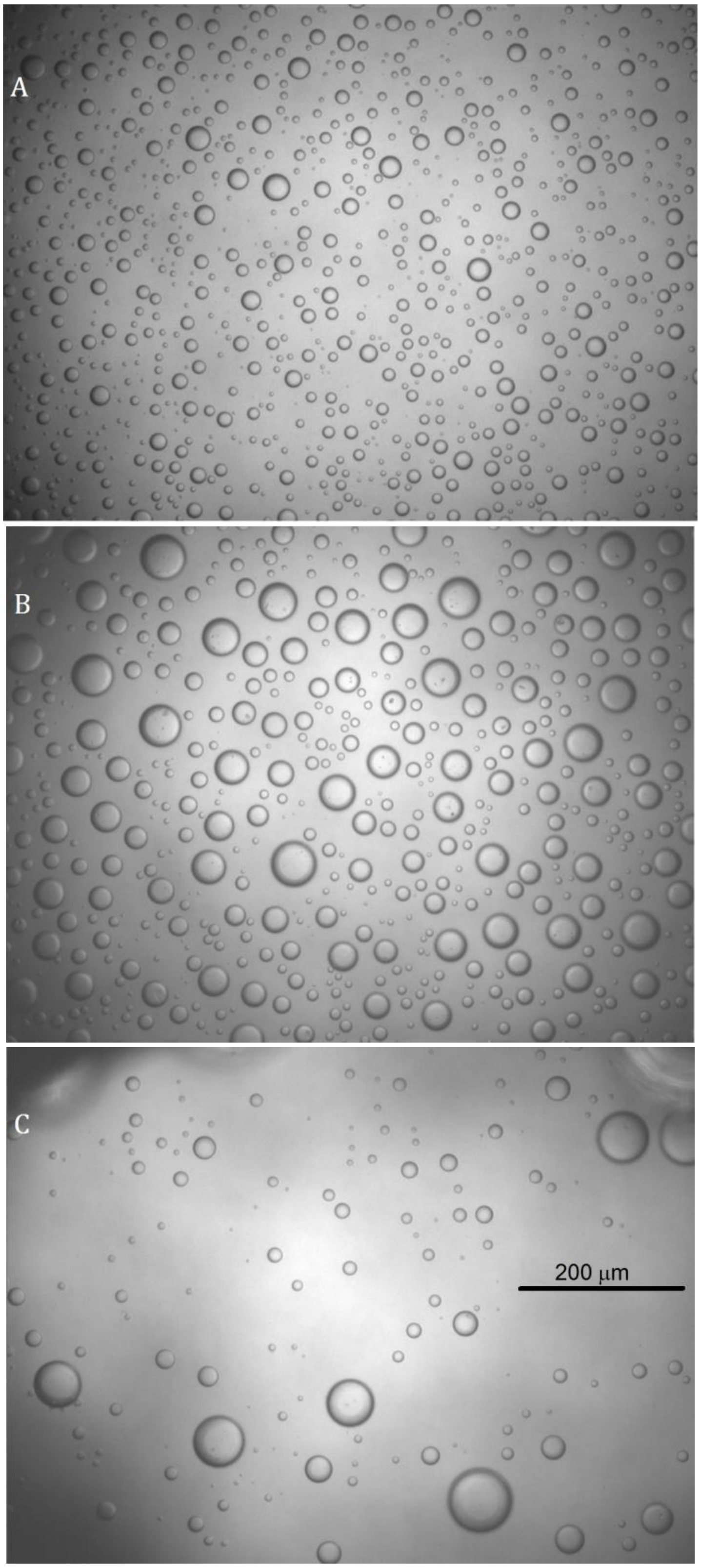

Figure 3.5. Examples of different nebulised droplet distributions. A) A good distribution of small pure water droplets, >600 droplets 5-30 µm diameter. B) A good distribution of large chlorite containing droplets, 5-50 µm, however this distribution was too large for the work in Chapter 7, as these distributions tend to have low numbers spread over a wide range of droplet sizes. C) A poor distribution – sparse droplets with some small and a few very large droplets, unsuitable for analysis. All images are to the same scale.

3.1.4. Isolation of droplets from the environment

The calculations to estimate the ice nucleating efficiency of a mineral rely on accurate knowledge of the amount of mineral in each droplet. Therefore, it is important that no water evaporates from or condenses onto the droplets during or after nebulisation. At the end of nebulisation the droplets are isolated from the environment by adding a drop of silicone oil (Sigma Aldrich 146153) to the centre of the brass spacer (Figure 3.6). The term ‘cover slip assembly’ is used to refer to this sealed substrate. Once isolated, the droplets are transferred to the cold stage equipped microscope.

If the material suspended in the droplets interacts with the silicone oil in some way, the droplets can be contained in a small pocket of air. Nebulisation occurs as described above, except a cover slip is used without the brass spacer attached. The spacer is instead greased on both sides and added to a second clean cover slip. After nebulisation this section is added to the nebulised cover slip, sealing droplets in the centre of the spacer (Figure 3.6). However, isolating in air allows water to transfer from liquid to frozen droplets in a manner similar to the Bergeron Findiesen process (Figure 3.7, e.g. refs [9,32]). As the oil isolates individual drops from each other and did not appear to interact with the mineral dusts, it was the experimental method used throughout.

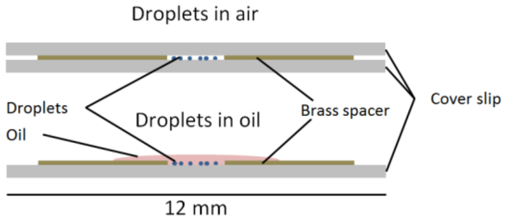

Figure 3.6. Schematic of the cover slip assemblies used. A different assembly is used if the droplets are to be isolated in oil or air. For experiments in oil a brass spacer is attached to a cleaned cover slip using grease, and after nebulisation the centre of the spacer is filled with silicone oil. In air, a cover slip without spacer is used for nebulisation and after nebulisation the spacer is added with a second cover slip to seal the droplets off from the environment. Not to scale.

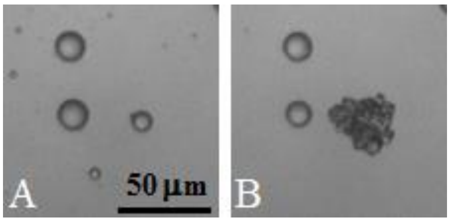

Figure 3.7. The results of vapour transfer between droplets in air. A) The small droplet in the centre of the image immediately after freezing. B) The same set of droplets some time later. Note the disappearance of the droplet at the bottom of the image and the loss of mass from the one to the left, resulting in a substantial increase in the size of the frozen droplet in the centre.

3.1.5. Droplet observation

The cold stage is mounted to the z-stage of an Olympus BX51 optical microscope with 10× magnification and a trinocular observation tube. This tube allows simultaneous observation using the eyepiece and an attached digital camera (Hitachi KP-M1AP). In the centre of the stage there is a hole which allows observation of the droplets by transmission microscopy.

As the droplets are positioned over this hole, there is a temperature difference between the droplets and the aluminium stage. At 0.22 mm thick, the glass cover slips are too thin to sufficiently conduct heat away from the droplets at the desired rate. Therefore, the hole is spanned by thermally conductive window (thermal management grade polycrystalline diamond: TM180, ~1800 W m^{-1} K^{-1}, 0.25 mm thick, supplied by Element Six, UK) to minimise the temperature difference between the droplets and stage, while still allowing transmission microscopy. The diamond is smoothed (to 50 nm) on one side and rough (250 nm) on the other. The smooth side is used to support the cover slip assembly and the rough side is in contact with the stage. The window is attached to the stage using a heat transfer paste (Omegatherm 201, ~2.3 W m^{-1} K^{-1}), taking care not to get the paste in the hole in the stage. As this paste is a less efficient heat conductor than the other materials used to construct the stage as thin a layer as possible is used.

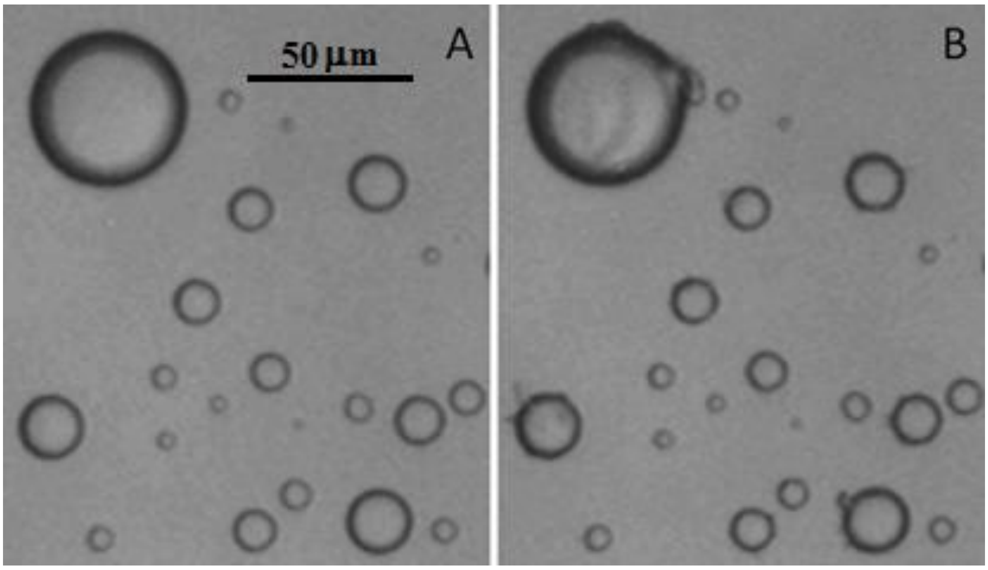

Figure 3.8. Comparative images of A): liquid and B): frozen droplets. The droplets are isolated from the environment by oil (see section 3.1.2). In droplets larger than about 10 µm the droplet outline is visibly distorted by freezing, whereas in smaller droplets a subtle contrast change is all that occurs.

Video recordings are stored on a large networked hard drive in .avi format. This format ensures that any potential loss of detail from compressed formats such as .mpg does not impact the analysis of smaller droplets. To keep the amount of data collected to a manageable size, recordings are made at ~5 frames per second; at this frame rate, a typical 1 K min^{-1} homogeneous experiment creates a video file 3 GB in size. To facilitate the video recording and simultaneously record the time of each frame to millisecond resolution, a program with a simple GUI was written in the National Instruments LabVIEW environment (see appendix). The videos are then analysed to produce nucleation statistics (Chapter 4).

In droplets larger than about 10 µm diameter, freezing is clearly noticeable as a change in the outline of the droplet. For smaller droplets generally the only visible change is a darkening of the droplet outline (Figure 3.8). The size of the droplet is measured prior to freezing and the time of freezing retrieved via the frame time.

The shape distortions observed occurring in larger droplets in Figure 3.8 are an interesting feature. They are probably a side effect of performing these experiments in oil, as they are seen infrequently in experiments in air. After nucleation, the growth rate of the solid phase depends upon the rate of dissipation of the heat of crystallisation[57]. If nucleation does not occur in the very centre of the droplet, cooling by conduction to the surrounding oil will encourage the growth of the crystal phase towards, and then across, the surface of the droplet (e.g. refs [132-134]). The result is a core of supercooled water surrounded by a shell of ice[135]. As the ice grows into the liquid core, its expansion increases the pressure on the core until a fracture in the shell occurs, and a jet of liquid is ejected from the fracture. This jet rapidly freezes, resulting in a protrusion of ice, as has been seen by many in the past[135-137], and can be seen in some of the larger droplets in Figure 3.8B.

3.1.5.1. Droplet size measurements

Droplet sizes are measured shortly before freezing directly upon a monitor using a ruler with 1 mm divisions. The on-screen image sizes are then converted to actual droplet sizes in µm, using the mm to µm ratio from the measurement of an image of a micrometre (Figure 3.9). As the lines of the micrometre are approximately 2 µm thick an error in the size conversion can occur; to minimise this a long section of the micrometre (700 µm) was used to calculate this ratio. By assuming that any slight lack in focus caused by droplet sizes and/or contraction of the stage does not result in a significant error, the uncertainty in the droplet size is due to the ±0.5 mm accuracy of the on-screen measurement. The conversion ratio on the screen used for the majority of analysis is ~2:5 mm:µm, resulting in a droplet size uncertainty of ±1.25 µm.

3.1.5.2. Freezing time accuracy

The time of droplet freezing is taken from the frame time records created by the computer. These records are at millisecond resolution and each frame is approximately 200 ms apart. Assuming that ice nucleation occurs and becomes visible during the same frame, the uncertainty in the time of freezing is ±100 ms. In a 1 K min^{-1} experiment this corresponds to a temperature error of $\pm 1.67 \times 10^{-3}$ K. However, the stage temperature is measured by a hand held temperature logger which does not have the capability to record directly to the computer, and it is necessary to synchronise the timing of the temperature logger to that of the stage. This synchronisation is performed shortly after beginning the video recording by sharply adjusting the light on the microscope in conjunction with starting the temperature logger, giving a frame time for the start of the temperature logger record. It is estimated that the error introduced by this synchronisation is about ±1 s, equivalent to ±0.02 K when cooling at 1 K min^{-1}. In comparison with the temperature uncertainty due to the stage (see section 3.1.7.1) the temperature error due to timing in a 1 K min^{-1} experiment is small and is considered insignificant.

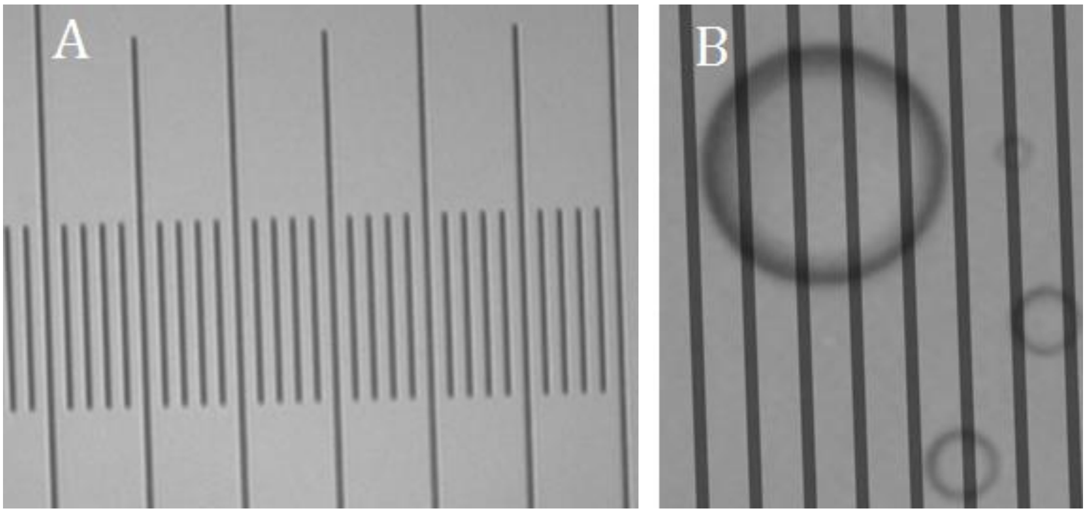

Figure 3.9. A) Image of a section of the micrometre and B) an example of droplets with an overlaid 10 µm scale. The micrometre in A) provides 100 ticks, each 10 µm apart, for a total length of 1 mm. The image shown in B) has been magnified and contrast adjusted for clarity, and shows the largest droplet visible in Figure 3.8.

3.1.6. Cold stage

The cold stage consists of an aluminium block mounted to an optical microscope. Significant heat conduction between the stage and the microscope was prevented by an insulating sheet of Teflon (see Figure 3.10 for a schematic of the stage). The block was cooled by liquid nitrogen, with the temperature controlled by counter-heating cartridge heaters. As the heaters have a power output of 15 W each, it was necessary to throttle the liquid nitrogen flow depending on the desired cooling rate. The cover slip assembly sits on a transparent window spanning a hole in the centre of the stage, which allows observation by transmission microscopy. The stage temperature is measured by two probes embedded into the stage close to the droplets. The new cold stage design is intended to give improved experiment quality through more consistent and accurate temperature control and improved productivity from increased usability and reliability.

The overall size and thermal mass of the stage has been reduced, giving multiple benefits. Less input from the cartridge heaters is required to control the temperature, thus reducing the response time of the stage to heating by the temperature controller, allowing for more accurate control as can be seen in Figure 3.11. As there is also a corresponding reduction in the surface area of the stage, heating from the environment is reduced. By replacing the single circular nitrogen line around the stage with two smaller parallel internal lines, the cooling is much more reliable and symmetrical across the stage. This also has the advantage of reducing the amount of nitrogen used, reducing equipment running costs and downtime. Collectively, these changes have reduced the variability of the stage temperature. A comparison of temperatures recorded during ~1 K min^{-1} cooling runs show that the new stage design reduces the root-mean-square (RMS) variability of temperature by ~63 % (Figure 3.11).

The compactness of the new design provides additional improvements to usability. The maximum vertical clearance between the microscope objective and z-stage is ~40 mm.

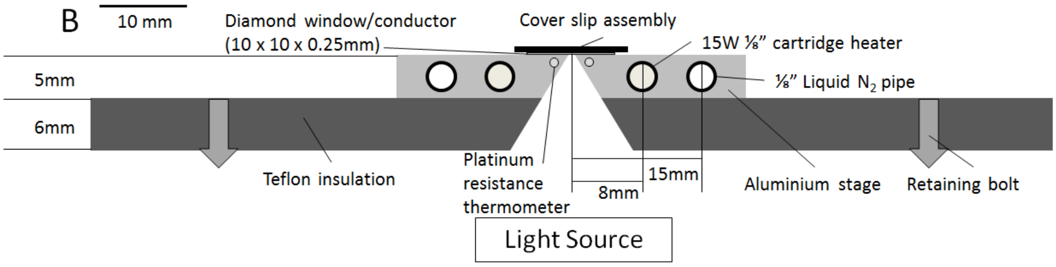

Figure 3.10. Scale side view schematics of the cold stage. The stage consists of an aluminium block 5 × 40 × 30 mm.

In comparison the stage including window takes up 11.25 mm. After most runs it is necessary to remove and clean oil from the diamond window, and at the beginning of runs it is necessary to position the cover slip assembly to acquire the best possible droplet distribution. Increasing the available space makes these operations much easier. Also, the stage typically cools by around 50 K during an experiment, and there is significant thermal contraction especially in the Teflon. Moving the droplets vertically by a few μm will take them out of focus, resulting in the video gradually drifting out of focus. By reducing the thickness of the stage, the thermal contraction is correspondingly reduced by around 40 % to 46 μm, improving video quality.

3.1.7. Temperature measurement

Temperatures are recorded using two platinum resistance thermometer (PRT) probes embedded near to the hole in the centre of the block. These probes (Fluke 5622-05) have a reported accuracy of ±0.04 K. One probe is used to supply temperature data to a data logger (Fluke 1524) at 1 Hz, which has an additional reported error of ±0.01 K. The second probe supplies data to a Eurotherm 2416 temperature controller, which controls the counter-heating in the stage. It also produces additional temperature logs at ~3 Hz as a backup, and the manufacturers quoted uncertainty for records taken using the Eurotherm 2416 is ±1 K. Both the Fluke 1524 and Eurotherm 2416 produce text file logs of temperature against time (1524: 0.001 K, 0.1 s resolution, 2416: 0.1 K, 1s resolution).

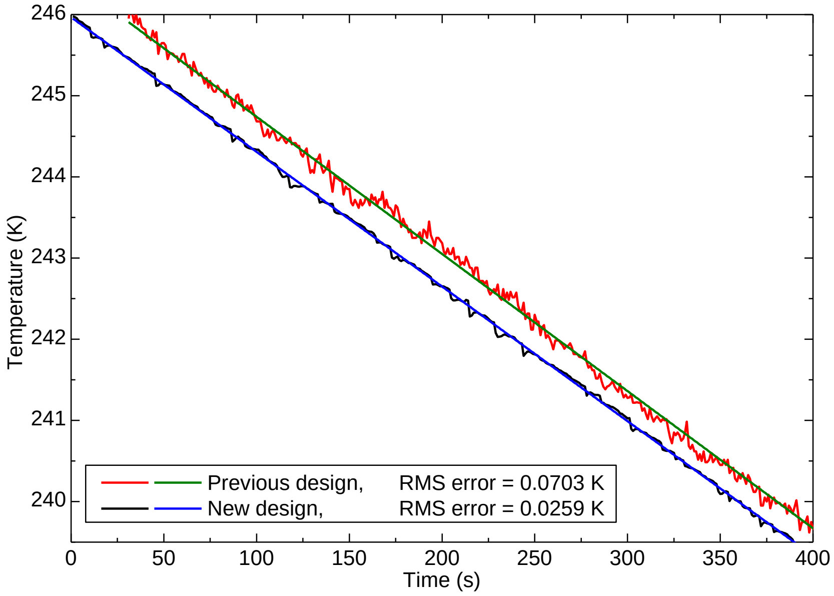

Figure 3.11. Comparison of the cooling smoothness of the old and new stage designs. The new design gives a smoother temperature record with a lower frequency of significant deviations, as can be seen in the previous design (red) at around 150 s.

The PRT probes are additionally calibrated by comparison with a standard (Fluke 5608). This comparison is done by embedding the standard and PRT probes into a deep hole drilled into the centre of a large cylinder of aluminium (7.5 cm diameter, 20 cm long). This cylinder is wrapped in a coil of ¼” copper pipe and encased in a foam thermal insulator. Liquid nitrogen is then passed through the coiled pipework to cool the block. The calibration is performed by comparative analysis between the temperatures recorded by the probe and standard as the aluminium cylinder warms back up to room temperature over the course of several hours.

3.1.7.1. Estimation of temperature uncertainty

During an experiment the stage is not held at thermal equilibrium with cooling balanced by heating, which generates temperature gradients within the equipment. As such, cold stages of this general configuration have a temperature difference between the droplets and the location of the temperature measurement. This difference arises because cooling and heating are provided at specific locations in the stage. In the orientation shown in Figure 3.10 a temperature gradient is formed between the centre (warmest) and the cartridge heaters near the outside.

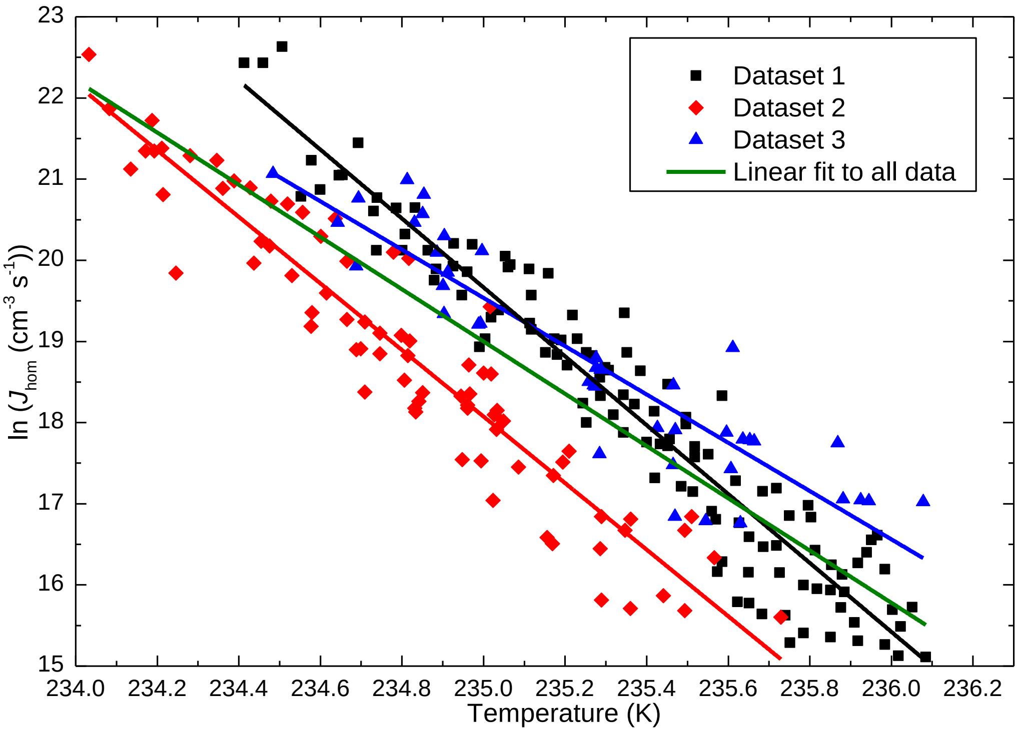

Figure 3.12. Comparison of repeat experiments at 1 K min^{-1}. An ln-linear fit to all the data is provided (green) which is used in the estimation of the temperature variability.

Calibration of the temperature difference between the droplet and measurement locations is difficult. The stage temperature was calibrated using the calculated nucleation rate coefficients. The wide spread in the literature for homogeneous freezing (see Figure 2.4, Chapter 2) complicates matters, meaning that the stage can only be calibrated against itself. Freezing experiments at a range of cooling rates have been performed using the experimental and analysis methodology provided in this chapter and Chapter 4. Three pure water experiments containing in total 1111 droplets of 5 – 20 μm diameter were performed at a cooling rate of ~1 K min^{-1}, nucleation rate coefficients from which are shown in Figure 3.12. Calculating the RMS error between the data and an ln-linear fit (green line) to all three datasets, the temperature variability of the stage at 1 K min^{-1} is ±0.26 K (1 s.d.).

Experiments at four faster cooling rates (not shown) were also performed to investigate any potential systematic temperature uncertainty. However, comparison of the offsets between these results and the 1 K min^{-1} experiments did not produce a clear trend with cooling rate, other than the suggestion of a positive bias. This bias means that, relative to 1 K min^{-1}, the temperature difference between the droplets and the stage temperature measured by the probes is larger at faster cooling rates. As such, at 1 K min^{-1} the variability due to the stage is estimated at ±0.26 K, with a greater uncertainty (±0.5 K) at higher cooling rates up to ~7 K min^{-1}. Combined with the ±0.05 K temperature uncertainty from the measurement probes the overall uncertainty at 1 K min^{-1} is estimated at ±0.3 K, and all experiments presented in Chapters 6 and 7 were done at this cooling rate.

3.2. Microlitre droplet cold stage

To investigate ice nucleation at higher temperatures or by uncommon/less active ice nuclei, the observation of a larger surface area of suspended material is needed. At concentrations greater than about one weight per cent, it became difficult to keep the mineral particles suspended, meaning an increase in droplet size was required. By using droplets of microlitre volume (~1 mm diameter) experiments containing four to six orders of magnitude more particle surface area are possible. However, the droplet nebulisation system detailed in section 3.1.2 is incapable of creating consistent droplets of this size and concentration. Producing a sufficient number of droplets of microlitre size requires a much larger substrate area, meaning the experimental process described previously is not suitable.

The microlitre experimental process is similar to that described above and is described in detail by Whale *et al.*[138]. The principle differences are summarised here. To create microlitre volume droplets an electronic pipette was used, providing droplets of 1 ±0.1 μl. These droplets were deposited onto cleaned hydrophobic slides of the same type described previously (Section 3.1.2) except 22 mm diameter (Hampton Research, USA, HR3-231). As the droplets are much larger than in the picolitre droplets in microscope cold stage, evaporation and mass transfer are not significant issues and so isolation of the droplets from the environment and each other was not required. The slide of droplets was then transferred to the cold plate of an Asymptote-Grant EF600 Stirling-engine flat-plate chiller to undergo a cooling experiment. The larger size of the droplets allows them to be observed without magnification and they were recorded digitally for later analysis of droplet freezing. However, the size of the droplets greatly increases the likelihood of contaminants being present in the pure water used and the chance that droplet freezing is triggered by the substrate (Figure 3.13). The expected homogeneous freezing temperature (~239 K) could not be achieved, limiting this method to freezing events above 253 K, the temperature at which the first 'pure' water freezing events occur[107,138]. The statistical analysis of these experiments proceeded as described in Chapter 4.

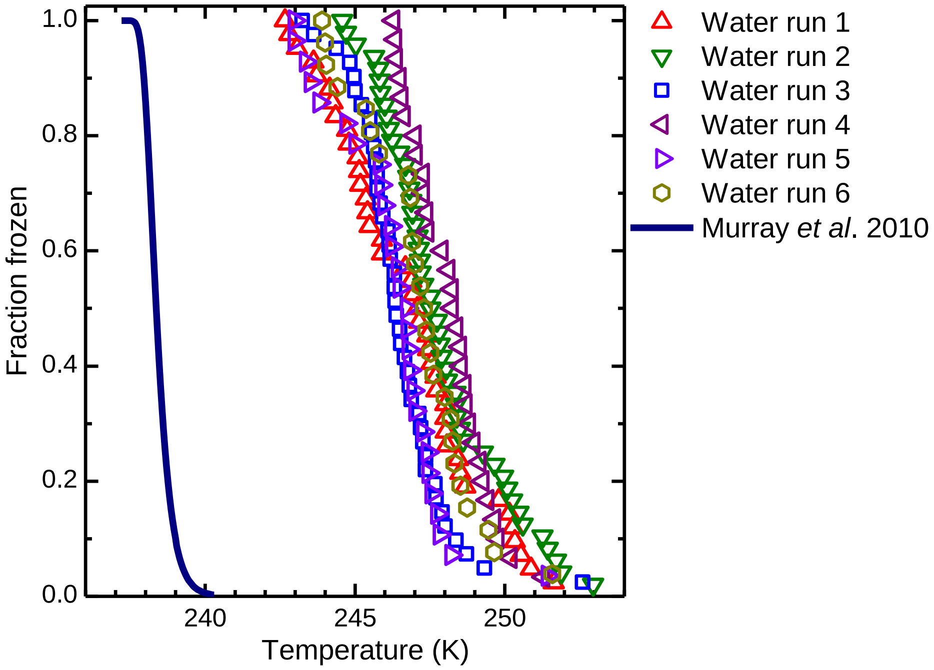

Figure 3.13. Freezing of 'pure' water droplets in microlitre experiments. These experiments form the baseline for differentiating heterogeneous freezing due to an added material from freezing due to contaminants in the water and the substrate. For comparison, the coldest freezing event recorded by this equipment in experiments shown in Chapter 7 is 257 K. The expected fraction frozen for 1 μl droplets calculated using the parameterisation of Murray *et al.*[29] is provided. From Whale *et al.*[138].

3.3.Summary and conclusions

A new cold stage was constructed for the observation and analysis of liquid droplet freezing. The updated stage provides a faster, more reliable and simplified experimental process. Changes to the equipment have resulted in a more thermally stable configuration and increased data quality through more accurate temperature measurement and higher droplet numbers. After calibration of the stage the temperature accuracy 1 K min^{-1} has been estimated at ±0.3 K.

After an experiment has been performed, statistical analysis is required and is described in detail in the following chapter.

Chapter 4. Numerical analysis of freezing

In this chapter the numerical analysis of droplet freezing experiments is described. After the measurement of the freezing time and size of each droplet (see the previous chapter), the data goes through a number of steps and processes. Briefly, these steps consist of converting the freezing times into freezing temperatures, after which fraction frozen plots are produced. Average droplet volumes are then calculated, which allows the calculation of nucleation coefficients; a schematic detailing the analysis steps is shown in Figure 4.1. There are a number of methods for estimating the volume of liquid, and the affect these methods have upon the resulting nucleation coefficients is detailed in section 4.3. In the calculation of nucleation rate coefficients it is necessary to make two assumptions, and the accuracy of these assumptions is investigated in section 4.4.

4.1.Processing of experimental data

The experimental process generates several data streams – the diameter and freezing frame number of individual frozen droplets, a temperature time series and video frame time series.

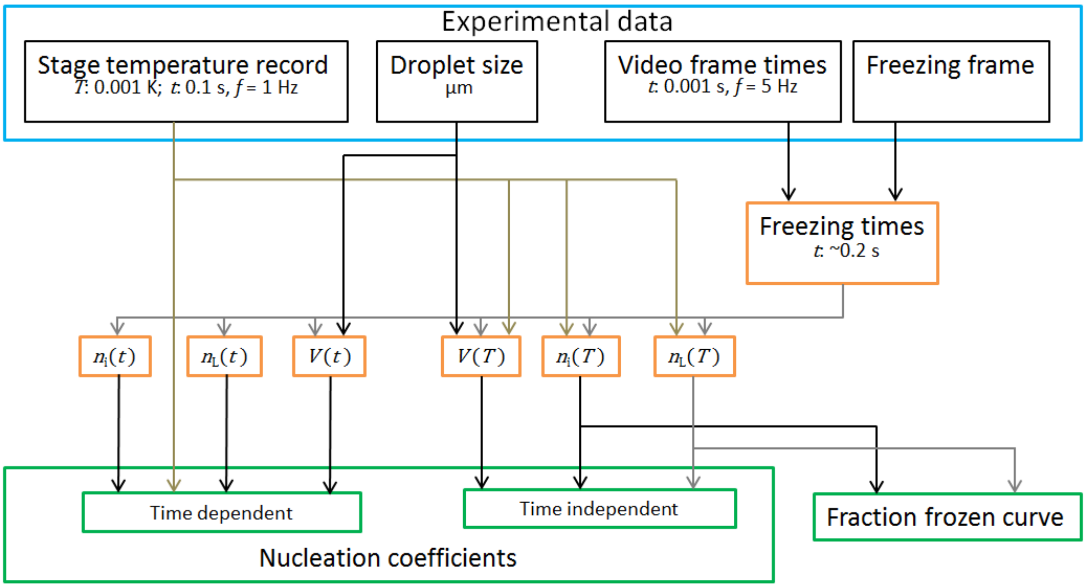

Figure 4.1. Schematic summarising the statistical analysis. The four main experimental datasets are combined to create temperature and time dependent series (denoted (T) and (t)) of freezing events and liquid droplets (n_i and n_L), which are then used along with the measure of the mean droplet volume, V (converted to particle surface area in heterogeneous experiments), to calculate nucleation coefficients. Orange boxes denote intermediate data products and green boxes final data output. Flow lines are coloured for clarity.

The droplet freezing frames are converted to times by referencing the freezing frame number within the frame time record. From the freezing times the time series of the number of freezing events, $n_i(t)$ and $n_L(t)$ are then compiled. To calculate droplet freezing temperature series, $n_i(T)$ and $n_L(T)$, the freezing times are referenced against the Fluke 1524 temperature log from the experiment. However, as the temperature records are at a lower time resolution than the freezing time data (1 Hz vs. 5 Hz), a simple look-up of the corresponding temperature is not possible. Instead, times are converted to temperature by performing a linear interpolation between each temperature data point. The fraction frozen curves of $n_i(T)/n_L(T_0)$ are then calculated from the temperature based event/droplet series, where $n_L(T_0)$ is the number of droplets at the start of the experiment. The time and temperature dependent coefficients nucleation can then be calculated.

4.2. Calculation of nucleation coefficients

The first step in calculating nucleation coefficients is to estimate the quantity of nucleant in the droplets. Regardless of whether this quantity is estimated as a mass, surface area or number of particles of suspended material, the quantity of this material is dependent upon the volume of the droplets analysed. There are several methods for calculating the average droplet volume in the literature, based upon the mean[37,42,76,77,80,139,140] or median[29,41,47,75] of the initial volume distribution or by calculating a time (or temperature) series of the mean droplet volume[68]. The volumes calculated by these different methods can have an influence upon the calculated nucleation coefficients. To reduce the uncertainties that can stem from this, some authors[29,41,47,141] grouped droplets of similar sizes into a number of bins rather than performing the analysis on the droplet size distribution as a whole. The different methods of representing the droplet size average and the influence of the width of the droplet size distribution are discussed in greater detail in section 4.3.

Once the time and temperature series of volume, frozen and liquid droplets have been compiled it is possible to calculate nucleation coefficients. The time series are used for calculation of stochastic coefficients (via Equation 2.17 for homogeneous nucleation and 2.24 for heterogeneous nucleation). For calculation of the time-independent coefficients, the droplet temperature series are used and if the average droplet volume is constant then the cumulative nucleus spectra[68] (or ice-active surface site density[109], Equation 2.31) can be calculated directly from these series. If the droplet volume is not constant it is necessary to first calculate the differential nucleus spectra[68] (Equation 2.28), from which the cumulative nucleus spectra can then be calculated (Equation 2.30).

The equations from Chapter 2 discussed above are repeated here for convenience:

$$\frac{n_\mathrm{i}}{n_\mathrm{L}} = 1 - \mathrm{e}^{-J(T)V\Delta t} \qquad \textbf{Equation 2.17}$$

$$\frac{n_\mathrm{i}}{n_\mathrm{L}} = 1 - \mathrm{e}^{-J_\mathrm{het}(T)\sigma\Delta t} \qquad \textbf{Equation 2.24}$$

$$\frac{n_\mathrm{i}(T)}{n_0} = 1 - \mathrm{e}^{-n_\mathrm{s}(T)\sigma} \qquad \textbf{Equation 2.31}$$

$$\frac{n_\mathrm{i}}{n_\mathrm{L}} = 1 - \mathrm{e}^{-k(T)\sigma\Delta T} \qquad \textbf{Equation 2.28}$$

$$k(T) = \frac{\left(n_\mathrm{s}(T - \Delta T) - n_\mathrm{s}(T)\right)}{\Delta T} \qquad \textbf{Equation 2.30}$$

Equation 2.17 describes volume based homogeneous nucleation (J_hom), Equation 2.24 heterogeneous stochastic nucleation by a single component (J_het), Equation 2.31 the cumulative time-independent nucleus spectra (n_s), Equation 2.28 the differential time-independent nucleus spectra (k) and Equation 2.30 the derivation of the cumulative time-independent nucleus spectra (K) from the differential nucleus spectra. n_i is the number of droplets frozen during the time-step Δt or temperature-step ΔT, n_L is the number of liquid droplets at the start of the step, $n_\mathrm{i}(T)$ is the cumulative number of droplets frozen at temperature T, n_0 the number of droplets at the start of the experiment, V the average droplet volume and σ the average surface area of the nucleant suspended in the droplets.

To calculate the stochastic nucleation rate coefficient it is necessary to define a time-step, Δt. In choosing the time-step the objective is to maximise the number of data points by minimising the length of the time-step. The actual time-step then depends upon the time taken for the whole droplet population to freeze. When cooling at 1 K min^{-1}, experiments with freezing occurring over short temperature ranges, such as homogeneous, have time-steps typically around 2 – 4 seconds, whereas in the wider temperature range heterogeneous experiments the time-step is longer, typically 4 – 10 seconds. Occasionally there are freezing events separated from the bulk of the droplet-freezing by several time-steps and it can be necessary to exclude these early events from the experiment to maintain a small enough time-step to optimise the quantity of data. The time-independent differential nucleus spectra (Equation 2.28) is derived in a similar manner to the stochastic coefficient, with ΔT analogous to Δt, and the same optimisation process used. During the calculation of stochastic nucleation rate coefficients some assumptions are necessary, which are examined in section 4.4.

4.3. Estimation of droplet size and its influence upon nucleation coefficients

The probability of a droplet freezing is proportional to its volume (e.g. Equation 2.17), and in experiments with a droplet size distribution the largest droplets will tend to freeze earlier than smaller droplets. This causes the size distribution of the remaining liquid droplets to evolve during the experiment, with the mean droplet size gradually reducing as larger droplets freeze (Figure 4.2). Therefore, if a droplet size distribution exists care needs to be taken with how the average volume is represented. The impact of the width of the size distribution upon the magnitude of this reduction has been investigated. There are several methods for representing the droplet volume but no ‘best practice’ recommended within the literature.

4.3.1. Averaging droplets of different sizes

It is possible to represent the droplet volume with a constant mean[37,42,76,77,80,139,140] or median (the volume at which 50 % of the volume of the distribution is in smaller droplets and 50 % is in larger. E.g. refs [29,41,47,75]) of the initial distribution, a mean which is updated during the experiment (see the appendix of Vali 1971[68]) or it can be explicitly modelled through the experiment[28,81,109]. As noted above, the probability of freezing is greater for larger droplets. This implies that as freezing progresses in populations with wide volume distributions there will be a greater variation in the average volume of the remaining liquid droplets than in populations with narrow volume distributions (Figure 4.2).

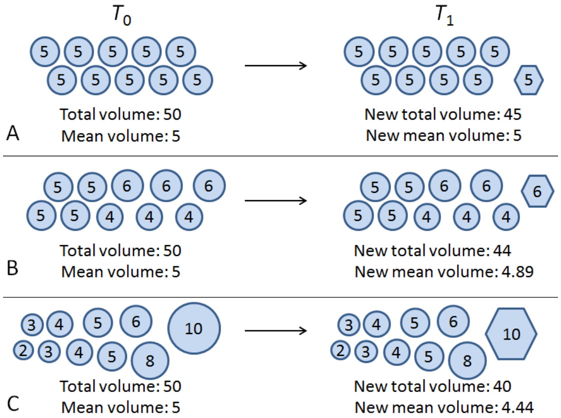

Figure 4.2. An example of how freezing can change the size distribution in different droplet populations. In the three arbitrary droplet distributions shown, the largest droplet has the highest probability of freezing (e.g. Equation 2.17) and is assumed to be the only droplet frozen on cooling to T_1. In a population of equal sized droplets (A) the mean does not change. In a narrow distribution (B) the mean changes a small amount and in the wide distribution (C) the mean changes significantly.

If an experiment contains sufficient droplets they can be separated into groups of similar sized droplets, referred to as size bins, to reduce the inaccuracies which can arise due to these representations[29,41,47,141], with the narrowest possible size bin limited to the measurement resolution[69] (referred to as the 'measurement-bin' here).

As part of the work in Chapter 6, a homogeneous experiment containing a large number of droplets is described. This experiment included more than six hundred droplets in seven measurement-bins 2.5 µm wide, with bin centres ranging from 5 to 20 µm (Table 4.1). The large number of droplets throughout this distribution allows a thorough investigation of the effects of four different averaging methods, specifically: the constant median and mean of the whole width of the initial size distribution; a mean of the size distribution recalculated after each time/temperature-step (updating mean); and grouping the droplets into the narrowest possible size bin – the measurement-bin. Using homogeneous experimental data allows for analysis of these methods without the need to deal with additional complications from factors which could be experienced in heterogeneous experiments, such as particle size distributions.

Each averaging method has associated assumptions about the droplet population. The constant mean and median both assume that the droplet volume distribution does not change during the experiment. In both of the constant averages and also the updating mean, it is assumed that the nucleating ability of each droplet scales directly with volume, which may not always be the case. For example, if both the surface and volume of the droplet are contributing to nucleation (see Chapter 6), the probability of freezing will not scale directly with volume and averaging a volume distribution is not appropriate. Alternatively, calculating nucleation coefficients for the narrow size distributions of each measurement-bin separately would not only minimise the effects of the volume-scaling assumption, but may reveal detail in situations where this assumption is not appropriate.

Bin width	Number	Volume (10^{-10} cm^3)	$\ln(J)$ parameterisation
5.0 ±1.25 µm	135	0.42	$-3.908T + 938.24$
7.5 ±1.25 µm	151	1.40	$-4.226T + 1012.6$
10.0 ±1.25 µm	123	3.33	$-3.969T + 952.35$
12.5 ±1.25 µm	93	6.50	$-4.103T + 983.65$
15.1 ±1.25 µm	63	11.23	$-4.512T + 1080.2$
17.6 ±1.25 µm	45	26.63	$-3.804T + 913.43$
20.1 ±1.25 µm	23	37.91	$-6.591T + 1570.2$
3.75 – 21.35 µm, constant median	633	9.31	$-2.781T + 671.14$
3.75 – 21.35 µm, constant mean	633	5.38	$-2.781T + 671.69$
3.75 – 21.35 µm, updating mean	633	0.42 – 5.38	$-4.362T + 1044.8$

Table 4.1. Details of droplet distribution and volumes. For the updating mean the volumes provided are the initial mean volume and smallest droplet volume in the experiment.

A direct comparison of *J* values calculated using the four averaging methods described above is shown in Figure 4.3. The influence of the averaging methods is seen in the offsets between, and different curvature of, each data set. Assuming that wider bins will increase the deviation of the average volume from the actual volume, *J* values calculated using droplets in measurement-bins will be the most accurate. Therefore, if sufficient droplets are available and it can be assumed that the probability of freezing in different droplet sizes scales with volume alone, using the measurement-bins is the best option. If this is not the case, a decision needs to be made on which one of the remaining averaging methods is used.

Inspection of Figure 4.3 suggests that, of the three droplet averaging methods, the updating mean is the most consistent with the measurement-binned data. This is an outcome supported by Vali in 1971[68], who stated that experiments with poly-disperse droplet populations are best analysed by either collecting droplets into groups with nominal volumes (e.g. the measurement-bins used here), or using a time/temperature series of the mean volume. In contrast, deviations can be seen when the constant mean and median are used.

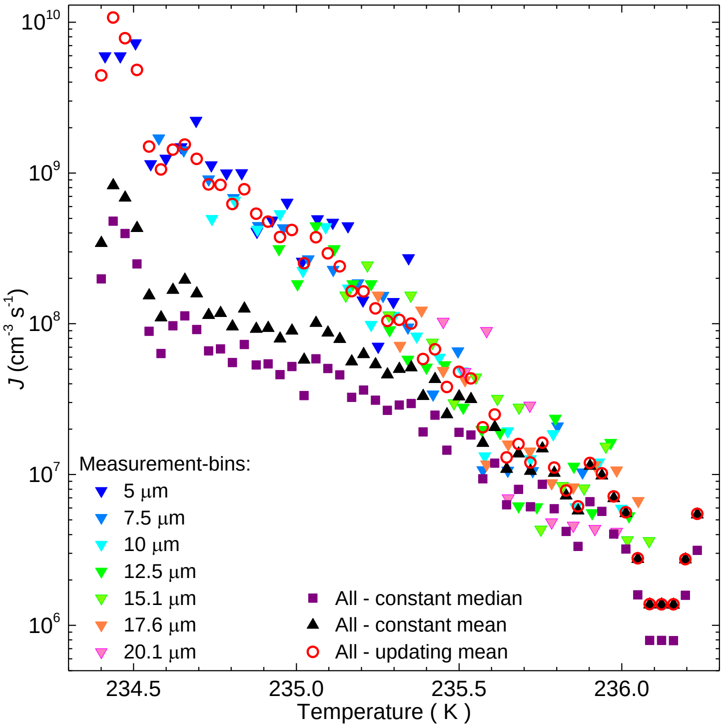

Figure 4.3. A comparison of nucleation rate coefficients calculated from the different droplet size averaging methods. The experiment starts at higher temperatures and proceeds, right to left, to lower temperatures. The legend labels refer to the bin widths in Table 4.1, with ‘All’ referring to the 3.75 – 21.35 µm wide bin.

At the beginning of the experiment, all four methods are numerically similar, but the methods utilising constant averages deviate from the updating mean and measurement-binned data. This deviation is caused by changes in the volume distribution of the droplets by larger droplets freezing early in the experiment, and as the experiment progresses the width of the volume distribution narrows. The constant averaging methods cannot account for the change in volume distribution, resulting in the artificial curvature at lower temperatures. At the end of the experiment, the updating and constant means are more than an order of magnitude apart, which is similar to the difference between the smallest and mean droplet volumes of the updating mean (Table 4.1). There is an additional variation of ~75% between the constant mean and median, caused by the non-normal volume distribution. The value of the difference the mean and median is dependent upon the shape of the volume distribution of the droplets (e.g. the more normal a distribution is, the smaller the difference and vice versa) and will vary between experiments.

4.3.1.1. Constant vs. updating mean

The cause and impact of the differences between the constant and updating averaging methods can be investigated mathematically. In the case of homogeneous nucleation, Equation 2.17 is revised by making the average droplet volume a function of temperature:

$$\frac{n_{\mathrm{i}}}{n_{\mathrm{L}}} = \left(1 - \mathrm{e}^{-J(T)V_{\mathrm{um}}(T)\Delta t}\right) \qquad \textbf{Equation 4.1}$$

where $V_{\mathrm{um}}(T)$ is the updating mean volume.

The effect upon J of using a constant rather than updating volume can be shown by equating Equation 2.17 and Equation 4.1 and then simplifying using the same fraction frozen and time-step (Equation 2.17 is on the left):

$$\mathrm{e}^{-J(T)V_{\mathrm{cm}}\Delta t} = \mathrm{e}^{-J(T)V_{\mathrm{um}}(T)\Delta t}$$

$$J(T)V_{\mathrm{cm}} = J(T)V_{\mathrm{um}}(T) \qquad \textbf{Equation 4.2}$$

with the subscripts cm and um referring variables calculated from the constant and updating mean droplet volumes respectively. Substituting in the ln-linear estimation of $J(T)$ from Equation 2.14 and rearranging:

$$V_{\mathrm{cm}}\mathrm{e}^{(a_{\mathrm{cm}}T+b_{\mathrm{cm}})} = V_{\mathrm{um}}(T)\mathrm{e}^{(a_{\mathrm{um}}T+b_{\mathrm{um}})}$$

$$\mathrm{e}^{(a_{\mathrm{cm}}T+\ln V_{\mathrm{cm}}+b_{\mathrm{cm}})} = \mathrm{e}^{(a_{\mathrm{um}}T+\ln V_{\mathrm{um}}(T)+b_{\mathrm{um}})}$$

$$a_{\mathrm{cm}}T + \ln V_{\mathrm{cm}} + b_{\mathrm{cm}} = a_{\mathrm{um}}T + \ln V_{\mathrm{um}}(T) + b_{\mathrm{um}} \qquad \textbf{Equation 4.3}$$

As the relationship between volume and temperature is not linear, the effects upon a and b, Δa and Δb, are approximate. Δa is derived by differentiating both sides of Equation 4.3 with respect to temperature, and Δb from the observation that the two averages produce the same value of J at the start of the experiment:

$$\Delta a = a_{\mathrm{cm}} - a_{\mathrm{um}} \approx \frac{\left(\ln(V_1) - \ln(V_{\min})\right)}{\Delta T} \qquad \textbf{Equation 4.4}$$

$$\Delta b = b_{\mathrm{cm}} - b_{\mathrm{um}} \approx \Delta a T_1 \approx \frac{\left(\ln(V_1) - \ln(V_{\min})\right)}{\Delta T} T_1 \qquad \textbf{Equation 4.5}$$

with V_1 and T_1 representing the mean volume and temperature at the beginning of the experiment, $V_{\min}$ the volume of the smallest droplet in the experiment representing the smallest possible mean volume, and ΔT the temperature difference between the first and last freezing events. The effect of using a constant average can be quite marked - estimated using Equation 4.4 Δa is -1.35 (updating vs constant mean in Figure 4.3, ΔT = -1.8, V_0 and $V_{\min}$ as per the updating mean in Table 4.1). In comparison, the actual ln(J) linear fits in Table 4.1 give Δa = 1.6 (using a_{um} - a_{cm}), suggesting that Equation 4.4 is a good estimator of inaccuracy caused by using a constant mean.

When deriving Equation 4.2, it is noteworthy that the time-step disappears from the equation. As the time-step is the principle difference between the stochastic and singular nucleation coefficients, its absence means that Equation 4.4 and Equation 4.5 apply to both coefficients. Additionally, as heterogeneous nucleation coefficients are derived from droplet volume, these estimations can be used for heterogeneous experiments. However, heterogeneous experiments tend to extend over a considerably wider range of temperatures than homogeneous, and a larger ΔT will reduce the impact of using a constant average. The connection between Δa and ΔT is demonstrated in Figure 4.4.

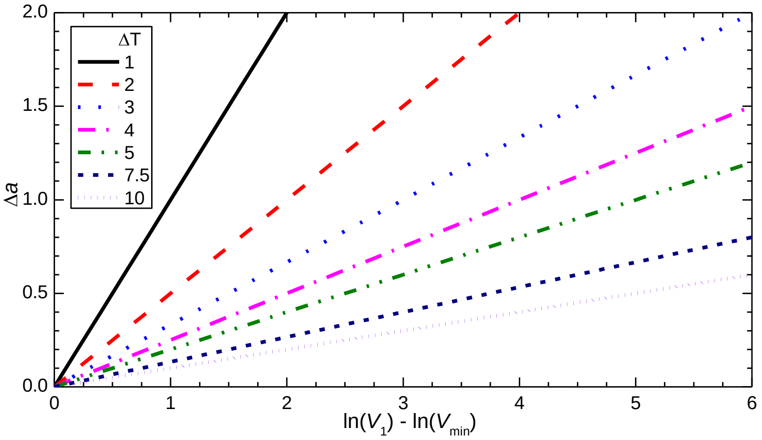

Figure 4.4. The effect of a volume distribution upon the fitted slope of J. The value of Δa calculated using Equation 4.4 for a range of volume distributions ($\ln(V_1) - \ln(V_{\min})$) and experimental temperature durations (ΔT). The natural logs of the volumes in Table 4.1 range from -23.9 to -19.4, and V_1 for the updating mean is -21.3. Typical values of ΔT are ~2 K for homogeneous experiments and ~4 – 7 K for heterogeneous.

4.3.1.2. Constant mean vs. median

In some experimental situations, it may be impossible to record the variations of droplet size with time/temperature. In analytical systems which sample large numbers of droplets but can only detect if droplets are frozen or not, such as in flow tube experiments (e.g. ref [79]), knowledge of the changes in the droplet size distribution is not available. In such cases, as only the initial size distribution of the droplets added to the chamber is known, using a constant volume in the form of a mean or a median may be necessary. Similarly to Equation 4.3 to Equation 4.5, for the same fraction frozen, temperature and time-step, the difference caused by using a constant median can be calculated. As both averages are constant the temperature dependent variables, a_{med} and a_{mean}, are assumed equivalent:

$$V_{\mathrm{mean}}\mathrm{e}^{(a_{\mathrm{mean}}T+b_{\mathrm{mean}})} = V_{\mathrm{med}}\mathrm{e}^{(a_{\mathrm{med}}T+b_{\mathrm{med}})}$$

$$\mathrm{e}^{(a_{\mathrm{mean}}T+b_{\mathrm{mean}}+\ln(V_{\mathrm{mean}}))} = \mathrm{e}^{(a_{\mathrm{med}}T+b_{\mathrm{med}}+\ln(V_{\mathrm{med}}))} \quad \textbf{Equation 4.6}$$

$$\Delta b = b_{\mathrm{mean}} - b_{\mathrm{med}} = \ln(V_{\mathrm{med}}) - \ln(V_{\mathrm{mean}}) \quad \textbf{Equation 4.7}$$

with the median and mean denoted by the subscripts med and mean. The difference between the mean and median volume is manifested in the non-temperature dependent component, b, as the natural log difference of the mean and median. In the case of Figure 4.3 Δb = 0.55, explaining the variation between the values of b shown in Table 4.1.

While Figure 4.3 indicates that the constant mean is closer to the measurement-bin dataset than the constant median, it does not definitively show which is most appropriate. However the measurement-bin data uses the volume calculated from the diameter in the centre of the bin and may not be the most appropriate comparison to judge between the constant mean and median. Again, this question can be resolved mathematically, by rearranging Equation 4.1, and substituting the Taylor series approximation of $\ln(1-x) = -x$ if $x < 0.1$[37]:

$$J = \frac{-\ln\left(1 - \frac{n_{\mathrm{i}}}{n_{\mathrm{L}}}\right)}{V\Delta t} = \frac{n_{\mathrm{i}}}{n_{\mathrm{L}}V\Delta t} \quad \textbf{Equation 4.8}$$

The relationship between J and n_{i} now depends upon $n_{\mathrm{L}}V$, the total liquid volume, for which V must be the mean not the median. Therefore, if a constant average has to be used this should always be the mean.

4.3.1.3. Recommended droplet averaging method

In summary, a mathematical analysis has been performed to guide the choice of the droplet averaging method. Where the droplet volume is constant, a constant mean is most appropriate. If the droplet volume varies during the experiment the validity of using a constant mean cannot be assured and should be tested for every size bin of every experiment. If the evolution of the droplet/particle size distribution during the experiment is not available Equation 4.4 provides a framework for establishing appropriate size bins. The width of size bins should be minimised to reduce the artificial curvature in J due to the changing droplet size distribution, and where possible it is recommended that size bins are adjusted such that Δa is no more than 10% of the actual value of a.

Estimations of this effect are shown in Table 4.2. Included are a range of size bins from the homogeneous experiment provided in this work, along with examples from the literature. The values of Δa from the homogeneous experiment in this work show that as the width of the bin increases the difference between a constant and updating mean increases. Two narrow bins both two measurement-bins wide – 5 µm –and are shown, one with small (row 3.75 – 8.75) and one with large (row 16.35 – 21.35) diameters. In the small diameter example Δa is ~10 % of a, whereas in the large diameter example it is ~4 % even though the bin width in both of these examples is 5 µm. This demonstrates that the effect upon a is due to the volume rather than size distribution, and this effect is also seen in the literature.

Bin width (µm)	Reference	Volume (10^{-10} cm^3)	ln(J_{cm})	ln(J_{um})	Δa Equation 4.4	Δa From ln(J)
3.75 – 8.75	Hom., this work	0.94 - 0.42	$-3.973T + 953.07$	$-4.422T + 1058.8$	0.525	0.449
3.75 – 11.25	Hom., this work	1.66 - 0.42	$-3.549T + 853.26$	$-4.402T + 1054.2$	0.847	0.853
3.75 – 21.35	Hom., this work	5.38 - 0.42	$-2.781T + 671.69$	$-4.362T + 1044.8$	1.398	1.581
16.35 – 21.35	Hom., this work	20.50 - 17.65	$-3.995T + 958.14$	$-4.217T + 1010.6$	0.181	0.222
3.75-6.25 + 18.85-21.35	Hom., this work	4.23 - 0.42	$-2.404T + 582.86$	$-4.349T + 1041.8$	1.410	1.945
10-20	Hom. exp. 2, Murray *et al.*[29]	15.35 - 3.29	$-2.696T + 652.14$	-	1.111	-
21-40	Hom. Exp. 2, Murray *et al.*[29]	82.15 - 35.07	$-2.759T + 668.74$	-	0.983	-
10-20	Kaolinite exp. vii, Murray *et al.*[41]	11.93 - 3.29	$-1.076T + 269.85$	-	0.237	-
21-40	Kaolinite exp. vii, Murray *et al.*[41]	74.94 - 35.07	$-0.782T + 198.20$	-	0.190	-
10-20	NX illite exp. 2, Broadley *et al.*[47]	15.28 - 3.29	$-0.230T + 65.97$	-	0.205	-
21-30	NX illite exp. 2, Broadley *et al.*[47]	61.19 - 35.07	$-0.386T + 103.38$	-	0.133	-

Table 4.2. Summary of sample Δa values from this work and the literature. Δa values are calculated using Equation 4.4 or by a comparison of a calculated using fits to the constant and updating means (i.e. $a_{cm} - a_{um}$). For homogeneous data Δa is numerically large except in the narrowest volume distribution (16.35 – 21.35 µm), and small for heterogeneous experiments (Kaolinite and NX illite) due to the wide range of freezing temperatures in these experiments. The volumes shown are the mean droplet volume at the start and the smallest droplet in the experiment. Droplet volumes were calculated from the diameter of the measurement-bin centre.

For example, a homogeneous experiment[29] from the literature has similar values of Δa to the experiment described here. The values of Δa from heterogeneous experiments[41][47] are much smaller than homogeneous due to the wider temperature range of freezing in these experiments – heterogeneous experiments tend to occur over 4 – 7 K and homogenous over ~2 K. However, in heterogeneous experiments Δa is still significant at 20 to 90 % of the fitted value of a. Therefore, the effect of droplet volume measurements on Δa is important in all experiment types. Where information on the evolution of the droplet size distribution is available, the mean droplet volume should be calculated using droplets the narrowest size bins possible (i.e. the measurement-bin) or using an updating mean if data is sparse. Nucleation coefficients in Chapter 6 and 7 are calculated using these methods.

4.3.2. Uncertainty due to droplet size measurement resolution

Having seen in section 4.3.1 that errors in the representation of droplet volumes can have significant effects, it is prudent to investigate whether the resolution of droplet size measurements could cause a similar problem. This is especially relevant to the work on homogeneous nucleation discussed in Chapter 6, in which subtle differences between the nucleation rate coefficients of individual measurement-bins are involved. To facilitate testing the droplet size distribution of the experiment shown in Figure 4.3 is interpolated into ~0.25 µm wide sub-sections (a tenth of the measurement resolution) by assuming that the droplet size distribution is continuous and linear (see Figure 4.5 and Table 4.3). While the absolute volumes and surface areas of each droplet size do not change significantly, there are relative changes between the different sizes. For instance, the interpolated volume of 5 µm size is 7 % larger than the non-interpolated volume, while for 20 µm droplets the interpolated volume is 2 % smaller.

Diameter (µm, ±1.25)	Volume (10^{-10} cm^3)	Interpolated vol. (10^{-10} cm^3)	Volume Ratio	Surface area (10^{-6} cm^2)	Interpolated SA (10^{-6} cm^2)	SA Ratio
5.0	0.4161	0.4480	1.077	0.8478	0.8736	1.030
7.5	1.4043	1.4374	1.024	1.9075	1.9204	1.007
10.0	3.3286	3.3312	1.001	3.3912	3.3756	0.995
12.5	6.5012	6.4615	0.994	5.2987	5.2598	0.993
15.1	11.234	11.139	0.992	7.6301	7.5697	0.992
17.6	17.839	17.645	0.989	10.386	10.293	0.991
20.1	26.629	26.095	0.980	13.565	13.366	0.985

Table 4.3. Summary of the interpolation correction to droplet volumes and surface areas. The ratios provided are interpolated/non-interpolated; see text and Figure 4.5 for details of the interpolation process.

As well as the minor changes to the mean droplet volume and surface, the interpolation has produced a simplistic approximation of the size distribution within the measurement-bin. Using Equation 4.4 the effect a droplet size distribution has upon the parameterisation of J can be estimated (Table 4.4). In the measurement-bins 10 µm or larger, the effect of this size distribution upon a is minor (~6 – 7 %). However in the smallest two sizes the effect is more pronounced and the change in a for the 5 µm measurement-bin is 23 %.

4.4. Stochastic nucleation rate coefficient assumptions

During the calculation of the stochastic nucleation rate coefficients two additional assumptions are made: the temperature dependence of the pre-exponential is minimal, and that the change in J over the analysis time-step is not significant.

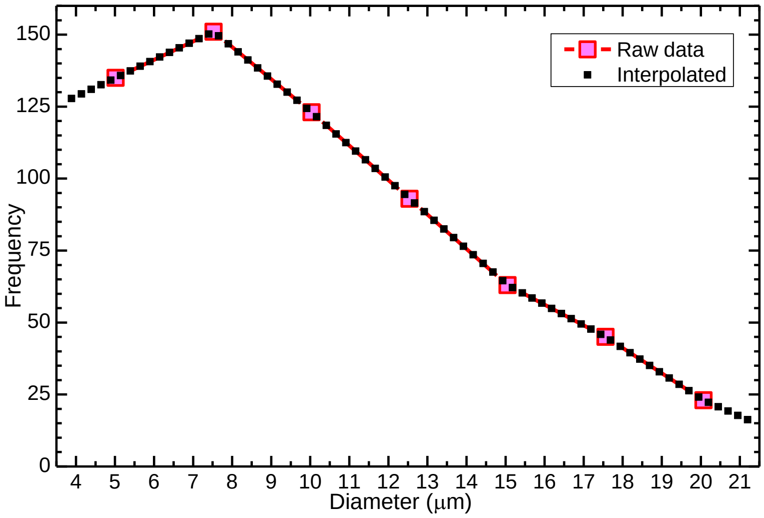

Figure 4.5. Interpolation of droplet diameter. Linear interpolations were performed using the gradient between actual data points; below 5 µm the gradient from 5 – 7.5 µm was used, above 20µm the number of droplets recorded at 22.5 µm was used. After interpolation the droplet frequencies were normalised to the original total number of droplets.

Diameter (µm, ±1.25)	Mean Interp. Vol (10^{-10} cm^3)	Min. Interp. Vol (10^{-10} cm^3)	ln(J_{cm})	Δa	a_{um}
5.0	0.4480	0.1937	$-4.028T + 966.5$	0.900	-4.928
7.5	1.4374	0.8624	$-4.245T + 1017.1$	0.392	-4.637
10.0	3.3312	2.3268	$-4.008T + 961.4$	0.285	-4.293
12.5	6.4615	4.8991	$-3.771T + 905.6$	0.257	-4.028
15.1	11.139	8.8912	$-4.334T + 1038.3$	0.242	-4.576
17.6	17.645	14.615	$-3.541T + 851.4$	0.236	-3.777
20.1	26.095	22.383	$-6.635T + 1580.7$	0.288	-6.923

Table 4.4. An estimation of the effect of the droplet measurement-bin upon the parameterisation of J. The diameters and mean interpolated volumes are as shown in Table 4.3 and ln(J) recalculated from experimental data based upon the mean interpolated volume. The minimum interpolated volume is the volume calculated for the smallest tenth-of-bin sub-section from each bin. a_{um} is calculated as a_{cm} - Δa.

4.4.1. Pre-exponential temperature independence assumption

In the use of the stochastic model it is usually assumed that the pre-exponential term in Equations 2.9 and 2.23 is constant over the range of droplet freezing temperatures. This assumption is necessary to allow the investigation of the terms residing within the exponential (e.g. calculation of the ice cluster-liquid surface energy using Equation 2.19). Denoting the pre-exponential and exponential terms as the temperature dependent functions $A(T)$ and $\beta(T)$ respectively, Equation 2.9 becomes:

$$J(T) = A(T)\mathrm{e}^{(\beta(T))}$$

$$J(T) = \mathrm{e}^{\left(\beta(T)+\ln(A(T))\right)}$$ **Equation 4.9**

Even though the temperature dependence of $\beta(T)$ is non-linear, as the temperatures are in Kelvin the relative change over a range of a few degrees is small. Therefore, similarly to Equation 2.14 (note a from this equation has become α here for clarity), Equation 4.9 can be approximated as log-linear:

$$J = \mathrm{e}^{(\alpha T+\ln(A_0))}$$ **Equation 4.10**

where A_0 is the pre-exponential factor at $T = 0$ and α is the temperature dependence of J:

$$\alpha = \frac{\mathrm{d}\beta(T)}{\mathrm{d}T} + \frac{\mathrm{d}\ln(A(T))}{\mathrm{d}T}$$ **Equation 4.11**

in which it is assumed that there is no influence on J from the droplet volume distribution (e.g. Section 4.3.1). Over the range of temperatures relevant to a single homogeneous nucleation experiment, it is typically assumed that α is constant and that $\mathrm{d}\ln(A(T))/\mathrm{d}T$ is zero. Testing of this assumption is further complicated by the existence of several proposed forms of the pre-exponential (see section 2.2.3.1), repeated here for convenience:

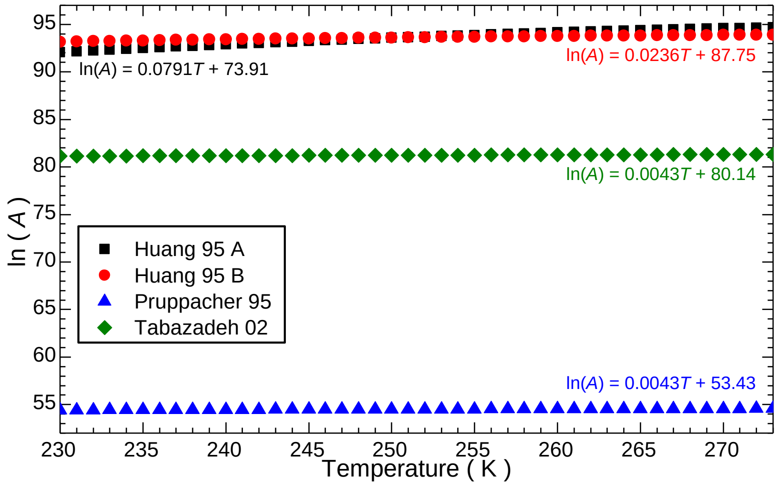

Figure 4.6. Estimations of the pre-exponential of J. The forms of the pre-exponential are from Huang and Bartell[58] (A = Equation 2.10, B = Equation 2.11), Pruppacher[62] (Equation 2.12) and Tabazadeh, Djikaev and Reiss[44] (Equation 2.13). Parameterisations of ln(A) for each form are provided.

$$A_{\mathrm{hom}} = \frac{2(\gamma_{\mathrm{iL}} kT)^{½}}{v^{5/3}\eta}$$ Equation 2.10 (Huang 95 A[58])

$$A_{\mathrm{hom}} = \left(\frac{5f}{cv^{⅔}}\right)\left(\frac{3\gamma_{\mathrm{iL}}}{m}\right)^{½}[1-S]$$ Equation 2.11 (Huang 95 B[58])

$$A_{\mathrm{hom}} = \left(\frac{\rho_{\mathrm{L}} kT}{\rho_{\mathrm{ice}} h}\right)\left(\frac{\gamma_{\mathrm{iL}}}{kT}\right)^{½}$$ Equation 2.12 (Pruppacher 95[62])

$$A_{\mathrm{hom}} = \frac{N_{\mathrm{L}} kT}{h}$$ Equation 2.13 (Tabazadeh 02[44])

The resulting values of the pre-exponential from these equations are shown in Figure 4.6. For all four versions of the pre-exponential $\mathrm{d}\ln(A(T))/\mathrm{d}T$ is less than 0.1. As literature values of a are significantly less than -2, using Equation 4.11 shows that it is appropriate to assume the pre-exponential is constant.

4.4.2. Nucleation rate coefficient change during the time-step assumption

To facilitate the calculation of the stochastic nucleation rate coefficients the experiment is split into a series of independent but short constant temperature time periods (Δt, Equations 2.17 and 2.24). The resultant value of J calculated from the observations corresponds to the centre of Δt. In a true constant-temperature experiment this is equivalent to the actual value of J, but in a cooling experiment this approach requires the assumption that the observed value of J is equivalent to the mean value over Δt. As the change of J over Δt is not linear, the accuracy of this assumption will depend upon the change of temperature, ΔT, during Δt and the temperature dependence of J. Using the simplified representation of J in Equation 2.14, the value of J observed at the centre of Δt is:

$$J_{\mathrm{obs}} = \mathrm{e}^{(aT+b)}$$ **Equation 4.12**

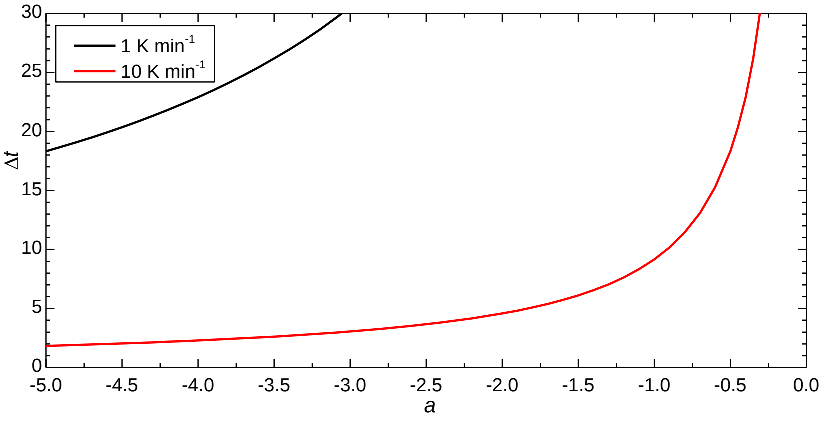

Figure 4.7. The maximum acceptable value of Δt with a, the temperature dependence of J, for two different cooling rates. The plotted lines show values of Δt calculated by Equation 4.14 corresponding to a 10 % difference between the theoretical and average value of J.

Integrating J over the temperature step allows calculation of the mean value over the time step:

$$J_{\mathrm{mean}} = \frac{1}{\Delta T} \int_{T-\frac{\Delta T}{2}}^{T+\frac{\Delta T}{2}} \mathrm{e}^{(aT+b)}\, dT$$ **Equation 4.13**

Completing the integral and dividing by Equation 4.12 reveals the following relationship:

$$\frac{J_{\mathrm{mean}}}{J_{\mathrm{obs}}} = \frac{1}{a\Delta T}\left(\mathrm{e}^{\frac{a\Delta T}{2}} - \mathrm{e}^{\frac{-a\Delta T}{2}}\right)$$ **Equation 4.14**

By defining the maximum acceptable error in J_{mean} as 10% (e.g. $J_{\mathrm{mean}}/J_{\mathrm{obs}} = 1.1$), Equation 4.14 can be solved iteratively. This gives a maximum value of $a\Delta T = 1.527$, above which this assumption is inaccurate. Using the cooling-rate relationship between Δt and ΔT allows calculation of acceptable values of Δt (Figure 4.7). In homogeneous experiments a is generally less than -2, so this assumption limits Δt to 18 seconds maximum at 1 K min^{-1}. The experiment shown in Figure 4.3 has $a\Delta T \approx 0.2$, giving $J_{\mathrm{mean}}/J_{\mathrm{obs}} = 1.002$, equivalent to a 0.2% error. For homogeneous experiments at 10 K min^{-1} care needs to be taken to ensure this assumption does not become a problem – for $a = -4$, Δt should be no greater than 2 seconds. For heterogeneous experiments $-2 < a < 0$ is usually the case, which allows greater freedom in deciding Δt. For the homogeneous experiments in Chapter 6 this assumption has no impact.

4.5. Summary

The numerical process for the analysis of freezing data has been described, in which the freezing times and temperatures are combined with the sizes of frozen droplets to calculate the temperature and time series of liquid and frozen droplet numbers. From these series the time dependent and independent nucleation coefficients can be derived. This requires a representation of the average droplet volume, and there are several methods that can be used to estimate it. Unless the volume distribution of the droplets is very narrow, the droplet averaging method used can have a significant impact on the calculated nucleation coefficients. In all cases where the grouping of droplets of different sizes is made it is recommended that the mean droplet volume should be recalculated after every time-step. Finally, an analysis of the two main assumptions made during the calculation of nucleation rate coefficients has been performed. Neither of these assumptions was found to invalidate the calculation method, and acceptable limits to the analysis time-step have been defined.

Chapter 5. Mineral dust characterisation

A principle aim of this project is to identify the ice nucleating ability of mineral dusts relevant to the atmosphere. Fundamental to this aim is the need to acquire mineral specimens which are of high purity, which can be quantified using X-Ray powder diffraction. Once this technique has identified a sample of sufficient purity, the surface area to mass ratio, termed the specific surface area, of the dust needs to be quantified to allow the calculation of surface area normalised nucleation coefficients. This specific surface area can be measured using gas adsorption techniques (section 5.2).

The X-ray diffractometer was operated by Dr T.L. Malkin, who performed all steps of the procedure; the author contributed to the XRD analysis by assisting with the identification of minerals likely to be present in samples. Gas adsorption measurements were produced at Leeds by the Particles-CIC group in the Faculty of Engineering and the School of Chemistry.

5.1.Mineralogy by X-ray powder diffraction

When X-rays are incident upon an electron, the electric field of the X-ray causes the electron to oscillate[142]. This oscillation causes the electron to emit X-rays in all directions, at the same frequency as the original X-ray. If a beam of X-rays is directed upon a crystalline substance, the X-rays emitted by the electrons of atoms in the crystal will create constructive and destructive interferences at angles in three dimensions around the crystal[142]. The directions of the constructive interferences from crystals can be detected, and are related to the distance between atoms by Braggs law[142]:

$$2d \sin\theta = n\lambda$$ **Equation 5.1**

where d is the distance between interfering atoms, θ is the angle formed between the incident (and emitted) X-ray and a plane perpendicular to a line intersecting the two atoms (see Figure 5.1), and n is an integer number of X-ray wavelengths λ. With λ typical to this method of analysis (0.154 nm[142]) the distances between electrons in a single atom are not significant, and knowing θ and λ enables the derivation of the positions of the atoms within a crystal. In a single crystal, the constructive interferences create a pattern of points around the main X-ray beam. In a powdered sample containing many micron and sub-micron sized crystals of random orientation, the constructive interferences form rings around the central beam. In modern instruments, the detector traverses the radius of the rings to produce the spectra.

The direct analysis of the mineralogical composition of samples can be done using a Rietveld analysis, which fits the observed spectra by the summation of standard XRD spectra for a number of minerals to achieve a best fit. However, this is generally prohibitive in terms of time; instead the composition of mineral samples can be analysed using a relative intensity ratio method[143,144]. In this method the sample is doped with a known amount of a standard, in this case with ~20 % by mass of corundum which is rare in natural samples. By comparing the intensities (i.e. the area under the peak) of peaks due to the added corundum with peaks from the other minerals in the sample a reasonably accurate composition of the sample can then be gained:

$$\frac{I_x}{I_s} = k\frac{m_x}{m_s}$$ **Equation 5.2**

In this general case I_x and I_s are the peak intensities for mineral x and the standard, k is the relative intensity ratio between the peak intensities and m_x and m_s are the mass fractions of mineral x and the standard[144]. Rearranging Equation 5.2 and using a corundum standard allows quantification of the mass concentration of the mineral content[144]:

$$m_x = \frac{m_{\text{cor}}}{k_{\text{cor}}}\frac{I_{(hkl)x}}{I_{(113)\text{cor}}}$$ **Equation 5.3**

in which m_{cor} is the mass concentration of corundum, $I_{(113)\text{cor}}$ is the intensity of the 113 corundum peak (~43.5 degrees in Figure 5.2), $I_{(hkl)x}$ is the intensity of a particular peak of the mineral and k_{cor} is the relative intensity ratio of the mineral peak to the 113 corundum peak[144].

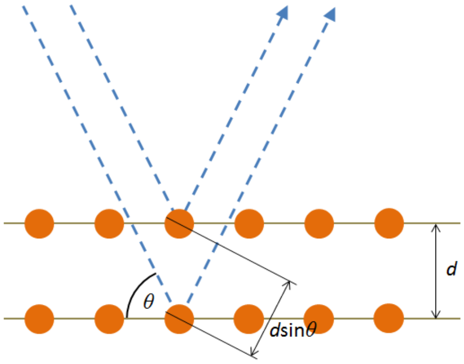

Figure 5.1. Schematic of X-ray diffraction. Incoming X-rays (top left) are incident upon atoms (orange circles) of the crystal structure. The electrons of these atoms emit X-rays of the same frequency as the incoming rays in all directions. At certain incident angles (θ), $2d\sin\theta$ is equal to an integer number of X-ray wavelengths and constructive interference occurs. By controlling the position of the detector (and source) θ is observed and d can be derived. As well as the adjacent atoms shown, these diffractions will exist for all atom pairs.

Prior knowledge of k_{cor}, which is dependent upon the equipment used, is required and can be measured independently of the sample under analysis. For common X-ray diffractometers values of k are already available for most minerals and standards.

The mineralogies derived in Chapter 7 were performed using the relative intensity methodology described by Hillier[143,144]. Briefly, the sample is thoroughly mixed with around 20 % by mass of accurately measured corundum. It is then packed into a sample holder and placed into the XRD. The sample holder is rotated continuously during analysis to reduce the possibility of specific peaks being enhanced. The resulting diffraction peaks can be used to identify and quantify the minerals in the powder. The position and intensity of each peak of the individual minerals relative to corundum need to be known before the analysis (Table 5.1).

Mineral	Peak 2θ	Peak k	NX Illite composition (Figure 5.2)
Corundum	25.6 35.2 37.8 43.5 52.6 57.6 66.8 68.4	0.55 0.88 0.38 1.00 0.45 0.92 0.36 0.55	20.0/0.0
Barite	25.89 22.85 28.78	1.80 0.92 1.79	-
Calcite	29.46	2.82	1.6/2.0
Chlorite	12.50 10.89	0.4 0.71	-
Gypsum	14.76	0.84	-
Halite	31.71 45.56	3.98 2.51	-
Illite	26.59 8.84	0.49 0.31	46.8/58.5
Illite-smectite	19.94	0.45	10.7/13.3
Kaolinite	12.34 24.86	0.64 0.51	5.6/7.0
K-feldspar	27.51 41.80	0.92 0.19	6.3/7.9
Na-feldspar	27.95 22.04	1.61 0.48	1.3/1.6
Quartz	26.68 20.84 50.39	3.82 0.76 0.52	5.1/6.4

Table 5.1. Reference peak 2θ diffraction angles and intensity ratios relative to corundum (k) for a number of common minerals. Where multiple peaks are available for a mineral, the composition is calculated for each peak and averaged. The value of k is relative to the corundum 113 (43.5°) peak. Compositions calculated using Equation 5.3 for the NX Illite spectra shown in Figure 5.2 are provided: the composition including corundum (before the slash), composition excluding corundum (after the slash). See Chapter 7 for a description of the minerals.

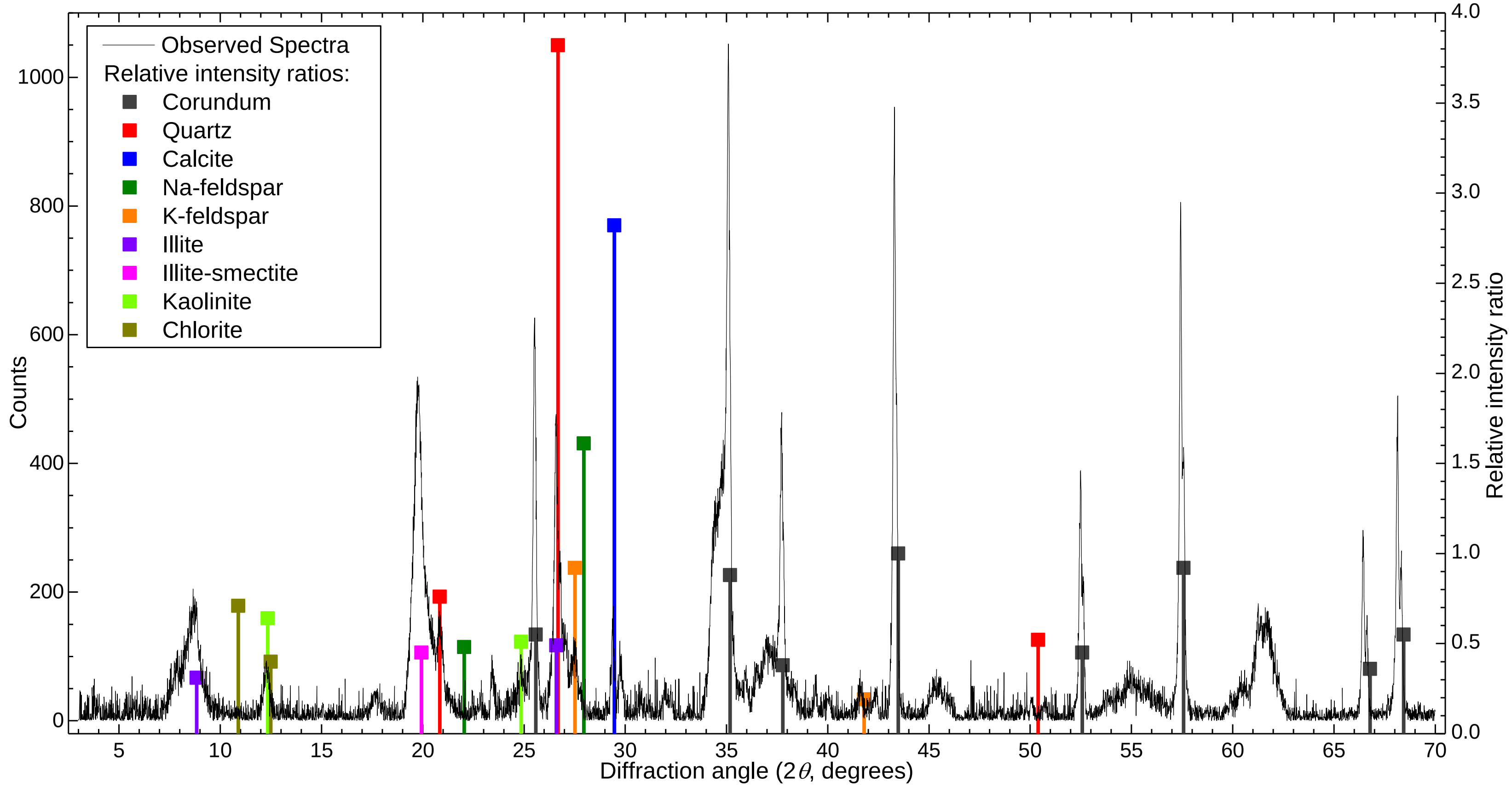

Figure 5.2. XRD spectra for NX Illite, with relative intensity ratios for several common minerals for comparison. The spectra records the number of X-ray counts (left axis, unitless) detected at each step in the diffraction angle between 3 and 70 degrees of 2θ (Figure 5.1). Sample peak 2θ and intensity ratios relative to the corundum peak at 43.5° are shown for a number of common minerals (right axis, unitless). Seven peaks for the added corundum are shown (dark grey) along with substantial peaks of illite (purple) and illite-smectite mixed layer clays (pink, see chapter 7 for mineral descriptions). The three large broad peaks at 45.5°, 55° and 61.5° are due to the sample holder. See Table 5.1 for details of the composition resulting from this spectra, and the text for a description of the instrument.

Reference peaks for most minerals are available in the literature[145], allowing calculation of the sample composition using Equation 5.2. An example of an XRD spectra of NX Illite, a commercial mixed dust[47], is shown in Figure 5.2 and the resulting composition is shown in Table 5.1.

XRD spectra were obtained using a Bruker D8, with a 2.2 kW Copper anode X-ray source and a VÅNTEC-1 detector with a resolution of 0.044°. Runs were typically performed over 2θ ranges of 3-70°, with a step size of 0.021° and 2 seconds taken per step, giving a total run-time of around 1 h 40 m. With this setup it is possible to identify the components of a sample down to around 1 % by mass, below which the noise to signal ratio is too great.

5.2. Sample surface area measurement by gas adsorption

In a closed system containing a solid surrounded by a gas, molecules of the gas will adsorb to the surface of the solid. This adsorption process increases the mass of the solid, and concurrently reduces the pressure of the gas. This pressure reduction can be related to the number of gas molecules adsorbed by the solid, and the relationship between pressure and the number of moles of gas adsorbed describe an isotherm (see Figure 5.3: non-porous). It is possible to derive the number of molecules that would be required to form a monolayer (a constant layer of molecules one molecule thick) of adsorbed gas molecules on the solid, which allows the surface area of the solid to be calculated[146]:

$$A = n_\mathrm{m} a_\mathrm{m}$$ **Equation 5.4**

where A is the surface area of the solid and n_m is the number of molecules of gas in a monolayer where each molecule occupies an area of a_m. n_m can then be calculated from pressure observations using the Brunaeuer, Emmet and Teller (BET) equation[146]:

$$\frac{1}{n\left(\frac{p}{p_0} - 1\right)} = \frac{1}{n_\mathrm{m} c} + \frac{c-1}{n_\mathrm{m} c}\frac{p}{p_0}$$ **Equation 5.5**

in which n is the amount of gas adsorbed onto the solid at a pressure of p, p_0 is the saturation vapour pressure (the pressure at which liquid forms) and c is the BET constant. By plotting $n(1-p/p_0)$ against p/p_0 (x axis), n_m and c can be calculated from the slope (s) and intercept (i) of the isotherm[146]:

$$n_\mathrm{m} = \frac{1}{s+i}$$ **Equation 5.6**

$$c = \frac{s}{i} + 1$$ **Equation 5.7**

The BET method measures the external surface area as well as any internal surfaces the gas can reach, such as pores and internal spaces in aggregates. The filling of these pores can change the rate of molecule adsorption and desorption, which can affect the calculated BET surface area, and the difference between the adsorption and desorption can be used to infer the volume and size of pores. These pores generally do not affect the isotherm at low values of p/p_0 (Figure 5.3, ref [146]), which allows for measurement of the surface area without pore filling having a significant effect upon the measured surface area.

As the BET method calculates a surface area to mass (and hence volume) ratio of the sample it can be used to calculate the radius r of a particle with the same ratio:

$$SSA = \frac{4\pi r^2}{\frac{4}{3}\pi r^3 \rho}$$

$$r = \frac{3}{SSA\rho} \qquad \textbf{Equation 5.8}$$

where SSA is the measured specific surface area in cm^2 g^{-1} and ρ the density of the substance (g cm^{-3}). As well as features such as pores, the BET method takes into account surface roughness down to molecular scales. In comparison, surface areas calculated from size measurements assuming spherical particles usually do not take into account these features and sometimes neglect the sphericity of the particles, which can result in significant differences between BET and particle size surface area measurements[147].

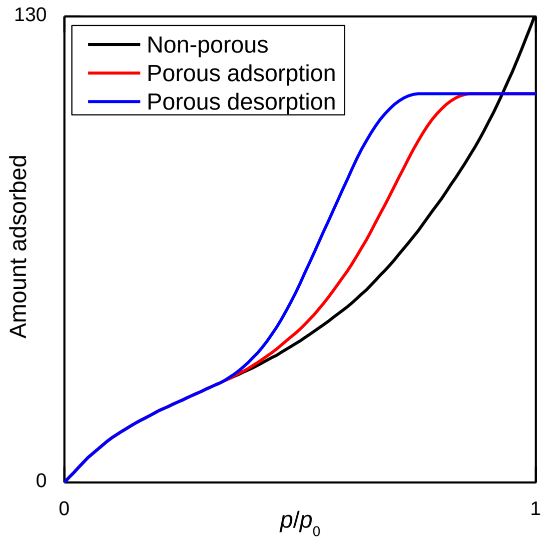

Figure 5.3. Example BET isotherms. Shown are example isotherms for non-porous and porous substances in terms of an arbitrary amount adsorbed vs. the fraction of saturation pressure[146]. The difference between the adsorption (red) and desorption (blue) isotherms for the porous material is due to the filling and emptying of pores. At low values of p/p_0 all three lines match.

In the Micromeritics TriStar 3000 used to measure the specific surface area, a known mass of dehydrated powder sample is placed in a flask of known volume and internal surface area. The flask is then evacuated and cooled to liquid nitrogen temperatures before a known mass of gaseous nitrogen is then added. The difference between the expected and observed nitrogen pressures allows calculation of the amount of gas adsorbed onto the sample and flask walls. Using Equation 5.4 toEquation 5.7 above, the sample surface area can be calculated and converted into a specific surface area by normalisation to a unit mass. For minerals that readily expand when absorbing water (e.g. montmorillonite[148]) it is assumed that the measured surface area and surface area available for immersion mode ice nucleation are the same.

The specific surface areas for the minerals used in Chapter 7 appear in Table 7.5 and range from 2.7 m^2 g^{-1} to 91.4 m^2 g^{-1}, with the clay minerals having specific surface areas above 25 m^2 g^{-1} and the granular minerals such as feldspar and quartz below 10 m^2 g^{-1}. Calculated using Equation 5.8 and a density of 2.6 g cm^{-3}, 25 m^2 g^{-1} corresponds to a mean particle diameter of 0.09 µm and 10 m^2 g^{-1} to 0.23 µm.

5.3.Summary

With the methods described here, the characterisation of the bulk powdered sample can be performed. The mineralogy of a sample can be determined for components contributing down to around 1 % of the mass using X-ray diffraction, and the samples mean surface area to mass ratio can be estimated using gas adsorption. This characterisation allows for the normalisation of nucleation coefficients to the mean particle surface area and gives confidence in apportioning nucleation events to the intended mineral in Chapter 7.

Chapter 6. Homogeneous nucleation: surface vs. volume nucleation

Knowledge of the homogeneous nucleation of ice within pure water droplets is important for a basic understanding of the formation of ice in highly supercooled liquid droplets. It is generally assumed that the probability of ice nucleation is dependent upon the volume of the droplet (e.g. refs [9,29,54,74,149]).

In 2002 and 2003, Tabazadeh *et al.*[44,150] and Djikaev *et al.*[83,151] hypothesised that homogeneous nucleation occurred due to the surface of the droplet. The evidence supporting this hypothesis was a reanalysis of experiments containing different sized droplets, in which nucleation normalised to the droplet surface area produced a better fit than to the droplet volume. This hypothesis sparked some debate (e.g. refs [46,69] and the online discussion about ref [152]). Work by Duft and Leisner[77] in 2004 comparing the freezing of single droplets of 38 µm and 98 µm was unable to find conclusive evidence for or against the presence of significant surface nucleation and suggested that it was not present in droplets larger than 8 µm diameter.

Recently Kuhn *et al.*[86] investigated nucleation in droplets <10 µm diameter using a cryogenic laminar flow tube. In three separate experiments using droplet distributions with mode diameters of 2, 3.4 and 5.8 µm, they found that droplet freezing was most accurately described using nucleation due to both the droplet surface and volume[86].

The new instrument developed in Chapter 3 is capable of observing droplets down to ~5 µm diameter, which in the region of the droplet sizes that surface nucleation has been suggested to be important[77,86]. This capability and the lack of certainty in the relevance of surface nucleation have motivated the further study of homogeneous ice nucleation. The following sections provide experimental results and derived nucleation rate coefficients, followed by a comparison with the literature and a discussion of the implications of this study for the atmosphere and future work.

6.1.Experimental results and nucleation rate coefficients

Homogeneous experiments were performed using the procedures outlined in Chapters 3 and 4 at cooling rates between 1 and 4 K min^{-1}. An example set of fraction frozen curves for a 1 K min^{-1} experiment is shown in Figure 6.1. As predicted by the theory (e.g. Equation

2.17), these curves show that the probability of freezing depends upon the size of the droplet: larger sizes freeze at higher temperatures. Fraction frozen curves are only of use for describing the freezing of a specific population of droplets. To predict the rate of freezing in a different droplet population it is necessary to calculate a nucleation rate coefficient.

Nucleation rate coefficients are calculated by normalisation of the probability of freezing to a property of the droplets, such as mean volume. To investigate if surface nucleation is active, the freezing data was normalised to the droplet volume (J_V, cm^{-3} s^{-1}) and surface area (J_S, cm^{-2} s^{-1}) separately for each of the droplet sizes in the experiment. The amount of scatter between the different droplet sizes in each normalisation then gives an implication of which normalisation is most accurate, and if the droplet volume or surface contributes to freezing. Example volume dependent nucleation rate coefficients for the 1 K min^{-1} data set, calculated using Equation 2.17, are shown in Figure 6.2. When this data is plotted on a log axis, the data approximately falls on to a straight line.

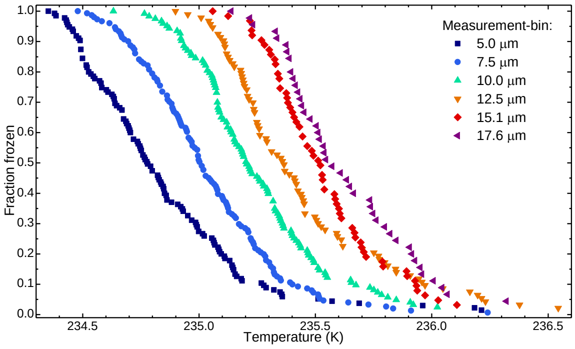

Figure 6.1. Fraction frozen curves for homogeneous experiments at two cooling rates. The centres of the droplet diameter measurement-bins are provided in the figure legend.

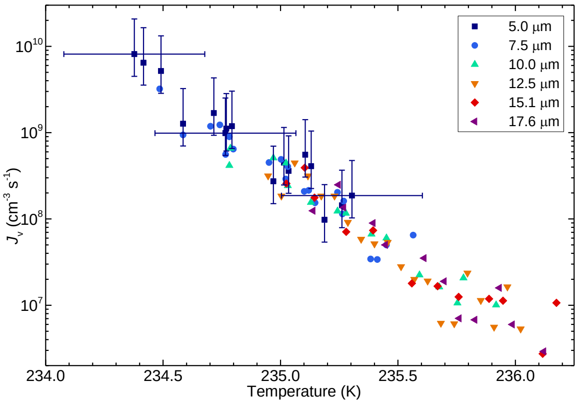

Figure 6.2. Nucleation rate coefficient for the 1 K min^{-1} homogeneous experiment. The coefficient (J_V) is calculated using Equation 2.17 using the measurement-bin interpolation corrected volumes (Table 4.3). The legend provides droplet diameter measurement-bin centres. Error bars are provided for the 5 μm droplet size; error bars provided for J_V display the maximum and minimum droplet volumes within the measurement-bin due to diameter measurement accuracy (± 1.25 μm) and are fractionally smaller for larger droplets. Sample temperature error bars (± 0.3 K) are also shown.

If nucleation due to the droplet surface is significant, normalisation to volume will cause differences between the nucleation rate coefficients calculated for each droplet size, especially at smaller sizes. As the individual data points in Figure 6.2 are scattered, linear regression fits are shown for each measurement-bin (Figure 6.3). This figure includes nucleation data normalised to the droplet surface area, s, calculated in a similar manner to the volume normalised nucleation coefficient (Equation 2.17):

$$\frac{n_\mathrm{i}}{n_\mathrm{L}} = 1 - \mathrm{e}^{-J_\mathrm{V}(T)V\Delta t} \qquad \textbf{Equation 2.17}$$

$$\frac{n_\mathrm{i}}{n_\mathrm{L}} = 1 - \mathrm{e}^{-J_\mathrm{s}(T)s\Delta t} \qquad \textbf{Equation 6.1}$$

where J_V and J_s are the volume and surface area normalised nucleation rate coefficients.

In some of the homogeneous experiments the number of droplets (~300) was insufficient to be able to calculate nucleation rate coefficients for individual droplet measurement-bins without significant amounts of scatter occurring (e.g. ‘exp 2’ in Figure 6.4). For these experiments no analysis was done beyond the calculation of the volume nucleation rate coefficient. The detailed analysis that follows concentrates upon a 1 K min^{-1} experiment with double the number of droplets (610).

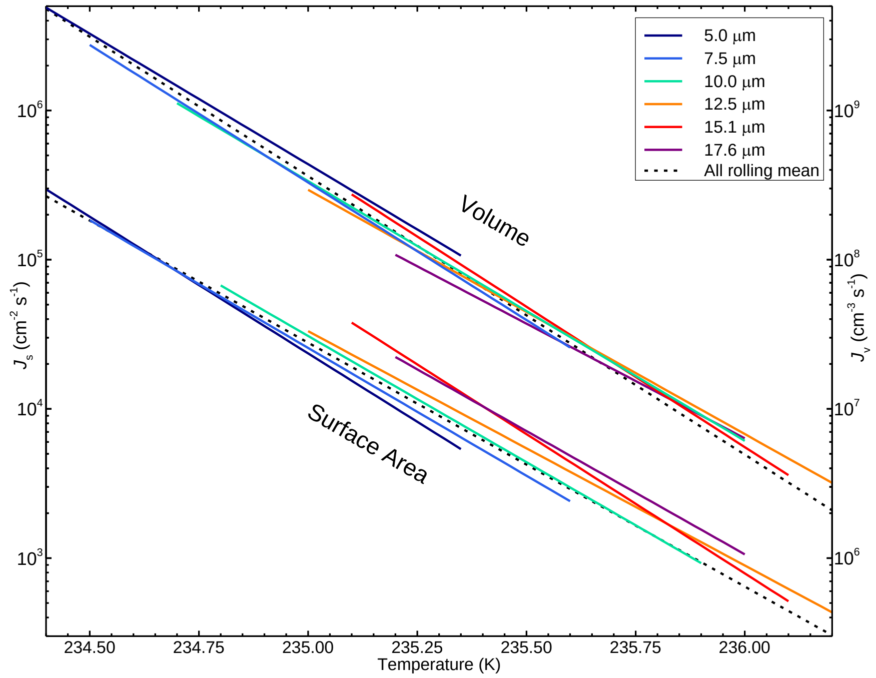

Figure 6.3. Nucleation rate coefficient fits to droplet volume and surface area broken down by droplet size for the 1 K min^{-1} experiment. The volume (surface area) normalised nucleation rate coefficient is shown on the right (left) axis. The fit to all six droplet sizes combined is also shown. For the volume rate coefficient most droplet sizes overlap, although the smallest (5 µm) is very slightly separated from the rest; for the surface area normalised coefficient the scatter is increased with a definite trend to higher values for larger droplets. Details of the individual fits are provided in Table 6.1.

When normalised to volume there is little discernible difference between each droplet size, though if one were critical it could be suggested that the data for the 5 µm measurement-bin is slightly separated (Figure 6.3). When normalised to surface area alone the scatter between the different droplet sizes increases, except for between the 5.0 and 7.5 µm measurement-bins. This implies that nucleation in droplets larger than 7.5 µm diameter is most accurately described using a volume based coefficient and in smaller droplet sizes nucleation due to the droplet surface may be occurring. However, in these small droplet sizes volume nucleation will still occur and nucleation by the volume and surface need to be considered simultaneously.

Param.	a_v	b_v	a_s	b_s	D_{tot}	R^2
All	-4.3714	1047.00	-3.7642	894.82	12.4/16.7	0.90/0.87
5.0 µm	-4.0281	966.52	-4.2193	1001.59	14.8/34.9	0.88/0.73
7.5 µm	-4.2446	1017.10	-3.9428	936.67	13.1/23.6	0.90/0.82
10.0 µm	-4.0075	961.38	-3.8939	925.36	12.3/17.3	0.91/0.87
12.6 µm	-3.7706	905.61	-3.6166	860.31	14.5/15.2	0.89/0.88
15.1 µm	-4.3338	1038.28	-4.2993	1021.29	11.9/36.2	0.91/0.72
17.6 µm	-3.5413	851.35	-3.8057	905.11	29.7/26.7	0.79/0.79

Table 6.1. Parameterisations for the surface and volume nucleation fits shown in Figure 6.3. D_{tot} (calculated using Equation 6.4) and R^2 values provided are for volume before the slash and surface afterwards.

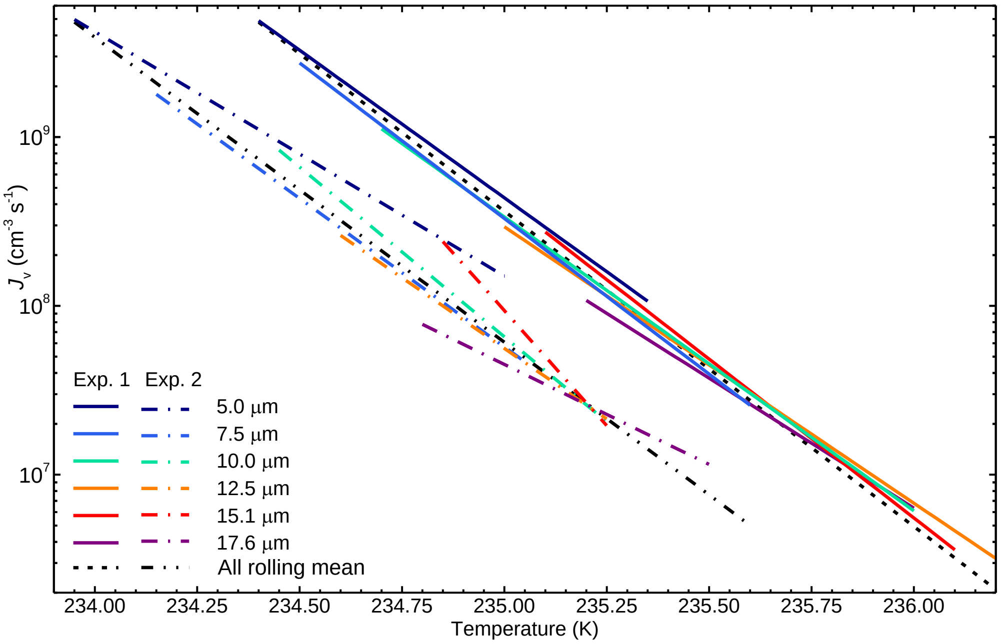

Figure 6.4. A comparison of volume normalised nucleation rate coefficients for two experiments. Both experiments were at 1 K min^{-1}, the first containing 610 droplets and the second 302 droplets. Note the large scatter and variation in slope of the fitted nucleation rate coefficients for the second experiment.

6.1.1. Combined surface and volume nucleation

To investigate the surface-volume nucleation relationship further, nucleation from the surface and the volume are combined by inserting Equation 2.20 into Equation 2.21[44,77,86]:

$$\frac{n_\mathrm{i}}{n_\mathrm{L}} = 1 - \mathrm{e}^{-\Delta t(J_\mathrm{V}(T)V + J_\mathrm{s}(T)s)}$$ **Equation 6.2**

which can then be solved iteratively to estimate J_V and J_s. V and s are the droplet volume and surface area respectively, using the interpolated values as provided in Table 4.3. The iteration uses the non-normalised nucleation rate, J', for each measurement-bin:

$$J' = -\frac{\ln\left(1 - \frac{n_\mathrm{i}}{n_\mathrm{L}}\right)}{\Delta t}$$ **Equation 6.3**

Iterative fitting was then performed by minimising the sum of the squares of the weighted difference in each of the x measurement-bins:

$$D_\mathrm{tot} = \sum_{x,y}\left(\frac{n_\mathrm{i}}{n_\mathrm{i}+1}\left(\ln J'_y - \ln J_{\mathrm{tot},y}\right)^2\right)$$ **Equation 6.4**

where D_tot is the minimised value, summed over each measurement-bin x, which contain y data points in which n_i droplets freeze and $J_{\mathrm{tot},y}$ is the value of $J_V V + J_\mathrm{s} s$ calculated for each y from the fitted values of J_V and J_s. R^2 values can also be calculated for each parameterisation for comparison.

A weighting factor, $n_\mathrm{i}/(n_\mathrm{i} + 1)$, is present in Equation 6.4 to represent the certainty of the value of each experimental data point. The nucleation rate is based upon the probability of freezing, calculated from the number of droplets which have frozen during a time step (Equation 6.3) via the Poisson distribution (Equation 2.16). However, as the value of J' is calculated from a probability, there are a range of values of J' which could result in the same number of freezing events[66]. The width of this range is inversely proportional to the number of events, meaning that values calculated from a small number of droplets can be more affected by experimental variability than higher numbers of events. For example, adding a freezing event to one analysis time bin, such as from a neighbouring time bin or measurement-bin, could cause a large change in the resulting value - adding an event to a time bin containing one event would approximately double J', whereas adding a droplet to a bin with ten already present would result in a much smaller change. The weighting then gives a greater importance to the data points with greater certainty – a point with one event is given a 50 % weighting (1/(1+1)), whereas points with 10 events are weighted at ~91 % (10/(10+1)).

The results of minimisations using Equation 6.4 are shown in Table 6.2. Minimisations have been performed using surface only, volume only and surface and volume nucleation combined (S1, V1 and C1 in Table 6.2), and are shown in Figure 6.5. The D_{tot} values for each of these fits are similar, and the R^2 values provided to give a standardised measure of the goodness of fit suggest that all three are of similar quality. This can be seen visually by the similarity of the fits in Figure 6.5: in comparison to the C1 fit, V1 gives slightly lower value for small droplet sizes and vice versa for large droplets. The surface only fit (S1) also gives a reasonable match to the data, but is disregarded as nucleation by the droplet surface alone has been previously disproved using larger droplets[28,69,76-78]. However, with the similar quality of the V1 and C1 fits to the data presented here it is not possible to categorically conclude that surface nucleation is or is not significant. If surface nucleation is inactive, the V1 fit gives an a_{V} value of ~-4.2, and if surface nucleation is active the C1 fit gives a_{V} is ~-3.7 and a_{S} is ~-4.9.

The best minimisation (smallest D_{tot}) to the experimental data is C1, which utilises both surface and volume nucleation and is displayed in Figure 6.6. The parameterisation from this minimisation does a good job of replicating the nucleation rates calculated for both small and large droplets. It is consistent with Duft and Leisner's[77] statement that at 237.1 K surface nucleation and volume nucleation should be equivalent for droplets no bigger than 8 µm diameter. Figure 6.6 suggests that an equivalent diameter of 7.5 µm occurs at around ~234.5 K, though it must be noted that these droplets are not spherical.

Param.	Constraint	a_{V}	b_{V}	a_{S}	b_{S}	D_{tot}	R^2
S1	None	n/a	n/a	-3.5270	839.15	14.62	0.8822
S2	a_{S}: Kuhn *et al.*[86]	n/a	n/a	-3.1853	758.75	16.16	0.8660
V1	None	-4.1716	1000.09	n/a	n/a	11.40	0.9098
V2	a_{V}: Stan *et al.*[76]	-4.4746	1071.36	n/a	n/a	12.61	0.9013
V3	a_{V}: Riechers *et al.*[28]	-3.574	859.47	n/a	n/a	16.11	0.8693
C1	None	-3.7000	888.78	-4.8956	1159.63	10.65	0.9150
C2	a_{V}: Stan *et al.*[76]	-4.4746	1071.36	-4.4779‡	1050.04‡	12.61	0.9013
C3	a_{V}: Riechers *et al.*[28]	-3.574	859.07	-4.8687	1153.44	10.69	0.9145
C4	None, 5-10 µm	-3.9552	948.50	-4.2532	1009.03	12.04	0.9072
C5	None, 10-17.6 µm	-3.5141	845.00	-6.7194	1588.84	20.33	0.8423
Kuhn	Kuhn *et al.*[86]	-2.5961	628.49	-3.1853	758.58	24.39	0.7848

Table 6.2. Summary of homogeneous ice nucleation parameterisations. Parameterisations are labelled as surface (S1, S2), volume (V1 – V3) and surface/volume combined (C1 – C5). See text for a description of the fitting process and constraints. C4 and C5 are unconstrained fits similar to C1, but with the minimisation stage only performed using a portion of the dataset: C4 drop sizes 5 – 10 µm inclusive, C5 10 – 17.6 µm inclusive. R^2 values have been provided for comparison. The parameterisation by Kuhn *et al.*[86] (labelled 'Kuhn') is provided for comparison, along with the value of D_{tot} resulting from Equation 6.4. ‡: This surface nucleation parameter produces values of J_{S} too small for surface nucleation to occur in any of the observed droplet sizes.

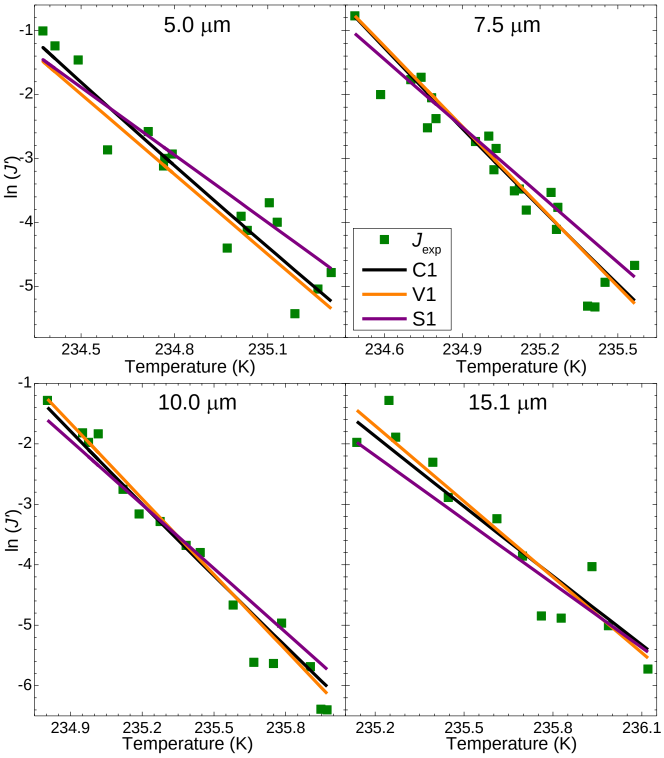

Figure 6.5. A comparison between the nucleation rate coefficient parameterisations. J' (y-axis, Equation 6.3) is the non-normalised nucleation rate, with the experimental data J_{exp}. The parameterisations shown are the C1, V1 and S1 fits from Table 6.2. Note the minor differences between the C1 and V1 fits, as suggested by the similar goodness of fit for each. Each panel shows a measurement-bin, with labels providing bin centres ±1.25 µm.

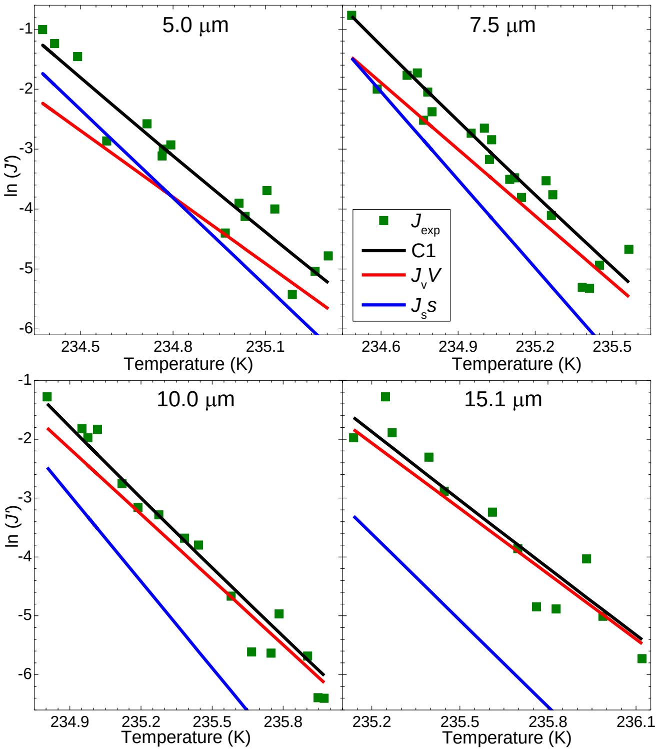

Figure 6.6. Surface and volume nucleation rates for the C1 parameterisation, as fitted using Equation 6.4. Similar to Figure 6.5, C1 and $J_V V$ and $J_S s$ from C1 are now shown. ln(J_V) = -3.7000 T + 888.78, ln(J_S) = -4.8956 T + 1159.63 (Table 6.2).

As mentioned above, evidence against surface only ice nucleation has been presented in the recent literature using droplets significantly larger (>50 µm diameter) than here[28,69,76-78]. Data from these publications could be used to constrain the volume nucleation rate in minimisations. However, of these publications some either provided data at a single temperature[77,78] or did not correct for changes in the droplet size distribution during the experiment (ref [69], Section 4.3.1). The datasets of Riechers *et al.*[28] and Stan *et al.*[76] provide the temperature dependence of J_V and do not have these size distribution issues due to modelled droplet size distribution and a very narrow reported size distribution respectively. Fits have been produced using these data sets to constrain the temperature dependence of the volume rate coefficient (Riechers *et al.*[28]:V3, C3; Stan *et al.*[76]: V2, C2). The V2 minimisation (Stan *et al.*[76], no surface nucleation) produced D_{tot} and R^2 values similar to V1. Likewise, the C3 fit to surface and volume nucleation combined using the Riechers *et al.*[28] volume nucleation temperature dependence resulted in a similar D_{tot} and R^2 to C1. For comparison with these fits, a minimisation using the Kuhn *et al.*[86] surface nucleation slope (S2) has been provided for comparison.

6.2.Discussion

6.2.1. Surface-volume equivalent radius

The atmospheric relevance of surface nucleation depends on not just the absolute surface nucleation rate, but also the surface to volume ratio of the droplets in question. This ratio dependence can be taken into account by determining the radius at which nucleation due to the surface and volume are of equivalent (i.e. $J_V V = J_S S$, see Section 2.2.3.1.1 and refs [44,77,86]), r_{eq}:

$$r_{\mathrm{eq}}(T) = \frac{3J_{\mathrm{S}}(T)}{J_{\mathrm{V}}(T)} \qquad \textbf{Equation 2.22}$$

As the ratio of J_V and J_S is not constant with temperature, r_{eq} is temperature dependent. The resultant values of r_{eq} are compared with that of Kuhn *et al.*[86] in Figure 6.7. For droplets smaller than this radius surface nucleation will be more important and vice versa for larger droplets. Note that the values of r_{eq} displayed in Figure 6.7 are slightly different to those implied by Figure 6.6 as the experimental droplets are not perfectly spherical and thus have a different surface to volume ratio.

The calculated equivalent radii for the C1 parameterisation imply that for droplets larger than ~5 µm diameter surface nucleation is not dominant. For larger droplets surface nucleation will become increasingly important. However, Figure 6.7 does not account for the temperature at which droplets of those radii typically freeze, which increases rapidly with size (Figure 6.1). Therefore, expected fraction frozen curves for several droplet sizes including and excluding surface nucleation have been calculated (Figure 6.8). For droplets radius ≥5 μm surface nucleation has insignificant impact upon the expected fraction frozen, but in smaller droplets the impact is significant.

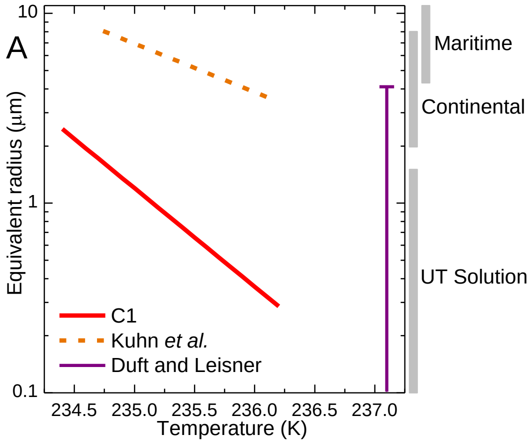

Figure 6.7. Temperature dependent equivalent radius of surface vs. volume nucleation. Calculated using Equation 2.22 for the parameterisations C1 from Table 6.2 compared with r_{eq} from the parameterisation provided by Kuhn *et al.*[86]. Both parameterisations are consistent with the upper limit of r_{eq} = 4 μm at 237.1 K derived by Duft and Leisner[77]. The grey bars to the right provide typical droplet mode radii for maritime and continental clouds[153,154] and typical upper troposphere (UT) solution droplets[155].

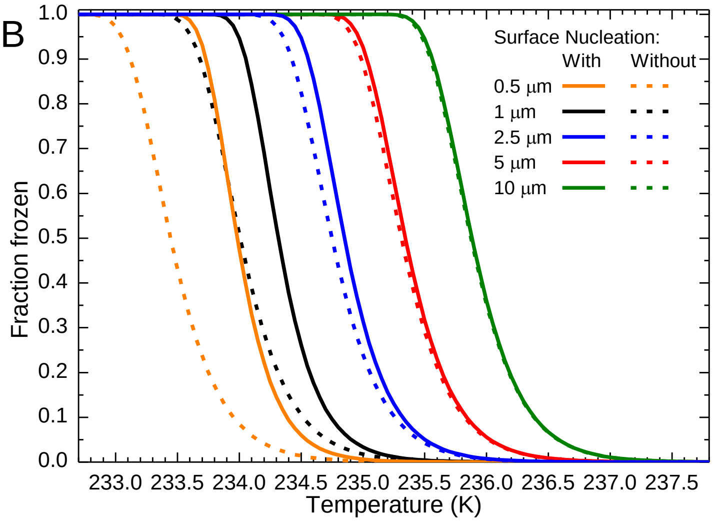

Figure 6.8. Expected fraction frozen for different size droplets with and without surface nucleation. The surface and volume based nucleation rates recommended (C1 parameterisation) were used with a cooling rate of 1 K min^{-1}, assuming spherical droplets of the radius given in the legend. The presence of surface nucleation has no impact on large droplets but is important at small sizes. The nucleation rate coefficients have been extrapolated outside of the experimental temperature range (234.4 – 236.2 K).

If surface nucleation is disregarded for droplets of 0.5 μm radius this reduces the temperature at which 50 % of the droplets are predicted to freeze by ~0.5 K. This is greater than the change in freezing temperature caused by doubling the droplet radius. This result implies that for the majority of lower tropospheric clouds surface nucleation can be neglected (e.g. Figure 6.7, refs [153,154]). In upper tropospheric solution droplets, which can be much smaller[155], surface nucleation may have a major impact – for a 1 μm diameter droplet at 234 K, surface nucleation contributes ~90 % of the overall nucleation rate. However, as ice nucleation in solution droplets is affected by the solute[156], the relative importance of surface and volume nucleation may be different in these droplets.

In comparison to r_{eq} calculated by Kuhn *et al.*[86], the r_{eq} presented here is significantly smaller. However, the droplet sizes in the experiments[81] analysed by Kuhn *et al.*[86] are all smaller than ~6 μm diameter. The data presented here (e.g. Figure 6.6) suggests that surface nucleation is active in droplets of this size. It is possible the lack of larger droplets in the experimental data allows too much freedom for the volume nucleation coefficient within the fitting process. To illustrate the effect of the absence of large droplets constraining the volume coefficient in the fitting process, two additional minimisations were performed.

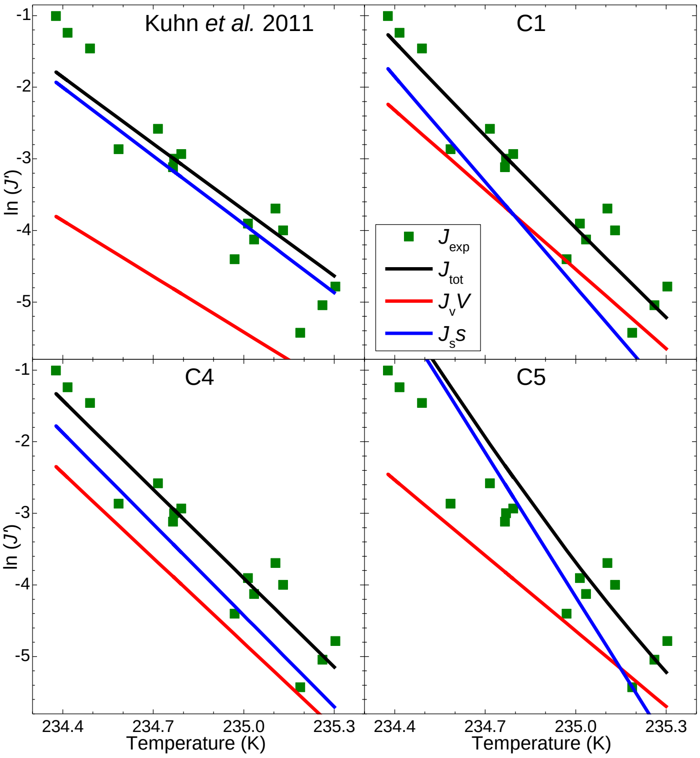

Figure 6.9. A comparison of the C1, C4 and C5 parameterisations with Kuhn *et al.*[86]. Shown are results of the parameterisations for the 5 μm experimental droplet size, with parameters based on all droplet sizes (C1), small droplets (≤10 μm, Kuhn *et al.*[86] and C4) and large droplets (≥10 μm, C5). The Kuhn *et al.*[86] and C4 parameterisations allow greater flexibility in volume nucleation, whereas C5 allows greater flexibility in surface nucleation.

The minimisation process (Equation 6.4) was then limited to droplets in specific measurement-bins (Table 6.2): C4 used droplets 5 – 10 µm inclusive (399 drops total) and C5 10 – 17.6 µm inclusive (312 drops). The values of D_{tot} and R^2 presented in Table 6.2 are calculated using all six measurement-bins. This results in different balance between nucleation due to the droplet surface and volume in each fit. The lack of larger droplets removes the constraint to the volume nucleation rate coefficient in the C4 fit and vice versa for C5. This allows greater flexibility in the volume component (surface in C5) without having a significant impact upon the value of the minimisation (Figure 6.9). This suggests that experiments that lack droplets larger than ~10 µm, such as those done by Kuhn *et al.*[86], may result in parameterisations that significantly increase the relative importance of surface nucleation.

To prevent such a bias towards surface or volume nucleation, the ideal experimental dataset for parameterising these nucleation coefficients would contain both droplets significantly larger and significantly smaller than 10 µm. Larger droplets are required to accurately parameterise volume nucleation, and smaller to parameterise surface nucleation. Observing and accurately measuring droplets smaller than 5 µm diameter in the current experimental configuration is not possible.

6.2.2. Comparison of rate coefficients with the literature

These new data can be compared with nucleation rate coefficients reported in the literature. The data for all the homogenous experiments are shown, including parameters calculated for volume nucleation (V1 and C1), and fall into the colder half of the reported values of J_V (Figure 6.10). There is good agreement between the fitted parameters (C1 and V1) and some recent works[29,69,73,76,81,86], and especially with Riechers *et al.*[28] and the higher temperature data of Lüönd *et al.*[42] and Hoyle *et al.*[80].

In comparison to volume nucleation, there are very few publications providing surface area normalised nucleation rate coefficients (Figure 6.11). The surface nucleation parameters presented here (C1, S1) are both lower than the data produced by Tabazadeh *et al.*[44] and the limit estimated by Duft and Leisner[77]. As Tabazadeh *et al.*[44] parameterised nucleation using the droplet surface area only, this data also represents an upper limit to the surface nucleation rate coefficient. The surface only parameterisation (S1) is very close to the parameterisation of Kuhn *et al.*[86], and the surface component of the C1 parameterisation (surface and volume combined) is around an order of magnitude lower at high temperatures.

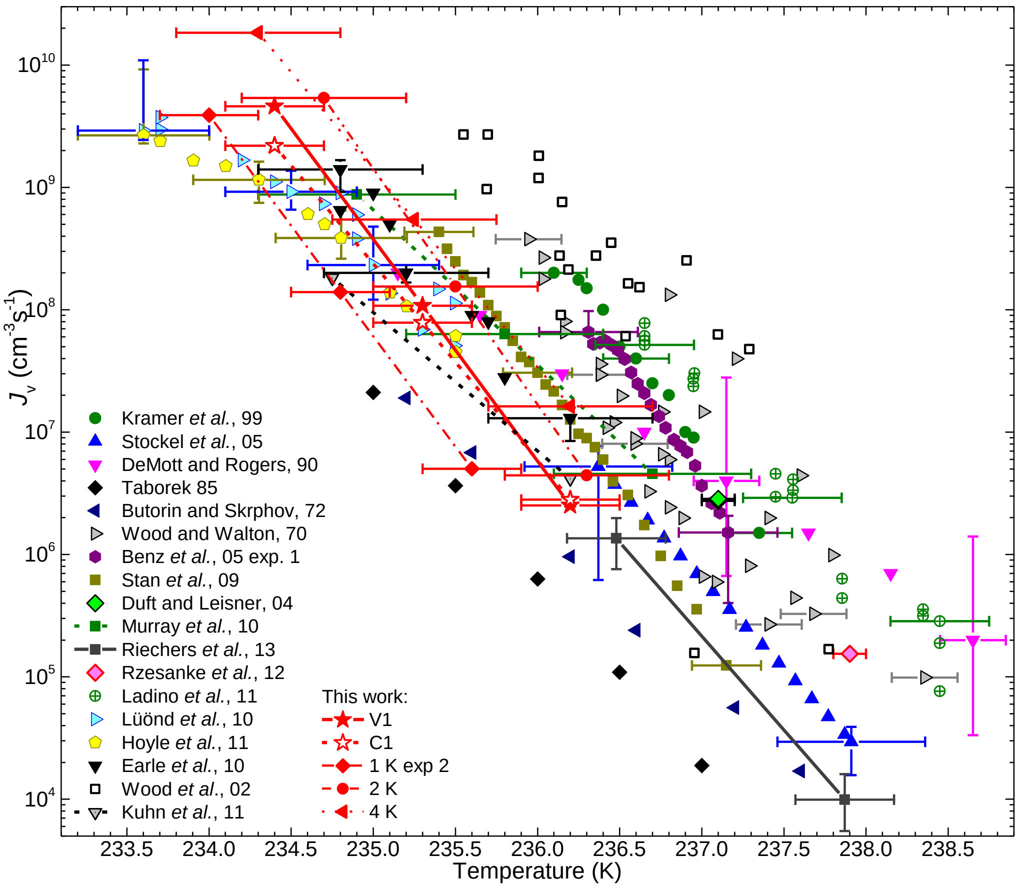

Figure 6.10. Calculated volume dependent homogeneous nucleation rate coefficient compared to literature data. Updated from Figure 2.4, with the volume components of the V1 and C1 parameterisations (Table 6.2) and volume nucleation rates from three other experiments (listed by cooling rate), with error bars showing the experimental temperature uncertainty (note the larger uncertainty for the 2 and 4 K min^{-1} experiments). The volume component of the surface and volume combined nucleation parameterisation of Kuhn *et al.*[86] is also shown. Sample error bars for the literature data[28,29,42,69-82] are provided.

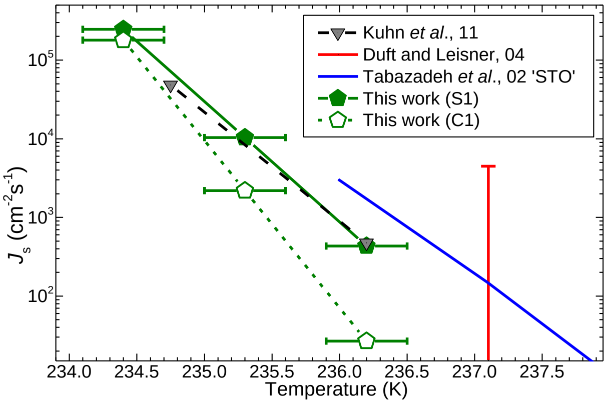

Figure 6.11. A comparison of the minimised surface nucleation rate coefficient with literature data. The line for Kuhn *et al.*[86] corresponds to the surface component of their surface and volume combined nucleation parameterisation, and the line from Duft and Leisner[77] is an upper limit to the surface nucleation rate coefficient based upon their data. Tabazadeh *et al.*[44] reanalysed results produced by Taborek[72] by assuming all nucleation was caused by the droplet surface and hence this data represents an upper limit to the surface nucleation rate coefficient in that dataset.

The close match between the Kuhn *et al*. parameter and S1 was not expected, as surface only nucleation is inconsistent with observations of freezing in higher droplet sizes. As discussed in the previous section, the explanation for this is the lack of large droplets in the Kuhn *et al*.[86]/Earle *et al*.[81] experiments (0.5 – 5 µm radius) – the absence of larger droplets allows more freedom to the value of volume nucleation during the fitting process.

6.2.3. Potential explanations for surface nucleation

If, as suggested by Kay *et al*.[46], surface nucleation is assumed to occur in a near-surface rather than directly upon the surface interface, it is appropriate to calculate an ice-liquid surface energy for the volume within this layer. At the surface, there is a transition zone between the liquid and exterior phases (i.e. the bath gas or oil). The near-surface layer is then assumed to be a layer including this zone and thick enough to contain a critical ice cluster (e.g. a few nm at <240 K according to Equation 2.6). In this zone the concentration of water molecules, and hence density of water, rapidly changes from liquid to vapour/solution values[84]. While the surface transition zone is very thin, on the order of a few Angstroms thick, a critical ice cluster is also very small (radius ~1.3 nm at 235 K calculated using Equation 2.6). This may be sufficient to cause significant differences between the near-surface layer and the bulk volume. For example, based upon the density profile in Figure 6.12 (density changes from zero to bulk within 0.5 nm), the mean density of a spherical ice cluster 1.3 nm radius would be reduced by ~8 %.

It has been suggested in molecular dynamics simulations that this low density region reduces the work done by the ice germ to expand the liquid phase into an ice-like phase[84]. The same simulations also showed that the outer-most layer of water molecules remained disordered and did not form part of the ice cluster, consistent with the suggestion of Kay *et al*.[46]. Conversely, Sun *et al*.[85] have observed a change in the oxygen-hydrogen bond length for water molecules with less than four neighbours (i.e. the layer of molecule directly upon the surface). They suggest that as well as reducing the density of this layer, it also gives the layer an ‘ice-like’ structure that is thermally more stable[85]. It has also been suggested that features are present in the charge profile near the surface (Figure 6.12, ref [84]). While it has been suggested that a bulk charge on a droplet has no effect on the ice nucleation rate[78], charges at the surface of a droplet may be important[157].The minimising process detailed above uses the droplet surface area rather than the volume of this surface layer. This is suitable for defining the temperature dependence of nucleation within this layer but is not suitable for describing the non-temperature dependent component. As pointed out by Kay *et al.*[46], in such a scenario the volume of the surface layer is on the order of 0.1 % of the total droplet volume. Therefore, for the probability of freezing due to the surface layer to be equal to that from the bulk droplet volume the surface layer nucleation rate coefficient must be in the region of a thousand times larger than that of the volume. Mathematically this would require either a shallower slope of J, which was not observed, or an increase in the pre-exponential in Equation 2.14 (Equations 2.10 - 2.13). Within the different descriptions of the pre-exponential a reduction to the density of the liquid, equivalent to an increase in the molecular volume, results in a smaller pre-exponential. This implies that the representations of the pre-exponential for the droplet volume are inappropriate for describing nucleation within the droplet surface layer.

6.3. Summary and conclusions

The analysis of a homogeneous experiment has been performed at a cooling rate of 1 K min^{-1} with droplets of between 3.75 and 18.75 µm diameter. This slow cooling rate has been used to minimise any systematic temperature uncertainty as one of the goals of this experimental work has been to reduce the uncertainty in the homogeneous nucleation rate coefficient, rather than to investigate the time dependence of nucleation. When considering the whole range of droplet sizes, it is possible to describe ice nucleation using a solely volume dependent parameterisation. However, there is some scatter between different size droplets.

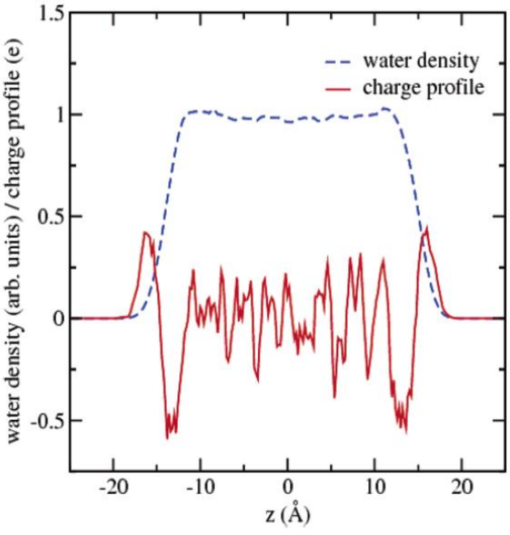

Figure 6.12. Charge distribution and density profile through a small mass of liquid water. From a molecular dynamics simulation of a slab of water molecules 30 Å across, showing the density-transition surface layer and surface features in the charge profile. From Vrbka and Jungwirth[84].

It has been suggested in the literature that the surface of a pure water droplet may cause the nucleation of ice[44,83,86,150,151]. Water molecules in the layer near the surface of the droplet have different properties to those in the bulk droplet volume[84,85] and will therefore have a different ice nucleation rate coefficient. However, this rate coefficient is not necessarily high enough for the surface layer to be a significant source of nucleation events[46].

Calculating nucleation rate coefficients by normalisation to the droplet surface area increases the scatter between droplets 10 µm diameter and larger, but improves agreement at smaller sizes. This implies that both the surface and volume of the droplets are participating in ice nucleation. Fitting to a two component (surface and volume) nucleation scheme using a minimising process has produced a parameterisation with a smaller minimisation and greater R^2 value than the volume only fit.

From the data and fits presented here it is not possible to clearly conclude that surface nucleation is occurring at rates sufficiently high to compete with volume nucleation. This is because both the volume only and combined minimisations have produced rate coefficients that are consistent with the literature data, and both have a similar goodness of fit.

When the nucleation coefficient is normalised to the droplet surface area, there is a good agreement between the smallest droplet sizes. Based upon this and the results of the fitting process (i.e. the smallest D_{tot}), the recommended parameterisation for homogeneous ice nucleation in pure water droplets is the C1 minimisation. This combines nucleation by the droplet volume and surface and is valid at 234.4 – 236.2 K:

$$\frac{n_{\mathrm{i}}}{n_{\mathrm{L}}} = 1 - \mathrm{e}^{-\Delta t (J_{\mathrm{V}}(T)V + J_{\mathrm{S}}(T)s)} \qquad \textbf{Equation 6.2}$$

$$J_{\mathrm{V}} = \mathrm{e}^{-3.7000T + 888.78} \qquad \textbf{Equation 6.5}$$

$$J_{\mathrm{s}} = \mathrm{e}^{-4.8956T + 1159.63} \qquad \textbf{Equation 6.6}$$

The volume component of the parameterisation, Equation 6.6, agrees very well with a number of literature datasets, especially those of Riechers *et al.*[28], Kuhn *et al.*[86], Hoyle *et al.*[80] and Lüönd *et al.*[42] (Figure 6.5). At above ~235 K, the surface nucleation rate is lower than that published by Kuhn *et al.*[86]. This is explained by the lack of droplets larger than 10 µm in the Kuhn *et al.*[86] experiments, which allows too much flexibility in the assignment of nucleation events between the surface and volume nucleation rates.

In the majority of clouds in the troposphere, especially maritime clouds which tend to contain less droplets than continental, droplet sizes tend to be too large for nucleation by the droplet surface to be significant[153,154]. In many continental clouds droplet radii are too large for surface nucleation to be important, although cases with median droplet radii below

2 μm are seen[153,154] in which surface nucleation may be important. In comparison, the solution droplets present in the upper troposphere are much smaller[155], and fall in the range of droplet radii where surface nucleation is significant. However, the effect of high concentrations of solute molecules upon surface nucleation is not clear and may not have the same concentration dependence as volume nucleation[156].

Chapter 7. The ice nucleating behaviour of atmospherically relevant mineral dusts

7.1. Introduction

Atmospheric mineral dusts are inorganic particles of rock and soil that have been lifted into the atmosphere, predominantly from arid regions such as the Sahara[158,159]. Mineral dusts from these regions are considered an important source of ice nuclei in mixed-phase clouds due to their nucleation efficiency[37,47,109] and abundance in the atmosphere[158]. The importance of mineral dust as an ice nuclei is also supported by its enhanced concentration within atmospheric ice crystals relative to the background aerosol[33-35,123,160].

Previous studies have investigated the ice nucleating behaviour of dusts sampled from arid source regions or dusts selected as proxies for natural dust (see Murray *et al.*[30] and references therein; Hoose and Möhler[31] and references therein). Studies of ice nucleation by individual minerals of varying purity immersed in water have focused on the clay minerals[30,31,38-42,114]. However, minerals are rarely available in a pure state and quantification of secondary minerals associated with a particular sample is often neglected. This characterisation is necessary because a minor component may dominate ice nucleation[40,161], and the individual components of mineral dust responsible for ice nucleation are poorly constrained.

7.1.1. Chapter contributions

Large parts of this chapter repeat or closely resemble material produced by the author for two publications. The majority of the discussion of the different mineral types in section 7.2.2 appeared in Section 6 of Murray *et al.* 2012[30] and was the work of this author, with proofing by the other authors of that article. Some parts of section 7.2.2 did not appear in Murray *et al.*[30]: additional discussion in 7.2.2.1 referring to mixed layer clays, the difficulties in acquiring pure illite samples and the description of muscovite mica, along with further discussion in section 7.2.2.2 regarding acid weathering of feldspar. Figure 7.7 to Figure 7.10 and Figure 7.12 were published in Murray *et al.*[30].

The majority of the rest of this chapter is based upon Atkinson *et al.*[107]. As this publication was in letter format the text was necessarily brief and some expansion and clarification has been added when producing this chapter. The main discussion and overall conclusions of this chapter and Atkinson *et al*.[107] are equivalent and figures from this publication appear within this chapter.

The main published figures appear here as Figure 7.14, Figure 7.16A, Figure 7.17, Figure 7.19C+D and Figure 7.21. The published supporting figures and tables are included here as Figure 7.5, Figure 7.16B, Figure 7.19A+B, Figure 7.22, and Table 7.1, Table 7.4 and Table 7.6. A number of authors contributed to this paper. The experiments using microlitre sized droplets (Figure 7.17) were performed and analysed by Mr T.F. Whale; Drs K.J Baustian and D. O'Sullivan assisted with some of the laboratory work. Dr B.J. Murray helped devise the whole study and Dr M.T. Woodhouse helped to devise and performed the modelling work. The maps of model output were created by Dr M.T. Woodhouse and reformatted by this author; all other figures were created by this author. Mineralogical identification was performed by Dr. T.L. Malkin. All the authors assisted with the proofing of the manuscript.

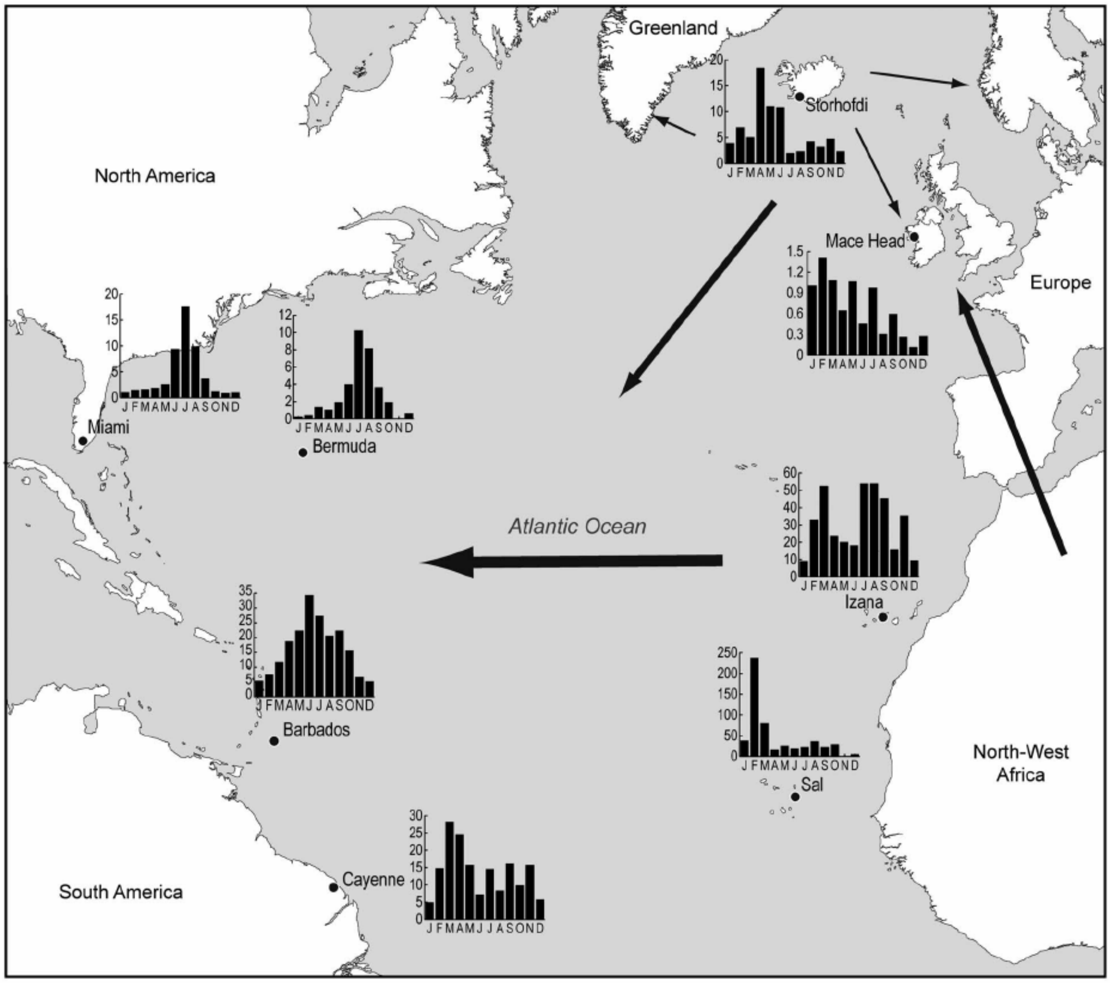

Figure 7.1. Mean monthly dust concentrations at eight sites around the north Atlantic, in µg m^{-3}. The arrows, which are not to scale, indicate the magnitude and principle direction of dust transport. Taken from Prospero *et al*.[162].

7.2. Atmospheric mineral dust

As the rocks of the Earth’s surface are broken down by the effects of physical and chemical weathering, small particles are formed[163]. In many locations, moisture and vegetation bind this dust together as soil. However, in arid and semi-arid regions, such as deserts and scrub land, these particles remain loose and mobile and can be lifted into the atmosphere by surface winds[164,165]. They are then distributed around the globe by atmospheric circulation patterns[166]. The concentration of airborne dust at any location therefore depends upon the local winds and distance from source.

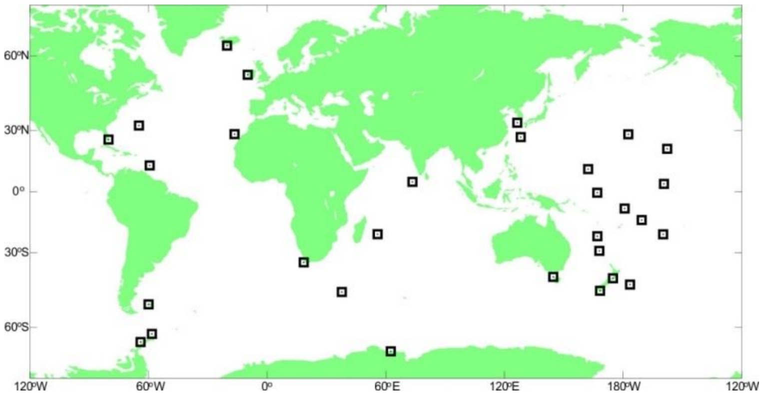

Figure 7.2. Locations of surface dust concentration measurement sites operated by the University of Miami during the 1980’s and 90’s. See for example, the Global Aerosol Climatology Project administered by NASA[167].

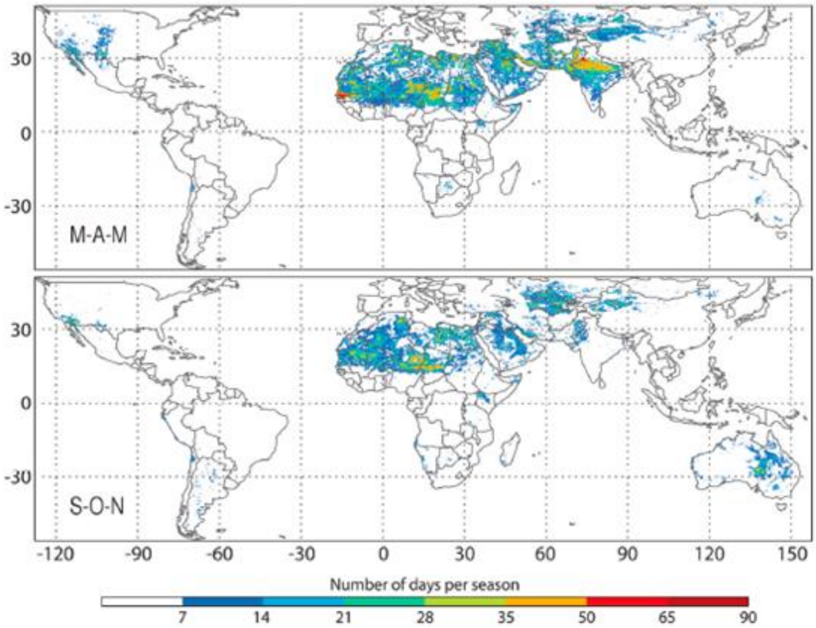

Figure 7.3. Global distribution of the seasonal mean number of days where the dust aerosol optical depth was greater than 0.2 during 2003-2009. Spring (Mar-Apr-May) and autumn (Sep-Oct-Nov) are shown. The dust aerosol optical depth, a proxy for the actual dust concentration, is retrieved from the Deep Blue data produced by the MODIS satellite, 0.2 is a threshold value used to classify a day as dusty. Taken from Ginoux *et al.*[158].

In the last two decades of the previous century, surface concentrations of atmospheric dust were recorded with standardised equipment at a number of sites around the globe (Figure 7.2) by a group from the University of Miami[167]. This observation network was globally dispersed and provided annual average dust observations, which were used by Woodward[168] and appear in section 7.4. The monitoring stations of this network were concentrated around the edges of the oceans (Figure 7.1), and the expensive and time consuming methodology for dust measurements prevented their extended use. For example, the observations taken at Iceland (the northern-most location in Figure 7.2) were produced using filters exposed for ~2 days each and then shipped back to Miami for laboratory analysis[162].

In absence of a wide network of surface and lower atmosphere monitoring sites satellite observations are used, but the ability of early satellite retrievals of atmospheric dust was limited. For example, early instruments used the overall aerosol concentration to estimate dust aerosol over desert regions, but such an estimation is inappropriate in locations where other aerosol is present and in some cases produced measurements limited to specific times of day[169]. With the 2004 launch of the first of the Meteosat Second Generation satellites carrying the SEVIRI instrument, frequent (15 minutes) high resolution dust measurements are available[169]. However, contemporary satellite instruments do not measure an absolute dust concentration but rather the dust aerosol optical depth[158]. This is an estimate of the amount of light which is absorbed or scattered as it passes through the atmosphere and is affected by variables such as particle number, size, shape optical properties and altitude[170]. Figure 7.3 shows an example analysis using such data, where the number of days per season where the dust aerosol optical depth exceeds a level is quantified[158].

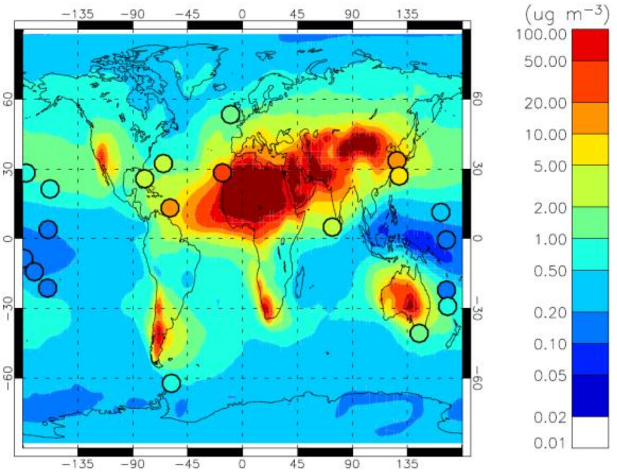

Figure 7.4. Annual mean modelled surface dust mass concentration, in µg m^{-3}. Annual mean surface dust mass concentration measurements are provided (circles). From Mann *et al.*[171].

As high resolution absolute dust concentrations are not currently available, especially at altitude, numerical models are used to estimate concentrations. Modelling is typically done using a chemical transport model which includes aerosol, such as the TOMCAT chemical transport model combined with the GLOMAP aerosol module[171]. Briefly, these models predict the atmospheric concentration of trace gases and aerosol by simulating sources (the surface and upper atmosphere), sinks (deposition to the surface), and the conversion of mass between species due to chemical and physical processes. These gases and aerosol are then transported around the atmosphere using a historical meteorology case, providing accurate values of parameters such as wind and precipitation which are used for transport and deposition.

Reference	Location	IL/MI	KA	MO	CH	QU	KF	NCF	CA	OT	Tsp.
Glaccum[172]	Cape Verde	53.7	6.6	0.0	4.3	19.6	2.2	5.4	8.2	0.0	Y
Glaccum[172]	Barbados	64.3	8.3	0.0	4.1	13.8	1.5	4.1	3.9	0.0	Y
Glaccum[172]	Miami	62.3	7.1	0.0	3.9	14.2	1.1	4.5	6.9	0.0	Y
Prospero[173]	French Guiana	62.0	10.0	0.0	5.0	8.0	2.0	5.0	1.0	7.0	Y
Prospero[173]	French Guiana	26.0	5.0	0.0	4.0	21.0	1.0	8.0	5.0	30.0	N
Blank[174]*	NW. Pacific	39.5	15.5	1.1	2.7	10.5	-*	11.2	-*	19.5	Y
Schutz[175]	Niger	2.0	6.0	8.0	1.0	54.0	8.0	10.0	8.0	3.0	N
Schutz[175]	Mali	4.0	7.0	7.0	3.0	59.0	4.0	6.0	7.0	3.0	N
Schutz[175]	Senegal	6.0	5.0	2.0	4.0	58.0	3.0	10.0	10.0	2.0	N
Schutz[175]	N. Atlantic	4.0	6.0	6.0	2.0	57.0	4.0	8.0	6.0	7.0	Y
Leinen[176]*	E. Pacific	37.2	17.6	5.4	2.3	7.3	-*	10.7	-*	19.5	Y
Leinen[176]*	W. Pacific	38.6	15.0	0.9	2.6	9.4	-*	13.8	-*	19.7	Y
Arnold[177]*	NW. Pacific	68.7	9.1	3.0	5.0	7.1	-*	7.1	-*	0.0	Y
Jeong[178]	South Korea	19.0	1.0	1.0	2.0	28.0	8.0	11.0	8.0	22.0	N
Kandler[179]	Morocco (dust storm)	11.0	2.0	0.0	2.0	67.0	10.0	4.0	3.0	1.0	N
Kandler[179]	Morocco	26.0	4.0	0.0	3.0	24.0	25.0	4.0	14.0	0.0	N
Kandler[180]	Cape Verde	14.0	35.0	6.0	0.0	11.0	20.0	6.0	2.0	6.0	Y
Díaz-Hernández[181]	Spain	7.1	7.9	9.1	3.6	21.3	0.8†		14.2	36.0	N
All observations mean		30.3	9.3	2.8	3.0	27.2	5.0	7.2	5.4	9.8	
All observations st.dev.		23.7	7.8	3.2	1.3	21.2	7.1	3.4	4.6	11.6	
Transported observations mean		44.4	13.0	2.2	3.2	15.8	3.1	7.6	2.8	7.9	
Transported observations st.dev		22.0	8.7	2.6	1.6	15.0	6.1	3.3	3.2	8.6	

Table 7.1. Summary of aerosol mineralogy observations, in weight per cent. See also Figure 7.5 and Figure 7.6 for a summary of the observation locations and mean observed dust. Mineral type abbreviations (see section 7.2.2 for mineral descriptions): IL – illite, MI – Mica, KA – kaolinite, MO – montmorillonite, CH – chlorite, QU – quartz, KF – K-feldspar, NCF – Na/Ca-feldspar, CA – calcite, OT – other minerals includes less common minerals, such as gibbsite, goethite, gypsum, haematite, halite, palygorskite and unidentified material. Column ‘Tsp.’ shows if observations have been identified as transported a large distance from source (100s of km).*: These authors only tested for the six mineral types provided and did not report the K-feldspar or calcite fractions. †: only total feldspar content reported.

An example surface dust concentration predicted by GLOMAP is shown in Figure 7.4. Once dust concentrations and size distributions have been predicted the dust aerosol optical depth can be calculated for validation against satellite data (e.g. Ginoux *et al*. 2012[158], Figure 7.3). The modelled dust is consistent with the principle dust sources being the major deserts of Northern Africa and Western/Central Asia, along with minor seasonal sources in the smaller deserts of Australia, Northern America and Southern America.

Two different versions of the GLOMAP model exist, which simulate the size distribution of each aerosol species as either a series of lognormal distributions (GLOMAP-mode) or classified into a number of size bins (GLOMAP-bin). GLOMAP-bin has the advantage of a more explicitly quantified aerosol size distribution, at the disadvantage of a greatly increased computational cost. GLOMAP-mode does not explicitly carry the aerosol size distribution – mass is apportioned to a lognormal mode, and any mass loss/gain is applied proportionally across the whole mode. Therefore, in situations which require as accurate as possible knowledge of the aerosol size (and surface area) distribution GLOMAP-bin is the preferred option and is the version used in the work appearing in section 7.4.

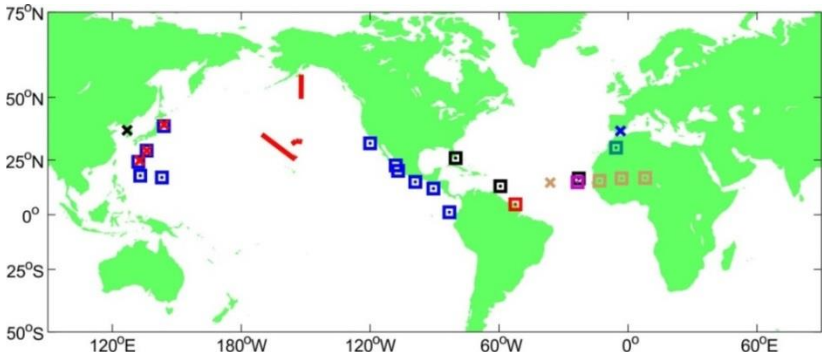

Figure 7.5. Locations of the sampling campaigns listed in Table 7.1. Left to right: black cross: Jeong[178]; blue squares: Leinen *et al*.[176] red crosses: Blank *et al*.[174]; red lines: Arnold *et al*.[177]; black squares: Glaccum and Prospero[172]; red square: Prospero *et al*.[173]; brown (squares: land stations; cross: approximate location of ship-borne observation): Schütz and Sebert[175]; purple square: Kandler *et al*.[180] (2011); green square: Kandler *et al*.[179] (2009); blue cross: Díaz-Hernández *et al*.[181].

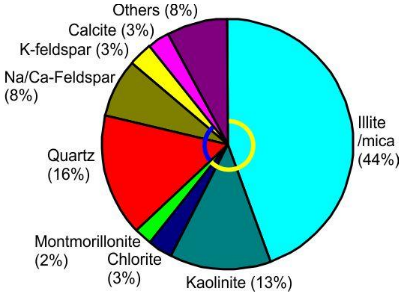

Figure 7.6. The average composition of atmospheric mineral dust by mass. This is limited to observations where dust has been transported 100s – 1000s km from source (Table 7.1, Tsp. = Y). The yellow arc denotes clay minerals, the blue arc framework silicates (quartz and feldspar). The category ‘Others’ is as defined in Table 7.1.

7.2.1. Composition of atmospheric mineral dust

While atmospheric dust concentrations and mineralogy vary spatially and temporally, a large fraction of observed atmospheric dust mass around the world is made up of just a few minerals. Individual minerals are classified by their crystal structure and chemistry and can be identified with X-ray diffraction techniques (see section 5.1). The average mineralogical composition of dust sampled from the atmosphere using filters is shown in Table 7.1. These observations originate from a number of locations around the world, mainly in the northern hemisphere tropical and sub-tropical regions (Figure 7.5). As with the dust concentration observations in Figure 7.2, the majority of observations are oceanic or coastal, with some observations taken from within Africa. The average composition of mineral dust that has been transported a distance from source (as denoted by the final column in Table 7.1) has been summarised in Figure 7.6. The clay minerals contribute approximately two thirds of dust mass (kaolinite 13%, montmorillonites 2%, chlorites 3% and micaceous minerals, such as the illites, 44%), with quartz (16%), feldspars (sodium/calcium feldspars 8%, potassium feldspar 3%) and calcite (3%) responsible for much of the remainder.

7.2.2. Description of mineral types

7.2.2.1. Clay minerals

The clay minerals, so called because their fine grained particles give clay its plastic quality when wet, are principally composed of layers of silicon and aluminium[148,182]. They usually form as alteration products of minerals such as feldspars and other igneous minerals[148,182]. Due to this, combined with their general softness and ability to be split along the layered structure, they are typically found as small particles[148,182]. The layered structures are typically based upon tetrahedra and octahedra containing 4+ and 3+ metal ions respectively, usually Si^{4+} and Al^{3+}. Substitutions within the structure can then occur, typically replacing a 4+ ion with a 3+, or a 3+ ion with a 2+ (e.g. Al^{3+} replacing Si^{4+}, Mg^{2+} replacing Al^{3+}).

Kaolinite has repeating aluminium and silicon layers in a 1:1 ratio (Figure 7.7). It is a common component of soil and has a density of approximately 2.65 g cm^{-3}, with a chemical composition of $Al_4Si_4(OH)_4O_{10}$. The substitution of the silicon and aluminium ions within kaolinite is infrequent, and hydrogen bonds provide inter-layer attraction. The relatively high strength of these inter-layer attractions prevents additional ions or molecules such as water from entering this region[148].

Montmorillonite is a common mineral of the smectite group, with a density of 2.35 g cm^{-3} and a 2:1 layered structure (see Figure 7.8). There are frequent substitutions within the aluminium octahedral layer, principally Mg^{2+} replacing Al^{3+}. The resulting charge imbalance is countered by the presence of cations within the interlayer region, usually Ca^{2+} or Na^{+}. The chemical composition resulting from these substitutions is $(Na,Ca)_{0.7}(Al,Mg)_4Si_8O_{20}(OH)_4 \bullet n(H_2O)$[148].

The size of the interlayer ions, combined with their distance from the negatively charged inner layer, results in weakly bound layers[182], with the consequence that the interlayer regions can be easily infiltrated by ions and polar molecules (especially water). As a result montmorillonite is a swelling clay with a high capacity for ion exchange[182,183]. This swelling characteristic can make identification of montmorillonite difficult via XRD as the layer separation, and therefore the diffraction pattern, can vary with humidity[148].

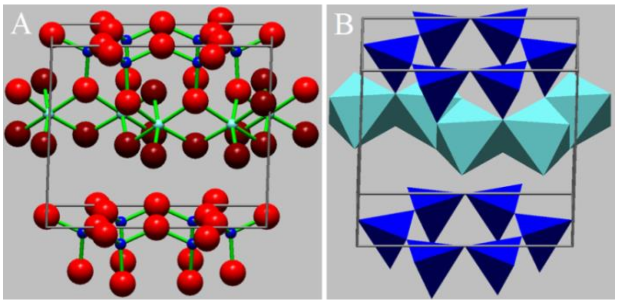

Figure 7.7. Representations of the structure of kaolinite. A) Ball and stick structure depicting the explicit location of the atoms within the structure: Light blue – Al^{3+}, dark blue – Si^{4+}, red – O^{2-}, dark red – OH^{-}. B) Polygonal representation: Light blue octahedrons represent $AlO_{0.5}(OH)_2$, dark blue tetrahedra representing SiO_2. In each polygon, the cation is positioned centrally and anions, which are shared between neighbouring polygons, occupy each point. As shown in the spherical representation OH^{-} ions occupy Al octahedra points not connected to Si tetrahedra. The grey frame represents the unit cell of the crystal structure. Drawn using the XtalDraw software package[184].

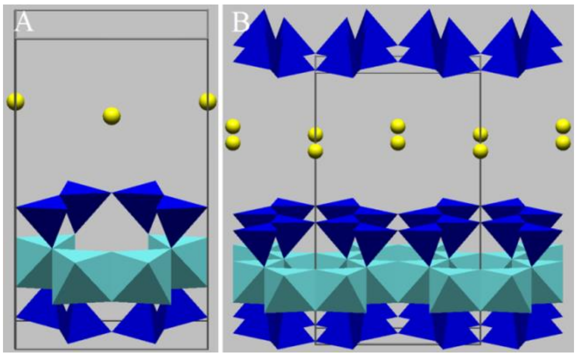

Figure 7.8. Polygonal representations of montmorillonite. A) the unit cell; B) an expansion of the structure showing the layering and hexagonal arrangements within the structure. Light blue octahedra represent AlO(OH), dark blue tetrahedra SiO_2 and yellow spheres interlayer Ca^{2+}. All polygon points represent O^{2-}, except for positions on Al polygons not connected to silicon tetrahedra, which represent OH^{-}.

Illite is one of the most prevalent minerals identified in the atmosphere (see Table 7.1) and has an average density of 2.75 g cm^{-3}. Its 2:1 structure is similar to that of montmorillonite (see Figure 7.9A) and muscovite. It has more frequent substitutions overall than montmorillonite, resulting in a higher layer charge and consequently stronger interlayer bonding and non-swelling structure, but less substitutions than muscovite[148] (Table 7.3). The layer charges are usually balanced by the addition of potassium ions between the repeating layers, with a general chemical composition of $K_{1.5}Al_4(Si,Al)_8O_{20}(OH)_4$[148]. Due to the similarity in structure between montmorillonite and illite, these minerals frequently form mixed layer clays such as rectorite, a 1:1 illite-smectite clay. A number of other forms of illite-smectite mixed layer clays exist; as exact classification by XRD of these clays is difficult, they are usually classed as illite-smectite mixed layer clays.

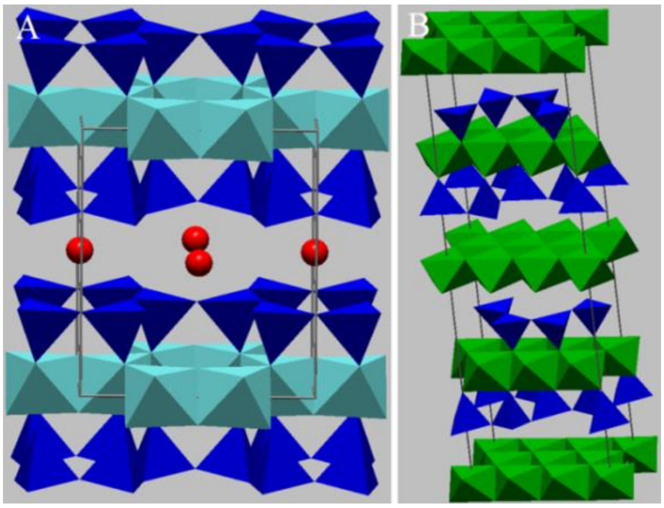

Figure 7.9. Polygonal representation of illite and chlorite. A) Illite, with the same colour coding as montmorillonite (Figure 7.8), but with red spheres representing K^+. Note the smaller separation between layers of illite vs. montmorillonite. B) The unit cell of chlorite, with green octahedra representing a range of metal ions, typically Mg^{2+}, Fe^{2+} or Al^{3+}. The majority of octahedron points in chlorite represent OH^- groups, with O^{2-} at positions connected to Si tetrahedra (blue).

Mineral	'X'	'Y'	'Z'	OH^-	O^{2-}
Muscovite	K_2	Al_4	Si_6Al_2	4	20
Hydro-muscovite A	$(K,H_3O^+)_2$	Al_4	Si_6Al_2	4	20
Hydro-muscovite B	K_{2-x}	Al_4	Si_6Al_2	$4+x$	$20-x$
Illite	K_{2-x}	Al_4	$Si_{6+x}Al_{2-x}$	4	20
Phengite	K_2	$Al_{4-x}(Mg,Fe^{2+})_x$	$Si_{6+x}Al_{2-x}$	4	20

Table 7.2. The relationship between muscovite and the illite mineral group. The minerals in this table have the same basic structure composed of atoms/ions in set positions 'X', 'Y' and 'Z' and the complete mineral composition is the sum of all five columns. x represents substitution relative to muscovite, 0.5 is often assumed for illite. From Deer *et al.*[148].

Illite is primarily formed by the weathering of feldspar[182], and is found as a component member of shale rocks[148]. Examples of shale have been found to contain up to 30 %, but generally more around 5 %, feldspar by mass[163]. Due to this formation method there was difficulty in locating a sample of illite which did not contain significant amounts of other minerals (Table 7.3). A number of the observations of atmospheric mineral dust (Table 7.1) did not differentiate between illite and the mineral mica. Therefore muscovite, the mica most resembling illite, was used as a proxy for illite in the experiments described in section 7.3.

Muscovite mica is a layered silicate structurally and elementally very similar to illite[148]. The principle difference is the lack of any ion substitutions in muscovite, with a chemical composition of $K_2Al_6Si_6O_{20}(OH)_4$. Substitutions within this structure result in several minerals (hydro-muscovite, illite and phengite, Table 7.2) dependent upon the number and form of these substitutions. While hydro-muscovite and phengite are technically not illites, they are sometimes included in what is referred to as the illite group of minerals. As micas can be formed from igneous and metamorphic processes[148], it can form very large single crystals weighing several tons[185] allowing the acquisition of high purity samples. As its crystals also tend to be larger it is generally not referred to as a clay mineral, despite the similarities to illite.

Sample	Source	IL/MI	KA	MM	CH	QU	FNC	FK	CA	Others
NX Illite	Arginotec	60.5	7.2	ND	ND	6.6	1.7	8.1	2.1	I-S 13.8
Illite	Wards, USA	92.7	ND	*	ND	2.3	1.1	2.0	ND	Unidentified 1.9
IMT 1	Clay Min. Soc., USA	90.5	ND	ND	ND	ND	ND	7.7	1.8	ND
Illite	Arkansas, private collection	58.7	ND	ND	5.1	18.6	1.0	2.1	ND	I-S 14.1 Dolomite 0.3
Illite	'Marblehead'	17.0	ND	*	9.6	4.1	3.8	13.7	ND	I-S 40.5 Unidentified 4.4 Halite 2.6 Barite 1.6 Pyrite 1.4 Dolomite 1.3

Table 7.3. XRD mineralogies of a number of illite samples, in weight per cent. Several other 'illite' samples were acquired but either had obvious contamination or were not illite but actually a mixture of montmorillonite and illite-smectite mixed layer clays. Mineral abbreviations as per Table 7.1, ND means this mineral type was not detected by the XRD. I-S: illite-smectite mixed layer clay. *:montmorillonite was not directly observed and is included in the unidentified material. Mineral compositions were produced using XRD (see Section 5.1) by Dr T.L. Malkin as part of work for Atkinson *et al*.[107]

Chlorite is not always classified as a clay mineral[148], but as it is a phyllosilicate (layered structure) mineral and is usually found in the same size range as typical clays (i.e. typically less than 2 µm) it is often included in the classification[175,182,186]. Chlorite refers to a group of minerals with a layer structure which is similar to a 2:1 clay, but with some important differences. Ion substitutions are more frequent than in illite and muscovite, but unlike these rather having single atom ions in the interlayer region chlorite contains a layer of metal hydroxide octahedra resulting in a 2:1:1 structure (see Figure 7.9B). This structure is strongly bound and non-swelling. Members of the chlorite group are classified by the primary non-aluminium-silicon ion present, such as clinochlore (magnesium, $(Mg_{10}Al_2)(Al_2Si_6)O_{20}(OH)_{16}$) and chamosite (iron(II), $(Fe^{2+}{}_{10}Al_2)(Al_2Si_6)O_{20}(OH)_{16}$), with densities in the range of 2.6-3.3 g cm^{-3} (refs [148,182]).

7.2.2.2. Framework silicates

In comparison to clays the framework silicates (e.g. quartz and feldspar) lack the clearly layered structure and thus tend to be harder. This hardness gives a resistance to physical erosion which makes them common in sedimentary rock formations, especially in the case of quartz[148].

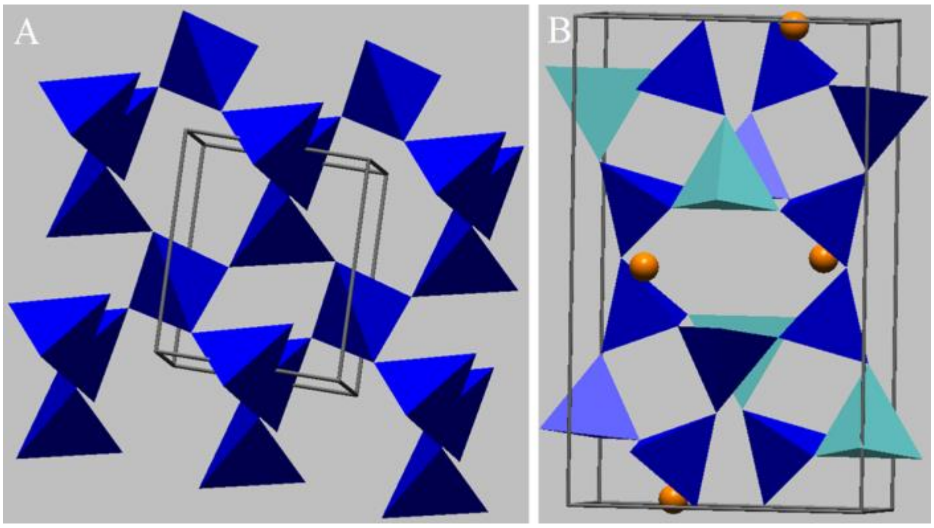

Figure 7.10. Polygonal representations of quartz and feldspar. A) quartz, which consists of SiO_2 tetrahedra arranged in six membered loops. B) the feldspars albite and microcline, with dark blue tetrahedra representing SiO_2 and light blue representing AlO_2^-, arranged in loops of four. Orange spheres represent Na^+(albite) or K^+ (microcline) which balances the AlO_2^- charge. In anorthite, a Calcium feldspar, these ions are instead Ca^{2+} and double the number of Al^{3+} for Si^{4+} substitutions.

Quartz is a primary mineral which is present in most igneous rocks, with a structure formed exclusively of silicon dioxide tetrahedra arranged into six membered loops (see Figure 7.10A). This results in a chemically resistant and very strong (Mohs hardness of 7) crystal structure which has a density of 2.65 g cm^{-3} which breaks up into granular particles with a lower surface area to volume ratio than the layered clays. In contrast to the softer clay minerals this hardness results in a resistance to erosion resulting in the presence of quartz in most sedimentary rocks, including clay formations[148].

The feldspar group of minerals are the most common crustal minerals[186]. They are primary minerals usually of igneous origin, which are found in most volcanic ashes and constitute a large proportion of common rocks such as granite[148]. Similarly to quartz the feldspars are composed of a framework of tetrahedra, except with some silicon replaced by aluminium and the resulting negative charges balanced by the addition of a cation. Potassium and sodium feldspars have Al:Si ratios of 1:3, calcium feldspar Al:Si = 1:1. The structure of the sodium feldspar albite is shown in Figure 7.10B. The hardness of the feldspars (6-6.5 on the Mohs scale) means they are resistant to physical erosion[148]. The feldspar minerals all have densities around 2.5-2.7 g cm^{-3}. The chemical compositions of the feldspars are $KAlSi_3O_8$ (orthoclase/microcline), $CaAl_2Si_2O_8$ (anorthite plagioclase) and $NaAlSi_3O_8$ (albite plagioclase); the plagioclase feldspars form a series of minerals composed of mixtures of anorthite and albite[148].

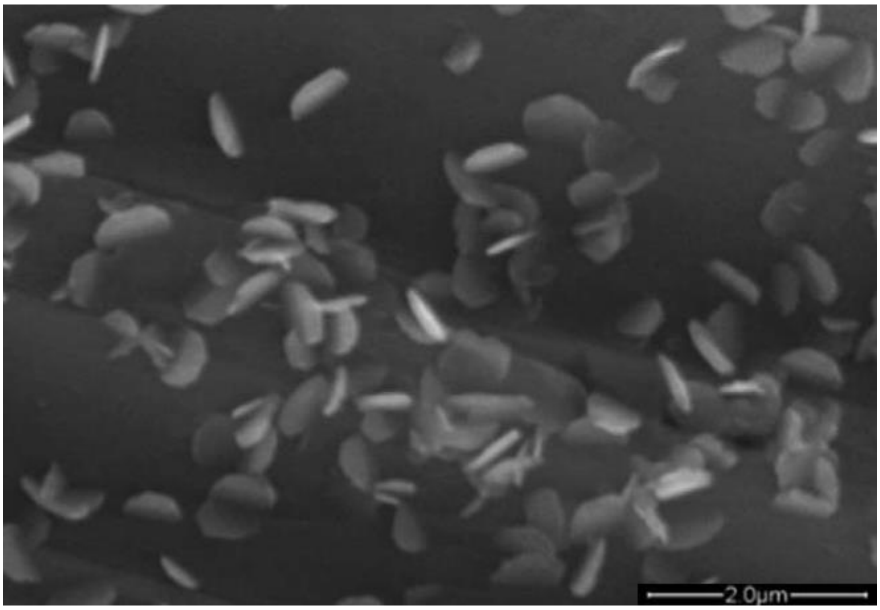

Figure 7.11. Scanning electron microscope images of the surface of a microcline crystal after a laboratory based acid weathering experiment. The platy structures visible are crystals of kaolinite. The experiment lasted for 27 days at 200 °C and a pressure of 300 bar in a KCl and CO_2 solution. Taken from Zhu *et al*.[187].

When weathered by acids the feldspars form clay minerals such as kaolinite, montmorillonite and illite[148,182,187-189]. As this weathering occurs at the accessible surfaces of the feldspar, any clay products can precipitate onto this feldspar surface (see refs [187,188], Figure 7.11). This may result in the reduction of the feldspar surface area available for ice nucleation.

7.2.2.3. Calcite

Calcite ($CaCO_3$) is a common carbonate mineral and is the principle component of a number of common sedimentary rocks including limestone and chalk[163]. Due to its softness (Mohs hardness of 3, see Figure 7.12 for its structure) it easily breaks up into small grains[148]. It reacts readily with acids, and via reactions with atmospheric sulphuric acid may be processed into gypsum[190], potentially buffering the chemical weathering of any accompanying feldspar. It has a density of 2.7 g cm^{-3} (ref [148]).

7.2.3. Ice nucleation by mineral dusts in the literature

The principle source of atmospheric mineral dust is desert regions (Figure 7.3), and laboratory investigations into immersion mode freezing by mineral dust has concentrated upon samples collected in these regions[30,31,37,40,96,109]. Additionally commercially available mixed dusts have been analysed as a proxy for field samples[37,40,47,80,109,139,191,192]. Of the natural and commercial mixed dusts the commercial dust mixture Arizona Test Dust (ATD) gives the highest measured nucleation coefficients[37,80,109,139] (Figure 7.13), followed by natural dusts[37,40] and the commercial mixed dust NX illite[40,47]. The mineralogy of ATD is a mixture of feldspar (~30 %), quartz (20 %) and clays (40 %), whereas NX illite is ~80 % clays (illite, kaolinite and illite-smectite mixed layer clay) with less than 10 % each of feldspar and quartz[47]. The composition of the natural mineral dusts used was not reported.

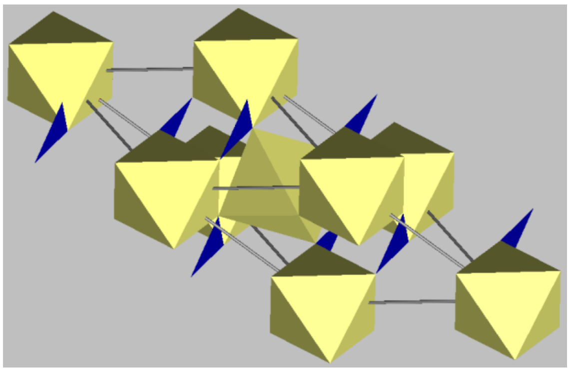

Figure 7.12. Polygonal representations of Calcite. Yellow octahedrals represent Ca^{2+} and blue triangles represent CO_3^{2-}. All polygon points are occupied by O^{2-}.

As well as mixed mineral dusts, there have been immersion mode freezing experiments performed on a number of clay samples, specifically of kaolinite[38-42], montmorillonite[38-40,114] and illite[38]. In some measurements the mineral concentrations[38,39] and surface areas[38,39,114] were not provided; for these studies a range of values has been plotted in Figure 7.13 corresponding to the reasonable ranges of mineral concentration (0.01 – 10 wt%) and specific surface area (5 – 30 m^2 g^{-1} for kaolinite, 10 – 100 m^2 g^{-1} for illite, 10 – 300 m^2 g^{-1} for montmorillonite). There have been two further studies of kaolinite which supplied n_s values or enough information to calculate them[41,42]. The ice nucleating activities of the majority of these clays is lower than that for ATD and the natural dust samples, though some exhibit similar n_s values to ATD (Figure 7.13).

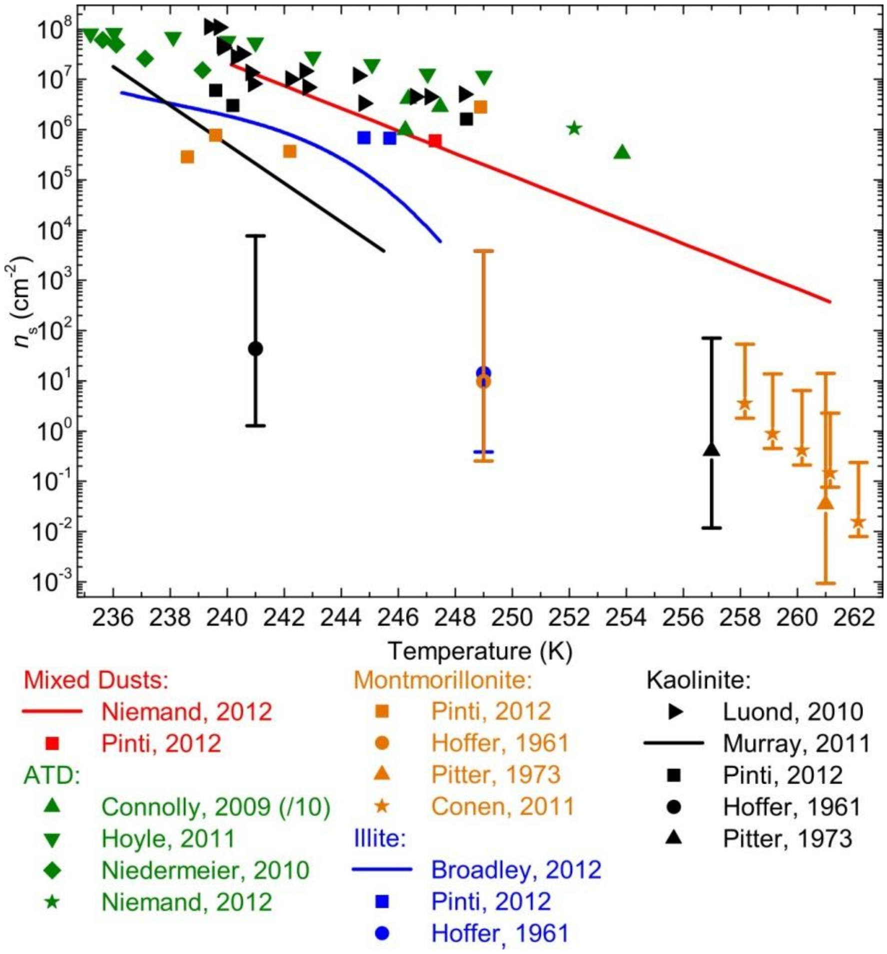

Figure 7.13. Nucleation coefficients for mineral dusts from the literature. Where shown, error bars represent the range of possible values based upon reasonable estimations of mineral concentration and surface area; the points shown for these data sets are for identification only and do not correspond to a reported or suggested value. Where only the freezing onset was provided, as by Pinti *et al*.[40], a fraction frozen of 5 % was assumed. Murray *et al*.[41] and Broadley *et al*.[47] were the only authors to provide mineralogy. The results from Connolly *et al*.[109] have been reduced by a factor of 10 as per Niemand *et al*.[37] [37-42,47,80,109,114,139].

Of the single mineral data sets only the kaolinite analysed by Murray *et al*.[41] has a known mineralogical composition (96 % kaolinite). In comparison, the kaolinite observed by Lüönd *et al*.[42] produced n_s values 2-3 orders of magnitude higher, and the difference was not thought to be due to contrasting experimental techniques alone[41]. Additionally, experiments by Pinti *et al*.[40] using differential scanning calorimetry imply that in some minerals (e.g. montmorillonite SWy-2, kaolinite K-SA) ice nucleation may be due to two different particle types.

Of the eight minerals listed in Section 7.2.1, the immersion mode ice nucleating ability of only three have been investigated as single mineral samples, of which only one has a quantified mineralogy. To improve our understanding of atmospheric mineral dust ice nuclei, the ice nucleating ability of high purity samples of the remaining 7 minerals have been analysed.

7.3. Experimental study of the ice nucleating ability of mineral dusts

The characterisation of the mineral samples preceded the analysis of their ice nucleating behaviour, with X-Ray diffraction used to determine the sample mineralogy (Section 5.1) and nitrogen gas adsorption used to estimate the specific surface area (Section 5.2). The characteristics of the mineral samples are summarised in Table 7.4. The specific surface areas of the clay minerals are generally around an order of magnitude higher than the other minerals, which results in much smaller estimated mean particle diameters. The montmorillonite was used as supplied whereas all other minerals were supplied as coarse powders or pebbles and required grinding (in an agate ball mill or mortar and pestle, see Section 3.2.1) to generate a fine dust, with specific surface area measurements and XRD analysis (during which no agate was detected) performed after grinding. The ice nucleating behaviour of each mineral was then determined using the droplet freezing technique described in Chapters 3 and 4.

7.3.1. Results and discussion

The freezing of hundreds of micron-sized droplets containing a known amount of each mineral was observed in experiments using a cooling rate of 1 K min^{-1}, the details of which are summarised in Table 7.5. In experiments with very similar dust surface areas, the temperature at which 50% of droplets were frozen was 250.5 K for K-feldspar (Figure

7.14A), followed by Na/Ca-feldspar at 247 K, quartz at 242.5 K, with calcite and the clay minerals at below 237.5 K. The surface area of mica had to be increased by around an order of magnitude relative to the other experiments as it froze at temperatures very similar to homogeneous. These results suggest that it is the feldspar minerals, in particular K feldspar, that cause mineral dust to be effective immersion mode ice nuclei in the atmosphere. This data contrasts with the prevailing view (see for example Murray *et al.*[30] and references therein, Hoose and Möhler[31] and references therein) that clay minerals are the most important component of atmospheric mineral dust for ice nucleation.

Droplet freezing temperatures are dependent on experimental parameters such as droplet volume and the surface area of the material immersed in the droplet. This makes comparison with other experiments and samples of the same mineral difficult as droplets with different quantities of suspended material will freeze at different temperatures[30]. To normalise the efficiency with which a material nucleates ice, the surface density of nucleation sites per unit surface area is determined[30,68,109] (n_s; see Chapter 2, Equation 2.31).

Mineral	Source	SSA ($m^2\ g^{-1}$)	BET dia. (µm)	X (%)	Composition (%)
Calcite	In house	6.0	0.4	2.8	99.6 calcite 0.4 unidentified
Chlorite	In house	25.0	0.08	3.2	99.6 chlorite 0.4 unidentified
K-feldspar	BCS 376, Bureau of Analysed Samples, UK	3.2	0.7	3.1	80.4 K-feldspar 16.0 Na/Ca-feldspar 3.9 quartz
Na/Ca-feldspar	BCS 375, Bureau of Analysed Samples, UK	5.8	0.4	7.6	76.6 Na/Ca-feldspar 16.7 K-feldspar 4.0 quartz Ilmenite 1.8 unidentified 0.9
Mica	SJ Mica, USA	28.2	0.08	44.4	98.2 mica 1.8 unidentified
Montmorillonite	STx-1, Clay Min. Soc., USA	91.4	0.03	2.2	67 montmorillonite[193] 30 Opal-CT 3 quartz
Quartz	Riedel-De Haën (Sigma Aldrich)	2.7	0.8	15.8	98.6 quartz 1.4 unidentified

Table 7.4. Characteristics of experimental mineral samples. Na/Ca feldspar is an example of albite, a low calcium plagioclase feldspar, and K-feldspar an example of microcline. SSA: specific surface area of the sample measured by BET N_2 adsorption (Section 5.2) after grinding. BET dia.: the surface area estimated mean particle diameter (Section 5.2, Equation 5.8). X: the contribution of this mineral to the mean observations as per Table 7.1. Mineral compositions were produced using XRD (Section 5.1), by Dr T.L. Malkin as part of work for Atkinson *et al.*[107] except montmorillonite (ref [193]).

This method of quantifying ice nucleation neglects the role of time dependence in nucleation, on the basis that ice nuclei particle-to-particle variability is more important than the time dependence of nucleation[30,68,109,110]. As the focus was to determine the ice nucleation abilities of the minerals relative to each other, experiments to investigate the time dependence of freezing by the different minerals were not performed and such investigations would be beneficial in the future. The n_s values derived for 9 - 19 µm size droplets are shown in Figure 7.14B. As suggested by the freezing temperatures, the feldspars are the most efficient of the minerals common to atmospheric dust, by surface area.

From these n_s values it is possible to calculate a statistical uncertainty in the fraction frozen data. While freezing events are observed explicitly and do not have an uncertainty, they occur due to a probabilistic process and therefore have some natural scatter. It is not possible to directly estimate the magnitude of this scatter by comparison to a fit of the fraction frozen. Instead, a log-linear fit to the n_s values is used to predict the fraction frozen, and the uncertainty in the fraction frozen is calculated as the root-mean-square difference between the predicted and observed fractions frozen (Figure 7.15).

Mineral	MI	MM	CH	QU	NCF	KF	CA
Wt. %	0.760	0.028	0.101	0.916	0.434	0.798	0.419
10 µm #	64	17	46	70	38	31	18
10 µm SA	7.13	0.84	0.84	0.85	0.84	0.84	0.85
12.5 µm #	60	21	28	60	30	23	36
12.5 µm SA	13.92	1.64	1.64	1.67	1.63	1.63	1.67
15 µm #	41	20	20	39	23	19	30
15 µm SA	24.06	2.84	2.83	2.88	2.82	2.82	2.88
17.5 µm #	21	-	-	18	21	19	24
17.5 µm SA	38.21	-	-	4.58	4.48	4.48	4.57

Table 7.5. Summary of the experimental parameters. The experiment weight per cent (Wt. %), number of droplets in each measurement-bin (X µm #) and the surface area of mineral dust immersed within droplets of each size (X µm SA, in 10^{-7} cm^2) are provided. There were insufficient droplets in the 17.5 µm diameter size for both montmorillonite and chlorite. See Table 7.1 for mineral abbreviations.

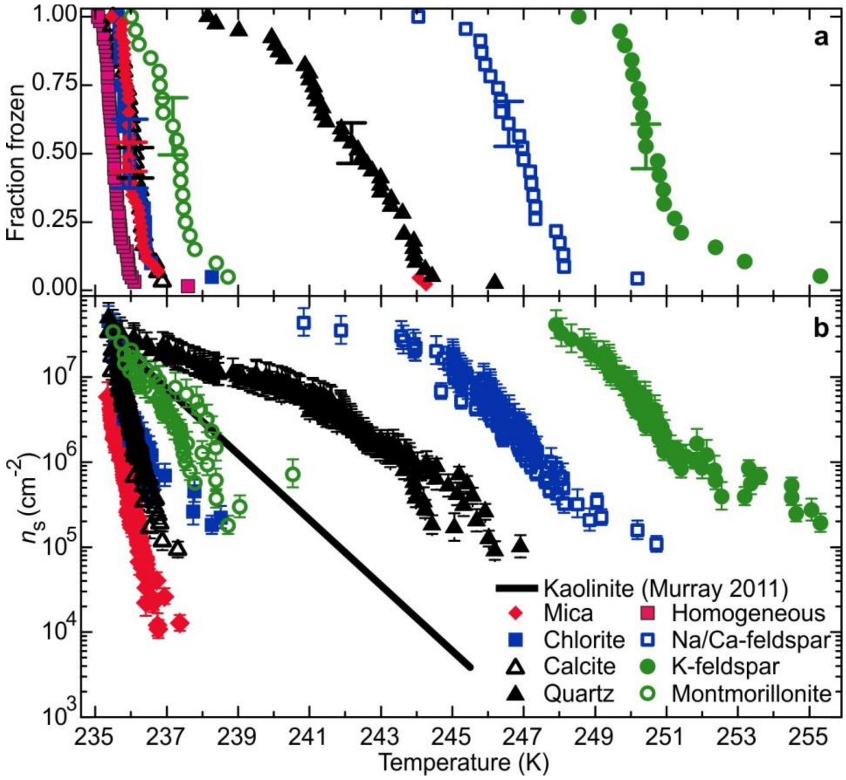

Figure 7.14. Experimental freezing results for the individual minerals. A) Fraction of droplets, 14-16 μm diameter and containing a range of mineral dusts, frozen as a function of temperature during cooling. An experiment where droplets froze homogeneously is shown for comparison. Temperature uncertainty is not shown and is estimated at ±0.3 K (section 3.2). The indicated uncertainty in the measured fraction frozen is the root-mean-square error (68 % confidence limit, see Figure 7.15). B) Nucleation site densities (n_s, cm^{-2}) for droplets between 9 and 19 μm diameter calculated individually for each measurement-bin. The uncertainty in n_s is primarily due to droplet size measurements and temperature uncertainty is as in A). The kaolinite parameterisation is from Murray *et al.*[41].

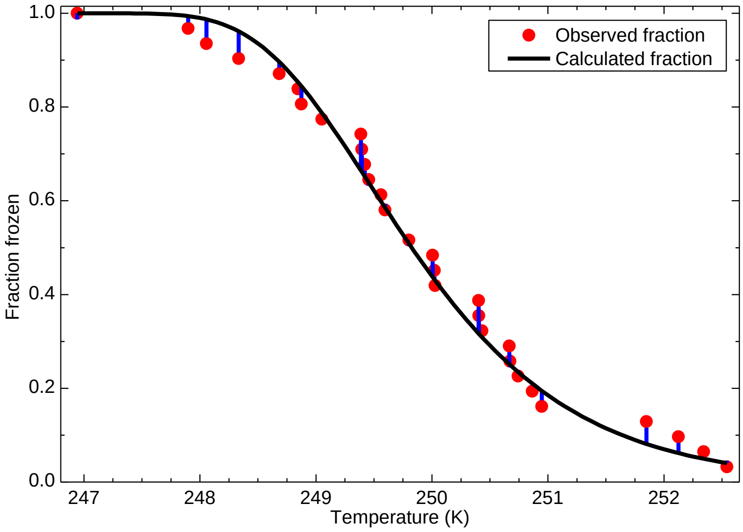

Figure 7.15. Comparison of the observed fraction frozen with the calculated fraction frozen. The calculated fraction frozen is derived from the ln-linear fit to n_s (Figure 7.14B). The errors provided in Figure 7.14A are the root-mean-square of the differences between the calculated and observed fraction frozen (blue lines). The experimental data shown is for K-feldspar immersed in 10 ± 1.25 μm diameter droplets freezing.

In natural airborne dusts the abundance of each mineral can vary greatly and the clay minerals tend to be much more abundant than feldspar. Therefore, it is not immediately clear which mineral, if any, will dominate ice nucleation in the atmosphere. To investigate this, the n_s values presented in Figure 7.14B were combined with the average mineralogical composition of atmospheric dust to estimate the temperature-dependent ice nuclei concentration (shown in Figure 7.16A). To enable surface area estimation it has been assumed that all particles are spherical.

Two limiting calculations have been made, one assuming that dust particles are internally mixed (i.e. all particles contain the same mixture of all eight minerals) and the other assuming they are externally mixed, where each particle is entirely composed of a single mineral:

$$IN_x = n_x\left(1 - \mathrm{e}^{\sum_y n_{\mathrm{s},y}\sigma_x m_y}\right) \qquad \textbf{Equation 7.1}$$

$$IN_{x,y} = n_x m_y (1 - \mathrm{e}^{n_{\mathrm{s},y}\sigma_x}) \qquad \textbf{Equation 7.2}$$

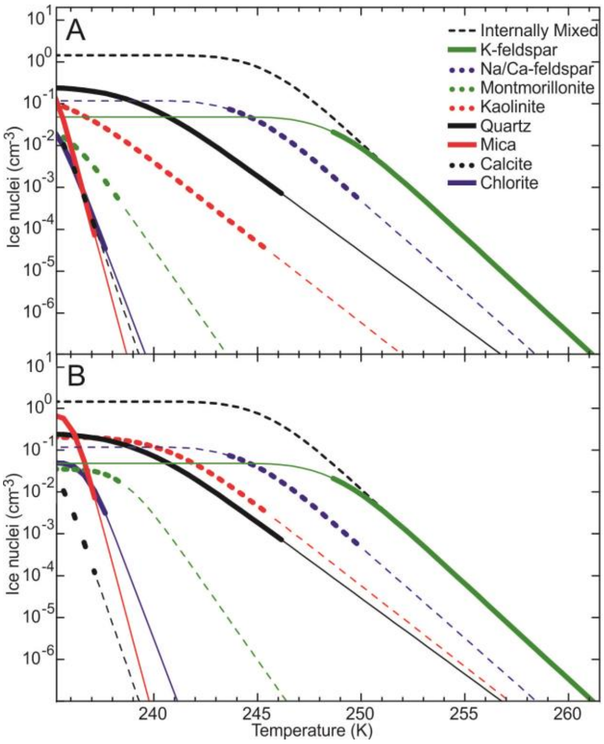

Figure 7.16. An estimation of atmospheric ice nuclei concentrations due to various minerals. Ice nuclei concentrations were estimated using Equations 7.1 and 7.2 with the abundance of each mineral from Table 7.1, taking an annually and globally averaged dust concentration (1.4 cm^{-3}) from the GLOMAP model (see Section 7.4) and the n_s values in Figure 7.14B. A) Particles are assumed to be spheres with a size distribution from the GLOMAP model. B) Particle size distributions are as in A), except with the surface areas of clay particles (kaolinite, mica, chlorite and montmorillonite) enhanced by a factor of 100. Lines with specific mineral names refer to externally mixed individual minerals. Thick lines denote the range of experimental data and thin lines extrapolations outside this range.

where n_x is the number of dust particles of size x, m_y is the mass fraction of mineral y within size x, and $n_{s,y}$ is the time-independent surface area normalised ice nucleation coefficient of mineral y. In the internally mixed case (Equation 7.1) the sum of the contribution to the freezing probability from the surface of each mineral is calculated, whereas in the externally mixed case (Equation 7.2) the number of frozen droplets due to particles of each mineral is calculated. The actual mixing state of atmospheric dust is poorly constrained but will fall between these two limiting cases (e.g. ref [178]).

Despite only accounting for 3% of atmospheric dust by mass, K-feldspar dominates the number of ice nuclei above 248 K in both the internally and externally mixed cases. The overall number of predicted ice nuclei is higher in the internally mixed case, as a small part of the surface of every dust particle is classified as K-feldspar. However, it has been suggested that clay mineral particles will typically be a smaller size than feldspar or quartz[172], and therefore may have a greater surface area per unit mass which would increase the concentration of clay ice nuclei. If these calculations are reproduced with the surface area of the clays increased by two orders of magnitude, which may be an overestimate[47], the feldspars remain the dominant ice nucleating minerals (Figure 7.16B).

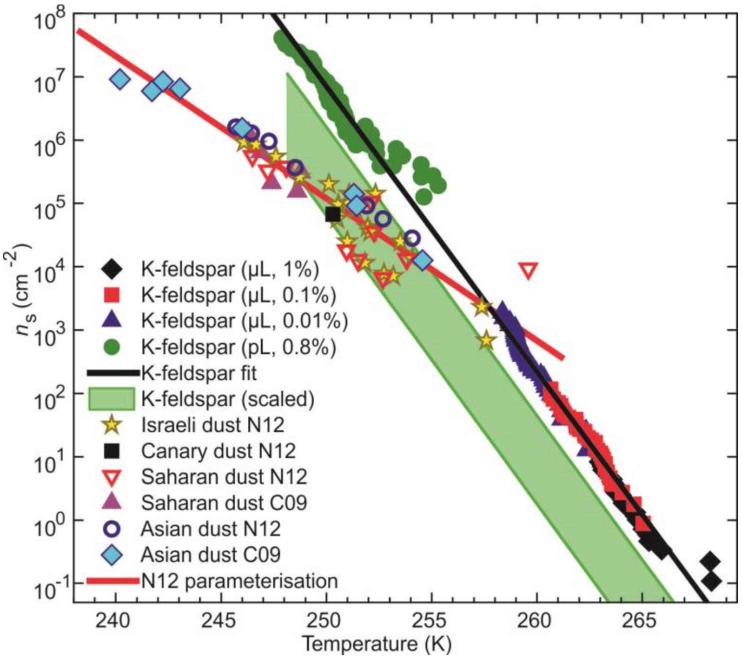

Figure 7.17. Nucleation site density (n_s, cm^{-2}) for K-feldspar and natural dusts. Data from Figure 7.14B (pL) extended to higher temperatures by use of μL sized droplets in experiments using the microlitre stage (section 3.3) performed by T. Whale. A log-linear fit is provided ($\ln(n_s) = -1.038T + 275.26$, valid between 248 and 268 K). Experimental K-feldspar concentrations in weight per cent are provided in the key, temperature uncertainties for μL experiments (not shown) were estimated at ±0.4 K, n_s ±25 %. Literature data for several natural dust samples from Niemand *et al.* (N12)[37] and Connolly *et al.* (C09)[109] are provided.

Since clouds glaciate over a wider range of temperatures than is achievable in the experiments presented above, it is important to further quantify the nucleating efficiency of atmospheric ice nuclei over a broader temperature range. For example, Crawford *et al.*[194] suggest that a concentration of as few as 10^{-5} cm^{-3} ice nuclei in a cloud at ~266 K could trigger substantial glaciation via the Hallett-Mossop ice multiplication process[195]. Therefore, measurements are needed at these higher temperatures. In order to extend the data for K-feldspar to this temperature regime, a series of experiments was performed with larger droplets (see section 3.3), which allows for a larger particle surface area per droplet and correspondingly lower value of n_s to be quantified. Results for K-feldspar using droplets of 1 μL volume are shown in Figure 7.17, which extends the range of experimental data up to 268 K. Combining the two techniques allowed n_s values to be determined over a range of eight orders of magnitude.

For comparison, cloud chamber derived n_s values for a range of natural mineral dusts sampled from arid source regions by Niemand *et al.*[37] and Connolly *et al.*[109] are provided in Figure 7.17. Since feldspar is a major component of the Earth's crust it is ubiquitous in soils around the globe[148]. K-feldspar makes up as much as ~24% by mass of soils throughout the Asian and African dust belt[196] (see Figure 7.18) and is also present in airborne dust in concentrations ranging from one per cent[181] to as high as twenty five per cent[180]. As the mineralogical compositions of the dusts used by Niemand *et al.*[37] and Connolly *et al.*[109] are unknown, scaled n_s values for K-feldspar are also shown. This scaling has been done by assuming the contribution to the natural dust particles' surface is the same as it is to the mass of dust, which ranges between 1 and 25 % in Table 7.1.

The mineralogical composition of soils in arid regions around the world varies substantially. To quantify the global distribution of ice nuclei concentrations due to K-feldspar beyond simple global calculations such as Figure 7.16 it is necessary to use a global aerosol model.

7.4. Global modelling study

7.4.1. Description of model

GLOMAP is a size- and composition-resolving two-moment microphysical aerosol scheme[197] run within the TOMCAT chemical transport model[198], which has previously been used to study the atmospheric processing of mineral dust[199]. The model is driven by

ERA-40 reanalysis meteorology for the year 2000[200] and has been extended to represent nine mineral types (see section 7.4.1.1). Typically the model only contains tracers tracking sulphate, sea-salt, mineral dust without any mineralogical detail, black carbon and organic carbon aerosol. To enable the expansion to nine dust tracers while maintaining the ability to run the model in a usable amount of time these original tracers were removed and the processes of nucleation scavenging (e.g. cloud condensation, ice nucleation and precipitation) disabled. Sedimentation and dry deposition processes were still modelled. Dust emissions are prescribed from AEROCOM recommendations for the year 2000[201] (section 7.4.1.2). The model was run with a horizontal resolution of 2.8°, with 31 vertical levels between the surface and a pressure level of 10 hPa.

7.4.1.1. Model mineralogy

A global map of the mineralogy of arid and semi-arid regions has been produced by Nickovic *et al.*[196]. This map, an update of an earlier map by Claquin *et al.*[202], provides the contribution of a number of minerals to the clay (<2 µm) and silt (2 – 50 µm) size fractions of soils in these regions. The minerals detailed are quartz, hematite, calcite (in both size fractions for all three), illite, kaolinite, smectite/montmorillonite (clay fraction only), gypsum, total feldspar (both silt fraction only, see Figure 7.18 for the feldspar distribution) and total phosphorous. The map is based upon a soil type map produced by the Food and Agriculture Organisation, part of the UN.

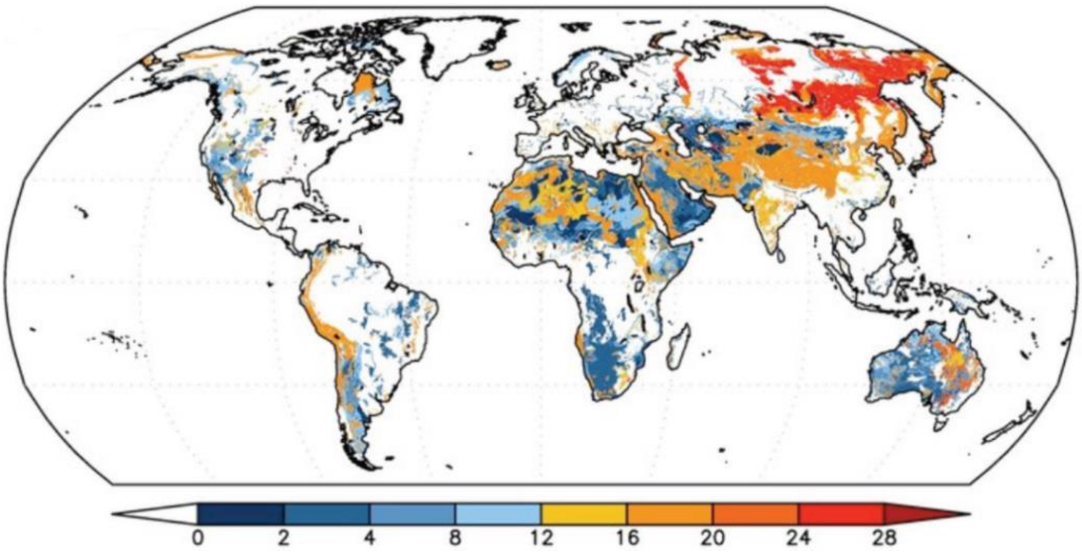

Figure 7.18. Global distribution of feldspar of the silt size fraction of arid soils, in weight per cent. From Nickovic *et al.*[196].

The clay and silt fraction of each soil is then assigned a typical mineralogy from the literature (see for example Table 1 of Claquin *et al.*[202]). In compiling this map, it has been assumed that the mineralogy of a soil is independent of the geology of a region. However, while the ratio of silt to clay particles is a specific part of the soil classification, the ratios of the minerals within these size ranges will vary from location to location. To date there is no comprehensive surface mineralogy map using in-situ measurements available, so this assumption has to be accepted. The soil mineralogy map has been made available as a global database with 30 seconds of a degree resolution.

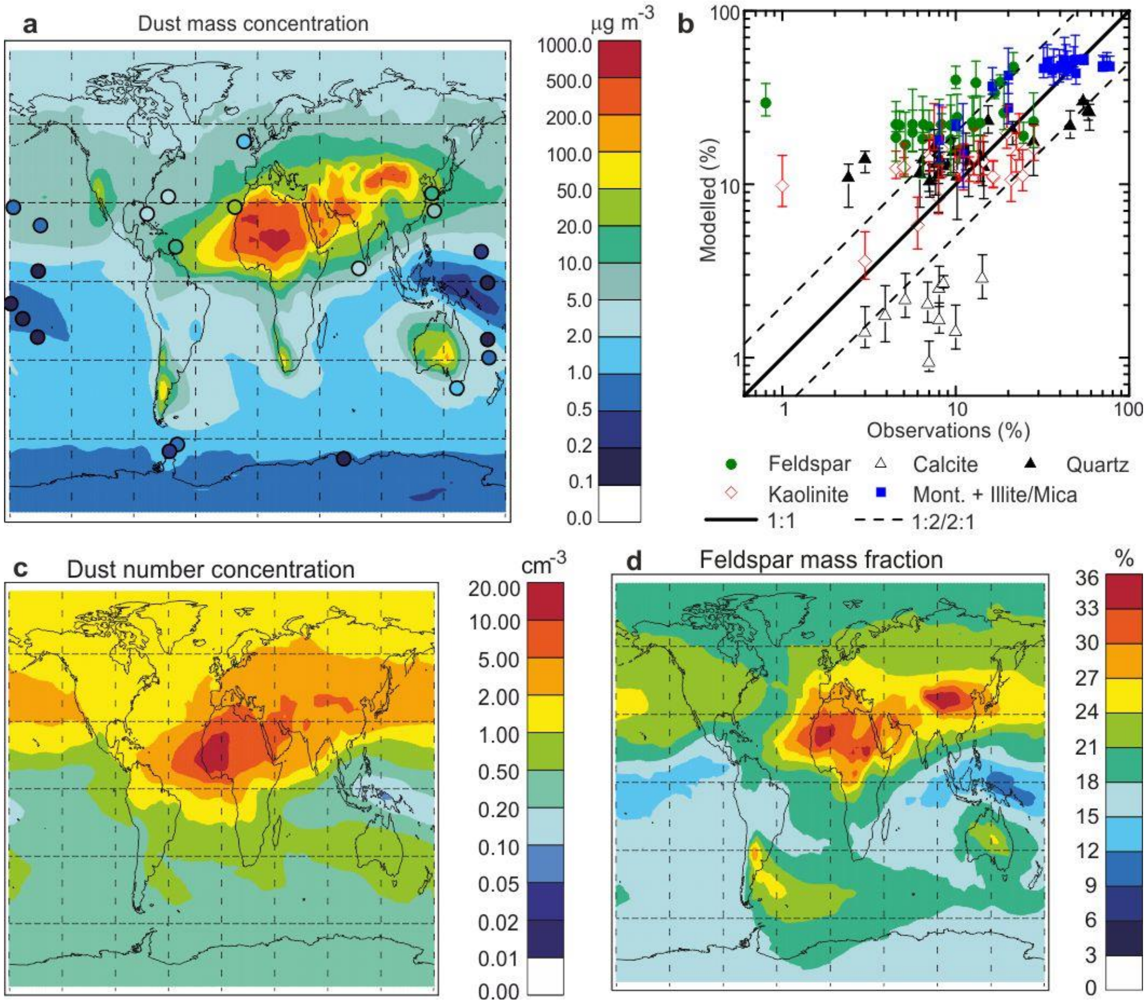

Figure 7.19. Comparison of modelled mineral dust with observations. A) Modelled surface dust mass concentrations compared with measurements from Woodward[168], from modelling work by Dr M. Woodhouse as part Atkinson *et al.*[107]. B) Modelled near-surface dust compositions compared with observations (Table 7.1). Vertical error bars represent the range of modelled monthly mean values. 1:1 and 2:1 lines are also shown for convenience. C) Modelled total dust number concentration at 600 hPa altitude. D) Modelled feldspar mass fraction of dust at 600 hPa.

Dust is represented in GLOMAP by 12 size bins ranging from 0.1 µm to >20.0 µm diameter, with the clay fraction placed in bins below 2 µm diameter. Each mineral type listed above has its own set of bins. As the mineralogy within the Nickovic *et al.*[196] database does not add up to 100 % in all locations a ninth mineral 'type' called others is included to carry the remaining material. For undeclared reasons, likely due to a lack of evidence in the soil mineralogies, Nickovic *et al.*[196] and Claquin *et al.*[202] did not include feldspar in the soil clay fraction. However, observations of atmospheric dust (e.g. Kandler *et al.*[179] and Arnold *et al.*[177]), show that feldspar is not absent from this size fraction. To adjust for this it was assumed that the ratio of quartz to feldspar in the clay fraction is the same as the silt fraction, after which the clay fraction composition was re-normalised to 100 %. This is based upon the principle that the particle size below which quartz and feldspar cease to be present is linked to the degree of weathering experienced by the soil[203]. However, this may be an over estimation as quartz tends to be present at smaller sizes than feldspar[203].

The soil feldspar content was provided without apportionment between K-feldspar and Na/Ca-feldspar. Therefore, 35 % of the feldspar mass was apportioned to K-feldspar based upon the ratio of these minerals in the atmospheric dust observations of Table 7.1, where the observation specified the feldspars individually and the observation was classed as transported. The transported classification gives a feldspar ratio unaffected by local variations in mineralogy and thus more representative of a global average. Chlorite was also not included in the surface mineralogy due to its low concentration[202]; as the atmospheric concentration (Table 7.1) and measured ice nucleation ability (Figure 7.14) are also low chlorite was not included in the modelling.

The mineralogy of modelled atmospheric dust is compared with observations (Table 7.1) in Figure 7.19B. The modelled mineralogy is close to the observations, especially for quartz and kaolinite. The amount of feldspar in the model is approximately double that of the observations. In Figure 7.19D the feldspar mass fraction can be seen to reduce with distance from source. This spatial trend is because in the model a large proportion of feldspar is in the larger size bins, which have higher deposition rates than the smaller size bins, resulting in the preferential loss of feldspar relative to the clay minerals which are only included in the model at smaller sizes. Also, as noted above nucleation scavenging was not active in the model, and as feldspar is an efficient ice nuclei in the real atmosphere its deposition rate may be fast. There were also discrepancies in the amount of illite and montmorillonite; however the sum of these two minerals matched well between the model and observations.

7.4.1.2. Dust emission scheme

The dust emission scheme used in GLOMAP is the AeroCom scheme specified by Dentener *et al.*[201]. This scheme provides the monthly dust emission in g m^{-2} at a 1 degree resolution (Figure 7.20). The primary dust sources within the scheme are the deserts of Northern Africa, the Middle East and Central Asia, with less intense sources from deserts in North America and the southern hemisphere. The seasonal variation, while present, is not strong and there is also no emission from non-arid regions, for example due to farming activity[158] or glacial regions[162].

The dust mass and number concentrations resulting from the use of this scheme is shown in Figure 7.19A and C. The highest dust concentrations are at source regions and locations down-wind, such as in the easterly flow out of North Africa and the westerly flow from China. In comparison to the dust concentrations measured by the University of Miami (see Woodward 2001[168]), the model results are higher than observations, especially in regions of lower dust concentration. The modelled results are also approximately a factor of five higher than previously modelled results (Mann *et al.*[171], Figure 7.4), suggesting that rather than the emission scheme and modelled meteorology this discrepancy is caused by the absence of nucleation scavenging processes.

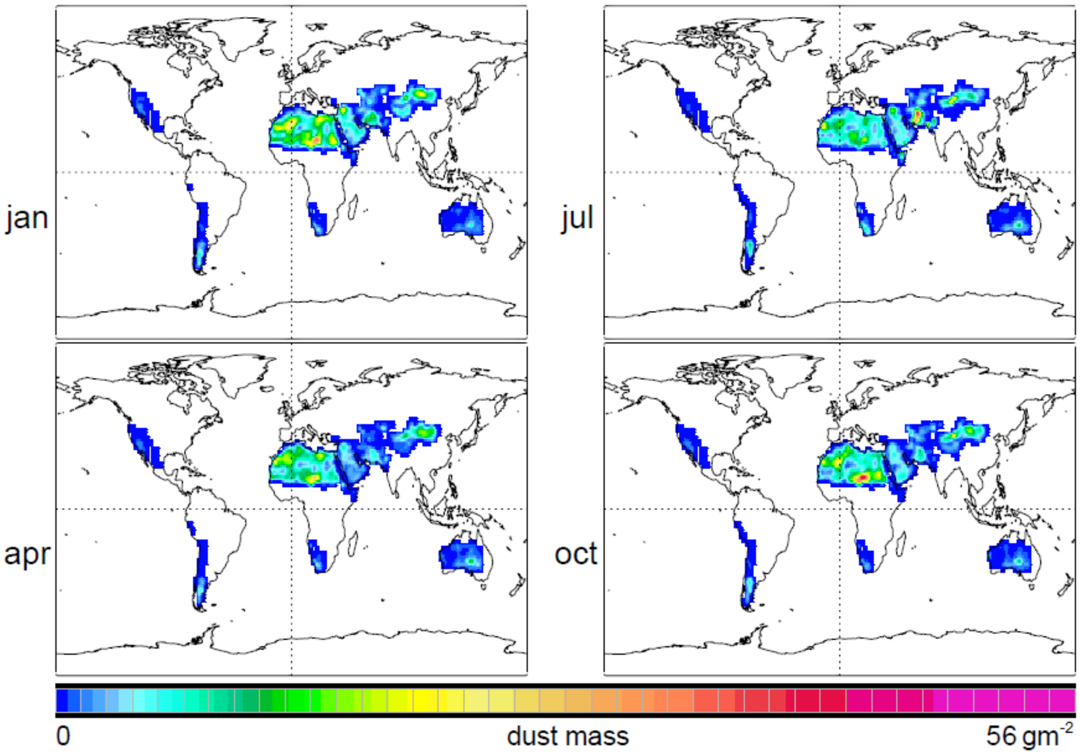

Figure 7.20. Global monthly dust emission rates for the months of January, April, July and October from the AeroCom scheme, in g m^{-2} per month. Taken from Dentener *et al.* [201].

7.4.2. Results and discussion

Knowledge of the dust number concentration, size distribution and mineralogy (Figure 7.19C and D) enables the estimation of the expected number of ice nuclei. It is assumed that the mineral dust is externally mixed and spherical. For each model grid-cell Equation 7.2 is used to combine the K-feldspar concentration and size distribution with the parameterisation of n_s for K-feldspar (Figure 7.17) to calculate the concentration of active ice nuclei expected. Figure 7.21A and B show the horizontal and vertical distribution of the estimated ice nuclei concentration at 253 K.

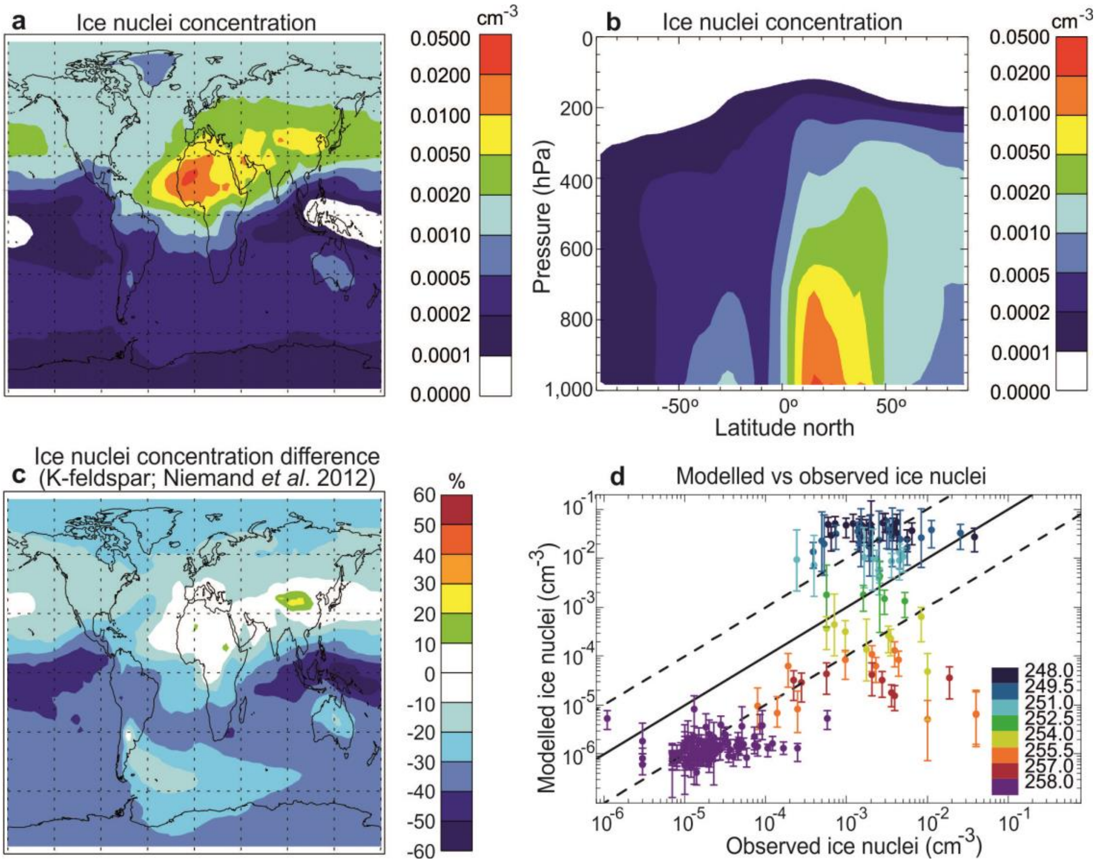

Figure 7.21. Dust aerosol modelling study results. A) Ice nuclei concentration due to K-feldspar at 253 K and 600 hPa, calculated using the n_s parameterisation from Figure 7.17 and modelled particle surface areas. B) Latitudinal zonal mean values of ice nuclei from A). C) Comparison of A) versus ice nuclei concentrations calculated at 253 K and 600 hPa using a mineralogy independent parameterisation by Niemand *et al.*[37] based on desert dust samples. Negative numbers mean the Niemand *et al.*[37] parameterisation predicts a higher concentration. D) Comparison of modelled K-feldspar ice nuclei concentrations with field measurements of total ice nuclei. Modelled concentrations are for the same pressure level as the observation, with the observation temperature used to calculate n_s. Only observations between 248 K and 258.15 K are shown, see Figure 7.23 for higher temperatures. Vertical error bars represent the maximum and minimum modelled monthly mean values. See Table 7.6 for field campaign details.

The model data clearly shows larger ice nuclei concentrations close to the major dust sources in North Africa and Asia, with concentrations three orders of magnitude lower in the regions furthest down-wind from the sources (i.e. the western and central Pacific). When comparing similar latitudes the predicted dust ice nuclei concentrations in the northern hemisphere are 1-2 orders of magnitude larger than the southern hemisphere.

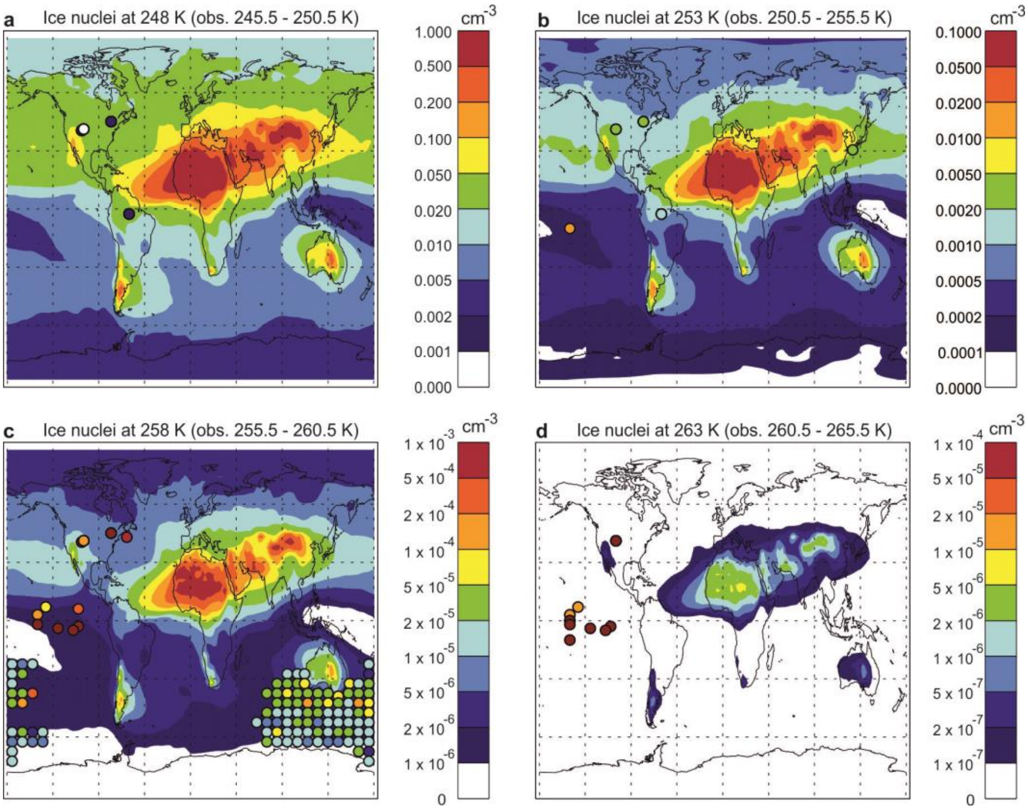

Figure 7.22. Spatial comparison of model feldspar ice nuclei concentration with field data. The model ice nuclei concentrations are for the specific temperatures shown, whereas the field ice nuclei measurements indicated by coloured circles are for the range of temperatures as specified in each plot. See Table 7.6 for details of the observations.

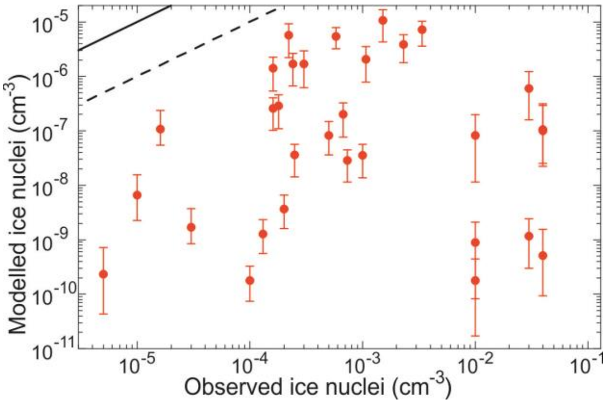

Figure 7.23. Comparison of modelled K-feldspar ice nuclei concentrations with observations at temperatures above 258 K. A 1:1 line (solid) and 10:1 line (dashed) are also shown. Vertical error bars show the range of modelled monthly mean values. See Table 7.6 for field campaign details.

This is consistent with observations of stratiform clouds in the southern hemisphere, which have been found to typically glaciate at lower temperatures[102,204,205], potentially due to this lower concentration of ice nuclei than in the northern hemisphere. These trends are largely consistent through a range of temperatures (Figure 7.22).

To investigate the importance of dust mineralogy for modelling ice nuclei, ice nuclei concentrations in Figure 7.21A were compared with those predicted by a parameterisation for natural dusts sampled from arid source regions from Niemand *et al.*[37]. The mineralogy of these dusts was not reported. Therefore, ice nuclei concentrations from this parameterisation were calculated using the total dust concentration rather than the feldspar concentration. The two parameterisations are in agreement close to dust sources (Figure 7.21C). This is consistent with the locations the dust samples used by Niemand *et al.*[37] were collected from.

However, the natural dust parameterisation predicts ice nuclei concentrations up to 60 % higher in regions remote from sources. This is because feldspar is more common in the larger particle size fractions (>2 μm) and therefore sediments out more rapidly than the minerals in the small size bins (Figure 7.19D), changing the mineralogy of the dust during transport. As a consequence, atmospheric mineral dust becomes less efficient at nucleating ice during transport through a non-chemical ageing process.

Campaign	Location	Lat.	Long.	Altitude (hPa)	T(K)	No. obs	Measurement technique
Amaze-08[115]	Brazil	-2.595	-60.209	Surface	241–255	63	CFDC
Bigg 73[206]	S. of Australia	-20 – -75	-70 – +140	Surface	258	102	Filter
Clex[115]	E. Canada	+45	-78	450–920	238–259	60	CFDC
Ice-L[115]	C. USA	+41.1	-104.8	385–724	238–252	32	CFDC
Inspect I[115]	C. USA	+40.455	-106.744	Surface	239–246	13	CFDC
Inspect II[115]	C. USA	+40.455	-106.744	Surface	241–258	11	CFDC
Rosinski 87[207]	C. Pacific	+7 – -10	-110 – +150	Surface	254–270	33	Filter
Rosinski 95[208]	E. China Sea	+30.5	+127.5	Surface	253	1	Filter
Schnell 77[209]	E. Canada	+43	-62.5	Surface	258	2	Filter
Wisp 94[115]	C. USA	+41.1	-104.8	340–880	254–264	20	CFDC

Table 7.6. Summary of ice nuclei observational campaigns. The temperatures reported are the aerosol processing temperatures rather than the ambient temperature at the sampling location. Only measurements at or above water saturation are shown.

GLOMAP mineral dust ice nuclei concentrations are also compared with field measurements of ice nuclei concentrations (where the aerosol processing temperature was below 258 K) from around the world in Figure 7.21D and 7.23. The data are scattered around the 1:1 line, suggesting that feldspar is one of the most important ice nuclei active in the Earth's atmosphere at below 258 K. The model tends to over-predict ice nuclei concentrations at temperatures below ~249 K, possibly because of the over-predicted dust concentrations due to deactivation of nucleation scavenging processes within the model. Additionally, the cluster of data at 258 K, from a ship-borne study in the oceans around southern Australia[206] (see Figure 7.22C), is consistently below the 1:1 line. This suggests that in addition to mineral dust other ice nuclei sources are important in this region. At temperatures warmer than 258 K, feldspar mineral dust is much less important as an ice nuclei and is unable to account for the observed ice nuclei concentrations (Figure 7.23). This result implies that at these warmer temperatures other ice nuclei types, possibly of biogenic origin[210], become increasingly important.

7.5.The implications of feldspar ice nucleation

In comparison with the literature, the results presented here may explain discrepancies in existing experimental data for ice nucleation by mineral dusts (Figure 7.24). Mineralogy determined by XRD for examples of a number of the mineral dusts used in the literature has shown the presence of feldspar (Table 7.7) . The dusts are: K-SA, a kaolinite provided by Fluka/Sigma Aldrich used by Lüönd *et al.*[42] and Pinti *et al.*[40], and four montmorillonites: M KSF supplied by Sigma Aldrich, M K-10 from Alfa Aesar and M SWy-2 supplied by the Clay Mineral Society (all used by Pinti *et al.*[40]) and M APC, a montmorillonite treated by aluminium pillaring and supplied by Sigma Aldrich, which was examined by Conen *et al.*[114]. Other mineral dusts from the literature is shown for comparison – KGa-1b[41], ATD[37,80,109,139,191,192] and NX illite[40,47] provided by Murray *et al.*[30].

Figure 7.24 is an updated version of Figure 7.13, with green centres denoting mineral dusts which were found to contain feldspar. The mixed natural dusts used by Pinti *et al.*[40] and Niemand *et al.*[37] have unknown mineralogy but likely contain feldspar due its ubiquitous nature[163]. In general, the more K-feldspar a mineral sample contains the higher the nucleation coefficient and/or freezing temperature. For example, of the literature mineral samples ATD has the highest measured K-feldspar content (20.3 %) and high n_s values, followed by kaolinite (K SA), the illites and the montmorillonites. All of the data above the quartz parameterisation (black dot-dashed) contains feldspar, as does the high temperature montmorillonite work by Conen *et al.*[114]. This highlights the need to characterise sample mineralogy in ice nucleation work.

Notable exceptions to this generalisation are two montmorillonites tested by Pinti *et al.*[40] (M KSF and M K-10), which both produced relatively low nucleation coefficients. Both of these samples, as well as the one used by Conen *et al.*[114], were acid washed by the manufacturer, which may have affected the surface of any feldspar particles present (see section 7.2.2.2).

The high nucleation coefficient of the montmorillonite used by Pitter and Pruppacher[39] implies it contained feldspar. However extrapolation of the kaolinite[41] and quartz parameterisations suggests the Pitter and Pruppacher[39] kaolinite result could be due to either of these minerals. The measurements by Hoffer[38] are consistent with the nucleation coefficients measured during this work. However, the lack of surface area data from both Hoffer[38] and Pitter and Pruppacher[39] makes it difficult to conclude with any certainty. For example if the montmorillonite used by Hoffer had a low surface area then it is more likely that nucleation was caused by contamination.

Mineral Sample	IL/MI	KA	MM	CH	QU	NCF	KF	CA	Others
K-SA	5.4	82.7	ND	ND	5.9	0.4	4.5	0.3	Dolomite 0.5 unidentified 0.2
KA	ND	96	ND	ND	ND	ND	ND	ND	Anatase 3 crandallite 1
M KSF	10.3	3.3	57.0	ND	4.3	1.6	1.7	0.9	Illite-smectite 18.3 barite 1.3 anatase 1.2
M K-10	17.6	ND	40.1	ND	10.5	6.5	3.2	ND	Illite-smectite 20.6 zincite 0.9 halite 0.5
M SWy-2†	<1	<1	75	<1	8	16 (combined)†		ND	Gypsum 1.0
M APC	ND	ND	<93.3	ND	1.4	2.0	3.2	ND	Unidentified <93.3
ATD	7.5	2.0	ND	ND	17.1	12.4	20.3	4.3	Illite-smectite 10.1 dolomite 1.3 hematite 0.7 unidentified 25.0
NX Illite	60.5	7.2	ND	ND	6.6	1.7	8.1	2.1	Illite-smectite 13.8

Table 7.7. Mineralogies of several mineral dusts used in the literature. The proportion of each mineral is expressed in weight per cent, mineral abbreviations as per Table 7.1. Mineral compositions were produced using XRD (see Section 5.1) by Dr T.L. Malkin. ND – not detected except: †: data from Chipera and Bish[193], who provided total feldspar rather than K-feldspar and Na/Ca-feldspar separately.

These results may also help understand the chemical ageing process of dust ice nuclei, which is known to reduce the ice nucleating efficiency of dust[191,211]. As discussed previously (Section 7.2.2.2) in an acidic environment the surface of feldspar grains can be converted into clay minerals. This suggests that gases which can be converted to acids in the atmosphere, such as SO_2, may reduce the surface area available for nucleation and reduce the efficiency of feldspar as an ice nucleus. This provides an explanation for the observed sensitivity of mineral dust ice nuclei to acid processing[191,211].

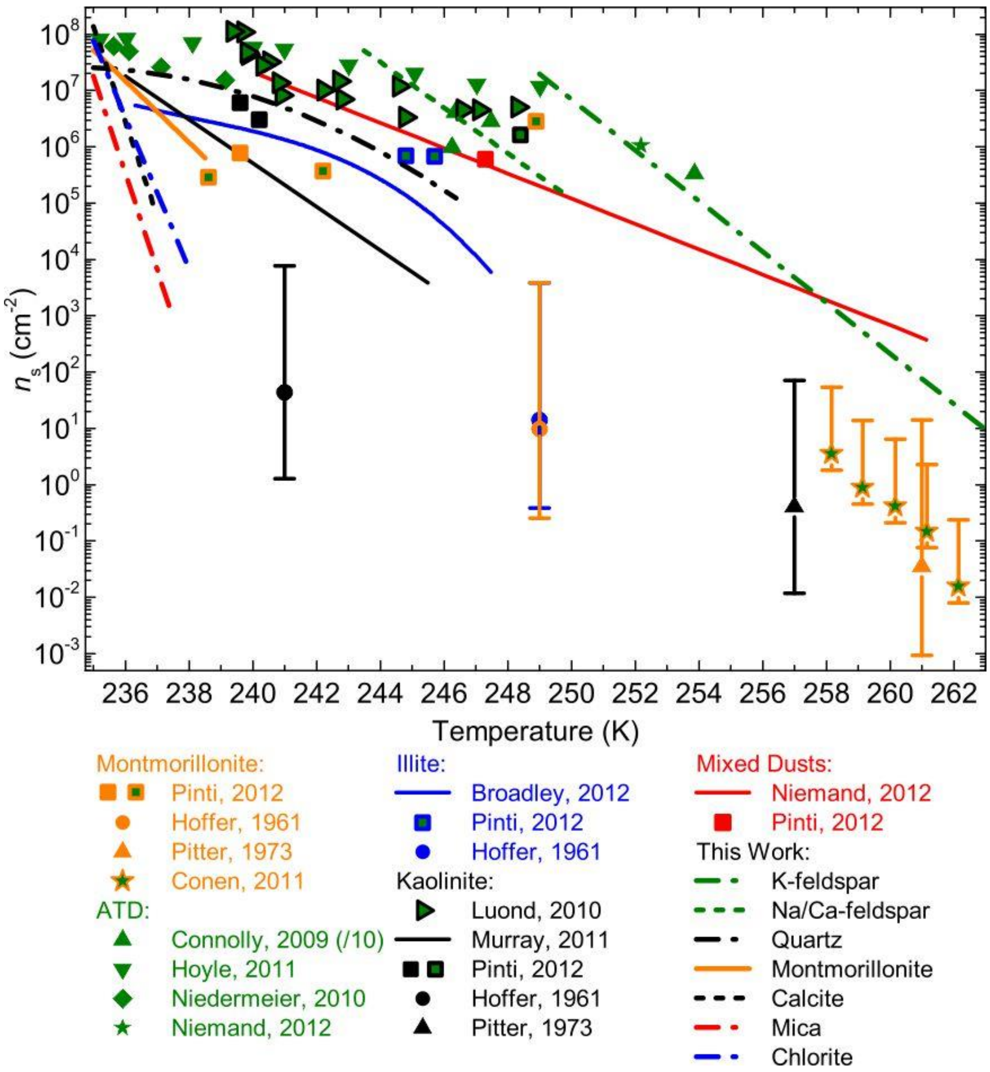

Figure 7.24. Nucleation coefficients from this study in comparison with literature values. Fits to the n_s values from Figure 7.14B are shown. Literature data[37-42,47,80,109,114,139] which has been shown to contain feldspar is displayed with a green centre. The illite used by Broadley *et al*.[47] also contained feldspar. The composition of the minerals used by Hoffer[38], Pitter and Pruppacher[39] and the mixed dusts used by Niemand *et al*.[37] and Pinti *et al*.[40] is unknown.

Finally, recent work suggests human activity has led to a substantial increase in atmospheric dust concentrations and that the source locations of this dust have changed[158,212]. For example, anthropogenic dust emissions have been estimated to be responsible for ~23 % of the total atmospheric dust burden[158]. The principle source regions for this anthropogenic dust are Northern India, Southeastern Australia, Central USA, Argentina, Kazakhstan and the Saharan margins in Africa (e.g. Figure 16 of ref [158]). Since potential dust sources around the world have very different feldspar contents[196], these and future changes may have consequences for the concentration of ice nuclei in the atmosphere and the associated aerosol indirect effect.

7.6. Summary and conclusions

The ice nucleating abilities of seven of the most atmospherically common minerals have been determined. The samples of these minerals have had their bulk mineralogy identified, and compliment the work on the well characterised kaolinite already in the literature[41]. This new data has shown that the feldspars are the most efficient of the common minerals. The n_s values presented here suggest that per unit surface area K-feldspar is two orders of magnitude more efficient than Na/Ca-feldspar and in the region of four orders of magnitude more efficient than kaolinite. This implies that the answer to the third project objective is that K-feldspar dominates ice nucleation by mineral dusts.

The feldspars and quartz are major components of igneous rocks and as such are found in most soils and sedimentary rock types. This makes the acquisition of samples of other minerals which are free of these more efficient ice nuclei difficult, and can explain the variations between, and high activity of, some of the literature ice nucleation data. It is strongly recommended that in all future work the mineralogy of dust samples is determined as standard.

The atmospheric importance of feldspar has been confirmed by comparisons using globally averaged dust compositions and concentrations as well as a modelling study. The modelling work has shown that, although feldspar is predominantly present in the larger dust size fractions it is present globally. Maximum contributions to the dust mass are near source regions and minimum contributions furthest down-wind from sources, with a similar trend to the expected concentration of ice nuclei. Comparison with a mineralogy-independent ice nucleation parameterisation, the change in feldspar contribution to the dust mass results in an over-estimation in expected ice nuclei concentrations of up to around a factor of three.

The modelling was performed without wet-deposition processes, the impact of which should be looked at in future work. The lack of these processes may result in an over-estimation of the total dust and feldspar concentrations. However as these processes occur over time, the impact is likely strongest at locations far from sources, where Figure 7.22 implies that dust is not the most important ice nuclei. In the future, satellite observations may be able to directly observe feldspar in the atmosphere (e.g. ref [213]), which would enable the validation of such modelling work.

It is now known which of the major components of atmospheric mineral dust is the most active as an ice nuclei. It has been suggested that a match in the crystal structure between the ice nuclei and growing ice cluster is a characteristic of an effective ice nuclei[9,214-216]. The crystal structure of K-feldspar and Na/Ca-feldspar are similar and very different from those of the clay minerals. Experiments to determine if nucleation occurs at a specific location or crystal face[217], and also molecular dynamics simulations[218], may provide some new insights into the fundamental process of ice nucleation. This new knowledge will also allow better focus in experiments studying factors such as the chemical ageing of ice nuclei (e.g. refs [211]).

Chapter 8. Summary and conclusions

In this project the ice nucleating behaviour of particles relevant to mixed-phase tropospheric clouds has been investigated. Mixed-phase clouds are thought to produce a large proportion of global precipitation. Clouds and precipitation are part of the hydrological cycle, and the prediction of rainfall amounts and intensities is of vital importance to various sectors of society. They are important for the Earth's radiation budget and their size and lifetime is sensitive to the concentration of ice crystals in them. The addition of aerosol particles, referred to as ice nuclei, to a cloud can catalyse the formation of ice. This study took place in three main steps. Firstly, to develop a laboratory instrument capable of investigating ice nucleation by pure water droplets and droplets containing atmospherically relevant particles. Secondly, to study the ice nucleating ability of pure water to determine if nucleation due to the droplet surface occurs at significant rates, and thirdly to investigate the ice nucleating abilities of atmospherically relevant mineral dusts.

8.1. Development of a laboratory experiment for studying ice nucleation

A new instrument was constructed to investigate the nucleation of ice in liquid water, based upon a cold stage droplet freezing assay. Water droplets containing suspended mineral particles were deposited on a hydrophobic glass surface and then cooled to freezing temperatures using a cold stage. The new stage is more reliable in comparison to previous designs, with an estimated temperature uncertainty of ±0.3 K in a 1 K min^{-1} cooling experiment. Simplifications to the experimental process have made experiments faster and more repeatable.

The statistical processes which need to be undertaken after a freezing experiment to produce ice nucleation coefficients have been described. The relationship between the size distribution of droplets and the nucleation coefficient has been investigated. The method used to represent the average liquid droplet volume in an experiment can have a large impact upon the calculated coefficient. A framework has been described for ensuring that the method used does not have a significant impact upon the calculated nucleation coefficients.

8.2.Homogeneous nucleation

The existence of nucleation at the surface of a pure water droplet was hypothesised by Tabazadeh *et al.*[44,150] in 2002 using laboratory measurements, and described theoretically in 2003[83,151]. As the surface to volume ratio of a droplet changes with the droplet diameter, nucleation due to the droplet surface is thought to be equal to that due to the volume only for small droplets[46] – no bigger than ~4 µm radius at 237.1 K[77]. This finding was supported by Kuhn *et al.*[86], who measured the nucleation rates of droplets <6 µm radius and determined that the radius of surface-volume equivalence was 5.1 µm at 235.5 K.

Parameterisations of the nucleation rate coefficients for both the surface and volume of pure water droplets were derived for temperatures between 234.4 and 236.2 K. Droplet freezing due to volume nucleation represented the data well, but nucleation was best described by the combination of the droplet surface and volume. The derived volume nucleation rate coefficient ($\ln(J_V) = -3.7000T + 888.78$) is in good agreement with the literature, especially with Riechers *et al.*[28], Lüönd *et al.*[42] and Hoyle *et al.*[80]. The reported surface nucleation rate coefficient ($\ln(J_S) = -4.8956T + 1159.63$) is in agreement with Kuhn *et al.*[86]. These parameterisations suggest that surface nucleation can be neglected for droplets >~5 µm radius. This is consistent with limitations to surface nucleation within the literature[44,77], and includes a large proportion of observed cloud liquid droplet sizes[153,154]. For much smaller droplets the effect of surface nucleation is significant, with a 0.5 K lower predicted freezing temperature for 1 µm diameter droplets without surface nucleation. If the data is stressed, the change in freezing temperature due to surface nucleation can be calculated for a 100 nm diameter droplet and is ~1.5 K.

8.3.Ice nucleation by mineral dusts in the immersion mode

Atmospheric mineral dusts are an important class of ice nuclei. However, of the eight minerals most common to the atmosphere, only one has reported ice nucleating ability and mineralogical details. In the literature the nucleating coefficients for different minerals range over many orders of magnitude and tens of degrees kelvin, with no clear trends between individual mineral types.

Examples of seven of the most atmospherically common minerals have had their bulk mineralogy and ice nucleating abilities determined. Evidence of a wide range of ice nucleating abilities was found. Counter to the prevailing view that the clays are the main mineral dust ice nuclei in the atmosphere (e.g. refs [30,31]), the derived nucleation coefficient for K-feldspar was orders of magnitude higher than the other minerals. This result implies that K-feldspar dominates ice nucleation by mineral dusts.

The K-feldspar data has big implications for the analysis of mineral ice nuclei, both past and present. Feldspar is a major component of igneous rocks[148] and is found in most soils and most rock formations from which clay mineral samples are often sourced[163]. This can make acquiring feldspar-free samples of some minerals difficult, especially illite (e.g. Table 7.3), and could explain the differences between mineral samples in the literature.

K-feldspar is relatively uncommon in the atmosphere, contributing on average only 3 % to the atmospheric mineral dust mass. A global chemical and aerosol transport modelling study has been combined with a surface mineralogy database to estimate the concentration of K-feldspar in the atmosphere. In comparison with field observations of total atmospheric dust, the model simulation estimates are within about a factor of two, and the predicted feldspar mass fractions are within a factor of four of the observations. These results were combined with the parameterisation for ice nucleation by immersed K-feldspar to estimate the concentration of ice nuclei active at a range of temperatures.

Annually averaged K-feldspar ice nuclei concentrations range from as high as 1 cm^{-3} in Northern Africa at 248 K, to less than 1×10^{-7} cm^{-3} in most areas of the globe at 263 K. Concentrations are at a maximum near the dust source regions (North Africa, Southern and Western Asia), and at a minimum in the locations furthest down-wind from these locations (the Western and Southern Pacific Ocean). In comparison to field observations of ice nuclei concentrations, it was found that K-feldspar ice nuclei are sufficient to explain the observations at below ~255 K. At temperatures much lower than this the predicted K-feldspar ice nuclei concentration is too high, suggesting the removal of dust from the model is too slow. At higher temperatures ice nucleation by K-feldspar is insufficient to explain the observations, suggesting another source of efficient ice nuclei is required.

In the future global models could predict the concentration of ice nuclei due to K-feldspar. For example, the global circulation model developed by the Monitoring Atmospheric Composition and Climate project[219] is capable of forecasting the concentration of dust in the atmosphere (e.g. Figure 8.1). If this model was updated to include tracers for the individual minerals characterised it would be capable of predicting the concentration of mineral dust ice nuclei. Satellite observations of dust mineralogy are currently being developed[213], and could be used to initialise and validate such a model.

It is now known which major component of atmospheric mineral dust is the most active ice nuclei. This presents interesting questions for future investigation. For example, experiments to investigate the chemical ageing of ice nuclei can now focus upon feldspar. Feldspar slowly dissolves in acids, which alters any exposed crystal surfaces[188,220]. The time and pH required to alter feldspar sufficiently to affect its ice nucleating ability is poorly constrained, as such experiments have concentrated on mixed mineral samples which may contain buffers[191,211]. Additionally, feldspar dissolution rates are faster in the presence of organic acids[189].

K-feldspar also represents an avenue of investigation into the fundamental ice nucleation process. Ice nucleation has been suggested to occur due to a match between the crystal structure of the mineral particle and the growing ice cluster[9,214-216]. However, K-feldspar is a more efficient ice nucleus than Na/Ca-feldspar which has a similar structure. Additionally, muscovite mica has a similar elemental composition to K-feldspar but a much lower ice nucleating efficiency. Molecular dynamics simulations[218] and experiments to determine why K-feldspar is more effective and if nucleation occurs at a specific location or crystal face[217] may give further insights into ice nucleation.

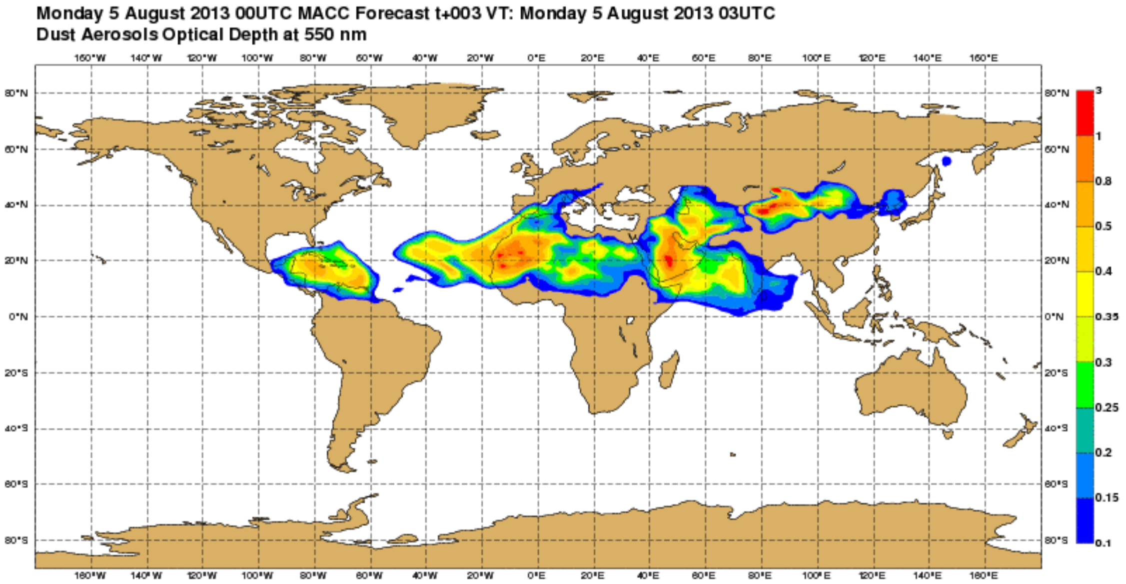

Figure 8.1. Example model prediction of column dust aerosol optical depth. Predicted as part of the Monitoring Atmospheric Composition and Climate project[219].

Appendix – LabVIEW video recording program

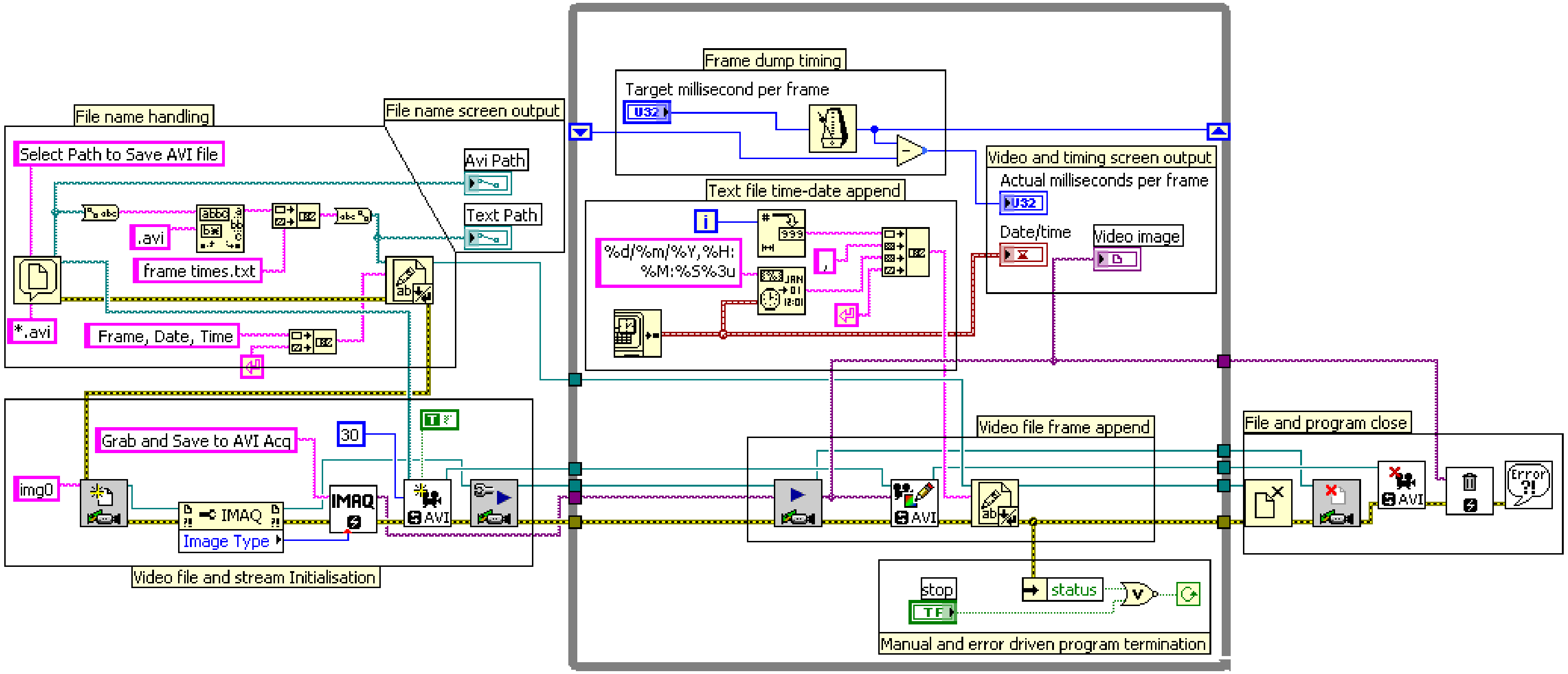

Program written in the LabVIEW environment to simultaneously retrieve images from the digital camera and record the frame time. The section to the left of the thick grey bordered box is responsible for initialising the connection to the camera and creating the video and text files. The section in the grey box is a loop while writing frames and timings to the files and providing on screen output until the program fails or is stopped. The small section to the right of the box finalises and closes the files, terminates the connection to the camera and outputs any system errors to screen.

References

1. Agnew, M.D. and J.E. Thornes, *The weather sensitivity of the UK food retail and distribution industry.* Meteorological Applications, 1995. **2**(2): p. 137-147, doi: 10.1002/met.5060020207.
2. Challinor, A.J., F. Ewert, S. Arnold, E. Simelton, and E. Fraser, *Crops and climate change: progress, trends, and challenges in simulating impacts and informing adaptation.* Journal of Experimental Botany, 2009. **60**(10): p. 2775-2789, doi: 10.1093/jxb/erp062.
3. Changnon, S.A., D. Changnon, E.R. Fosse, D.C. Hoganson, R.J. Roth, and J.M. Totsch, *Effects of Recent Weather Extremes on the Insurance Industry: Major Implications for the Atmospheric Sciences.* Bulletin of the American Meteorological Society, 1997. **78**(3): p. 425-435, doi: 10.1175/1520-0477(1997)078<0425:eorweo>2.0.co;2.
4. Roulston, M.S., D.T. Kaplan, J. Hardenberg, and L.A. Smith, *Using medium-range weather forcasts to improve the value of wind energy production.* Renewable Energy, 2003. **28**(4): p. 585-602, doi: 10.1016/S0960-1481(02)00054-X.
5. Haile, M., *Weather patterns, food security and humanitarian response in sub-Saharan Africa.* Philosophical Transactions of the Royal Society B: Biological Sciences, 2005. **360**(1463): p. 2169-2182, doi: 10.1098/rstb.2005.1746.
6. Barry, R.G. and R.J. Chorley, *Atmosphere, Weather and Climate*. 8th ed., 2003, London: Routledge.
7. Trenberth, K. and J. Fasullo, *Tracking Earth’s Energy: From El Niño to Global Warming.* Surveys in Geophysics, 2012. **33**(3): p. 413-426, doi: 10.1007/s10712-011-9150-2.
8. Forster, P., V. Ramaswamy, P. Artaxo, T. Berntsen, R. Betts, D.W. Fahey, J. Haywood, J. Lean, D.C. Lowe, G. Myhre, J. Nganga, R. Prinn, G. Raga, M. Schulz and R. Van Dorland, *Changes in Atmospheric Constituents and in Radiative Forcing.*, in *Climate Change 2007: The Physical Science Basis. Contribution of Working Group I to the Fourth Assessment Report of the Intergovernmental Panel on Climate Change*, S. Solomon, D. Qin, M. Manning, Z. Chen, M. Marquis, K.B. Averyt, M.Tignor and H.L. Miller, Editor 2007: Cambridge, United Kingdom.
9. Pruppacher, H.R. and J.D. Klett, *Microphysics of Clouds and Precipitation*. 2nd ed., 1997: Kluwer Academic Publishers.
10. Ramanathan, V., R.D. Cess, E.F. Harrison, P. Minnis, B.R. Barkstrom, E. Ahmad, and D. Hartmann, *Cloud-Radiative Forcing and Climate: Results from the Earth Radiation Budget Experiment.* Science, 1989. **243**(4887): p. 57-63, doi: 10.1126/science.1064034.
11. Hartmann, D.L., M.E. Ockert-Bell, and M.L. Michelsen, *The Effect of Cloud Type on Earth's Energy Balance: Global Analysis.* Journal of Climate, 1992. **5**(11): p. 1281-1304, doi: 10.1175/1520-0442(1992)005<1281:teocto>2.0.co;2.
12. Chahine, M.T., *The hydrological cycle and its influence on climate.* Nature, 1992. **359**(6394): p. 373-380, doi: 10.1038/359373a0.
13. Twomey, S., *Pollution and the planetary albedo.* Atmospheric Environment, 1974. **8**(12): p. 1251-1256, doi: 10.1016/0004-6981(74)90004-3.
14. Lohmann, U. and J. Feichter, *Global indirect aerosol effects: a review.* Atmospheric Chemistry and Physics, 2005. **5**: p. 715-737, doi: 10.5194/acp-5-715-2005.

15. Lin, B., P. Minnis, and A. Fan, *Cloud liquid water path variations with temperature observed during the Surface Heat Budget of the Arctic Ocean (SHEBA) experiment.* Journal of Geophysical Research: Atmospheres, 2003. **108**(D14): p. 4427, doi: 10.1029/2002jd002851.
16. Boucher, O. and U. Lohmann, *The sulfate-CCN-cloud albedo effect.* Tellus B, 1995. **47**(3): p. 281-300, doi: 10.1034/j.1600-0889.47.issue3.1.x.
17. Gibson, E.R., K.M. Gierlus, P.K. Hudson, and V.H. Grassian, *Generation of Internally Mixed Insoluble and Soluble Aerosol Particles to Investigate the Impact of Atmospheric Aging and Heterogeneous Processing on the CCN Activity of Mineral Dust Aerosol.* Aerosol Science and Technology, 2007. **41**(10): p. 914-924, doi: 10.1080/02786820701557222.
18. Koehler, K.A., S.M. Kreidenweis, P.J. DeMott, M.D. Petters, A.J. Prenni, and C.M. Carrico, *Hygroscopicity and cloud droplet activation of mineral dust aerosol.* Geophys. Res. Lett., 2009. **36**(8): p. L08805, doi: 10.1029/2009gl037348.
19. Keil, A. and J.M. Haywood, *Solar radiative forcing by biomass burning aerosol particles during SAFARI 2000: A case study based on measured aerosol and cloud properties.* Journal of Geophysical Research: Atmospheres, 2003. **108**(D13): p. 8467, doi: 10.1029/2002jd002315.
20. Pierce, J.R. and P.J. Adams, *Global evaluation of CCN formation by direct emission of sea salt and growth of ultrafine sea salt.* Journal of Geophysical Research: Atmospheres, 2006. **111**(D6): p. D06203, doi: 10.1029/2005jd006186.
21. Schmidt, A., K.S. Carslaw, G.W. Mann, A. Rap, K.J. Pringle, D.V. Spracklen, M. Wilson, and P.M. Forster, *Importance of tropospheric volcanic aerosol for indirect radiative forcing of climate.* Atmos. Chem. Phys., 2012. **12**(16): p. 7321-7339, doi: 10.5194/acp-12-7321-2012.
22. Sun, J. and P.A. Ariya, *Atmospheric organic and bio-aerosols as cloud condensation nuclei (CCN): A review.* Atmospheric Environment, 2006. **40**(5): p. 795-820, doi: 10.1016/j.atmosenv.2005.05.052.
23. Albrecht, B.A., *Aerosols, Cloud Microphysics, and Fractional Cloudiness.* Science, 1989. **245**(4923): p. 1227-1230, doi: 10.1126/science.245.4923.1227.
24. Booth, B.B.B., N.J. Dunstone, P.R. Halloran, T. Andrews, and N. Bellouin, *Aerosols implicated as a prime driver of twentieth-century North Atlantic climate variability.* Nature, 2012. **484**(7393): p. 228-232, doi: 10.1038/nature10946.
25. Lohmann, U., *A glaciation indirect aerosol effect caused by soot aerosols.* Geophys. Res. Lett., 2002. **29**(4), doi: 10.1029/2001GL014357.
26. Brenguier, J.-L., T. Bourrianne, A.A. Coelho, J. Isbert, R. Peytavi, D. Trevarin, and P. Weschler, *Improvements of Droplet Size Distribution Measurements with the Fast-FSSP (Forward Scattering Spectrometer Probe).* Journal of Atmospheric and Oceanic Technology, 1998. **15**(5): p. 1077-1090, doi: 10.1175/1520-0426(1998)015<1077:iodsdm>2.0.co;2.
27. Rosenfeld, D. and W.L. Woodley, *Deep convective clouds with sustained supercooled liquid water down to -37.5 °C.* Nature, 2000. **405**(6785): p. 440-442, doi: 10.1038/35013030.
28. Riechers, B., F. Wittbracht, A. Hütten, and T. Koop, *The homogeneous ice nucleation rate of water droplets produced in a microfluidic device and the role of temperature uncertainty.* Physical Chemistry Chemical Physics, 2013. **15**: p. 5873-5887, doi: 10.1039/C3CP42437E.
29. Murray, B.J., S.L. Broadley, T.W. Wilson, S.J. Bull, R.H. Wills, H.K. Christenson, and E.J. Murray, *Kinetics of the homogeneous freezing of water.* Physical Chemistry Chemical Physics, 2010. **12**(35): p. 10380-10387, doi: 10.1039/c003297b.

30. Murray, B.J., D. O'Sullivan, J.D. Atkinson, and M.E. Webb, *Ice nucleation by particles immersed in supercooled cloud droplets.* Chemical Society Reviews, 2012. **41**: p. 6519-6554, doi: 10.1039/C2CS35200A.
31. Hoose, C. and O. Möhler, *Heterogeneous ice nucleation on atmospheric aerosols: a review of results from laboratory experiments.* Atmos. Chem. Phys., 2012. **12**(20): p. 9817-9854, doi: 10.5194/acp-12-9817-2012.
32. Korolev, A., *Limitations of the Wegener–Bergeron–Findeisen Mechanism in the Evolution of Mixed-Phase Clouds.* Journal of the Atmospheric Sciences, 2007. **64**(9): p. 3372-3375, doi: 10.1175/jas4035.1.
33. Pratt, K.A., P.J. DeMott, J.R. French, Z. Wang, D.L. Westphal, A.J. Heymsfield, C.H. Twohy, A.J. Prenni, and K.A. Prather, *In situ detection of biological particles in cloud ice-crystals.* Nature Geosci, 2009. **2**(6): p. 398-401, doi: 10.1038/ngeo521.
34. Cziczo, D.J., K.D. Froyd, C. Hoose, E.J. Jensen, M. Diao, M.A. Zondlo, J.B. Smith, C.H. Twohy, and D.M. Murphy, *Clarifying the Dominant Sources and Mechanisms of Cirrus Cloud Formation.* Science, 2013. **340**(6138): p. 1320-1324, doi: 10.1126/science.1234145.
35. Prenni, A.J., M.D. Petters, S.M. Kreidenweis, C.L. Heald, S.T. Martin, P. Artaxo, R.M. Garland, A.G. Wollny, and U. Poschl, *Relative roles of biogenic emissions and Saharan dust as ice nuclei in the Amazon basin.* Nature Geosci, 2009. **2**(6): p. 402-405, doi: 10.1038/NGEO517.
36. Richardson, M.S., P.J. DeMott, S.M. Kreidenweis, D.J. Cziczo, E.J. Dunlea, J.L. Jimenez, D.S. Thomson, L.L. Ashbaugh, R.D. Borys, D.L. Westphal, G.S. Casuccio, and T.L. Lersch, *Measurements of heterogeneous ice nuclei in the western United States in springtime and their relation to aerosol characteristics.* Journal of Geophysical Research, 2007. **112**(D2), doi: 10.1029/2006JD007500.
37. Niemand, M., O. Möhler, B. Vogel, H. Vogel, C. Hoose, P. Connolly, H. Klein, H. Bingemer, P.J. DeMott, J. Skrotzki, and T. Leisner, *A particle-surface-area-based parameterization of immersion freezing on desert dust particles.* Journal of the Atmospheric Sciences, 2012. **69**(10), doi: 10.1175/jas-d-11-0249.1.
38. Hoffer, T.E., *A laboratory investigation of droplet freezing.* Journal of Meteorology, 1961. **18**(6): p. 766-778, doi: 10.1175/1520-0469(1961)018<0766:ALIODF>2.0.CO;2.
39. Pitter, R.L. and H.R. Pruppacher, *Wind-tunnel investigation of freezing of small water drops falling at terminal velocity in air.* Quarterly Journal of the Royal Meteorological Society, 1973. **99**(421): p. 540-550, doi: 10.1002/qj.49709942111.
40. Pinti, V., C. Marcolli, B. Zobrist, C.R. Hoyle, and T. Peter, *Ice nucleation efficiency of clay minerals in the immersion mode.* Atmos. Chem. Phys., 2012. **12**(13): p. 5859-5878, doi: 10.5194/acp-12-5859-2012.
41. Murray, B.J., S.L. Broadley, T.W. Wilson, J.D. Atkinson, and R.H. Wills, *Heterogeneous freezing of water droplets containing kaolinite particles.* Atmos. Chem. Phys., 2011. **11**(9): p. 4191-4207, doi: 10.5194/acp-11-4191-2011.
42. Lüönd, F., O. Stetzer, A. Welti, and U. Lohmann, *Experimental study on the ice nucleation ability of size-selected kaolinite particles in the immersion mode.* J. Geophys. Res., 2010. **115**(D14): p. D14201, doi: 10.1029/2009jd012959.
43. Li, Z., H. Xue, and F. Yang, *A modeling study of ice formation affected by aerosols.* Journal of Geophysical Research: Atmospheres, 2013. **118**(19): p. 11213-11227, doi: 10.1002/jgrd.50861.
44. Tabazadeh, A., Y.S. Djikaev, and H. Reiss, *Surface crystallization of supercooled water in clouds.* Proceedings of the National Academy of Sciences, 2002. **99**(25): p. 15873-15878, doi: 10.1073/pnas.252640699.

45. Tabazadeh, A., *Commentary on "Homogeneous nucleation of NAD and NAT in liquid stratospheric aerosols: insufficient to explain denitrification" by Knopf et al.* Atmos. Chem. Phys., 2003. **3**: p. 863-865, doi: 10.5194/acp-3-863-2003.
46. Kay, J.E., V. Tsemekhman, B. Larson, M. Baker, and B. Swanson, *Comment on evidence for surface-initiated homogeneous nucleation.* Atmos. Chem. Phys., 2003. **3**: p. 1439-1443, doi: 10.5194/acp-3-1439-2003.
47. Broadley, S.L., B.J. Murray, R.J. Herbert, J.D. Atkinson, S. Dobbie, T.L. Malkin, E. Condliffe, and L. Neve, *Immersion mode heterogeneous ice nucleation by an illite rich powder representative of atmospheric mineral dust.* Atmos. Chem. Phys., 2012. **12**(1): p. 287-307, doi: 10.5194/acp-12-287-2012.
48. Rogers, D.C., P.J. DeMott, S.M. Kreidenweis, and Y.L. Chen, *Measurements of ice nucleating aerosols during SUCCESS.* Geophys. Res. Lett., 1998. **25**(9): p. 1383-1386, doi: 10.1029/97GL03478.
49. Lau, K.M. and H.T. Wu, *Warm rain processes over tropical oceans and climate implications.* Geophys. Res. Lett., 2003. **30**(24): p. 2290, doi: 10.1029/2003gl018567.
50. Creamean, J.M., K.J. Suski, D. Rosenfeld, A. Cazorla, P.J. DeMott, R.C. Sullivan, A.B. White, F.M. Ralph, P. Minnis, J.M. Comstock, J.M. Tomlinson, and K.A. Prather, *Dust and Biological Aerosols from the Sahara and Asia Influence Precipitation in the Western U.S.* Science, 2013. **339**(6127): p. 1572-1578, doi: 10.1126/science.1227279.
51. Murphy, D.M. and T. Koop, *Review of the vapour pressures of ice and supercooled water for atmospheric applications.* Quarterly Journal of the Royal Meteorological Society, 2005. **131**(608): p. 1539-1565, doi: 10.1256/qj.04.94.
52. List, R. and J.R. Gillespie, *Evolution of Raindrop Spectra with Collision-Induced Breakup.* Journal of the Atmospheric Sciences, 1976. **33**(10): p. 2007-2013, doi: 10.1175/1520-0469(1976)033<2007:eorswc>2.0.co;2.
53. Koop, T. and N. Mahowald, *Atmospheric science: The seeds of ice in clouds.* Nature, 2013. **498**(7454): p. 302-303, doi: 10.1038/nature12256.
54. Young, K.C., *Microphysical Processes in Clouds* 1993, Oxford, UK: Oxford University Press.
55. McFiggans, G., P. Artaxo, U. Baltensperger, H. Coe, M.C. Facchini, G. Feingold, S. Fuzzi, M. Gysel, A. Laaksonen, U. Lohmann, T.F. Mentel, D.M. Murphy, C.D. O'Dowd, J.R. Snider, and E. Weingartner, *The effect of physical and chemical aerosol properties on warm cloud droplet activation.* Atmos. Chem. Phys., 2006. **6**(9): p. 2593-2649, doi: 10.5194/acp-6-2593-2006.
56. Denman, K.L., G. Brasseur, A. Chidthaisong, P. Ciais, P.M. Cox, R.E. Dickinson, D. Hauglustaine, C. Heinze, E. Holland, D. Jacob, U. Lohmann, S. Ramachandran, P.L. da Silva Dias, S.C. Wofsy, and X. Zhang, *Couplings Between Changes in the Climate System and Biogeochemistry. In: Climate Change 2007: The Physical Science Basis. Contribution of Working Group I to the Fourth Assessment Report of the Intergovernmental Panel on Climate Change* 2007, Cambridge, United Kingdom: Cambridge University Press.
57. Mullin, J.W., *Crystallization* 2001, Oxford, UK: Elsevier.
58. Huang, J. and L.S. Bartell, *Kinetics of Homogeneous Nucleation in the Freezing of Large Water Clusters.* The Journal of Physical Chemistry, 1995. **99**(12): p. 3924-3931, doi: 10.1021/j100012a010.
59. Murphy, D.M., *Dehydration in cold clouds is enhanced by a transition from cubic to hexagonal ice.* Geophys. Res. Lett., 2003. **30**(23), doi: 10.1029/2003GL018566.

60. Tanaka, H. and I. Okabe, *Thermodynamic stability of hexagonal and cubic ices.* Chemical Physics Letters, 1996. **259**(5–6): p. 593-598, doi: 10.1016/0009-2614(96)00824-X.
61. Malkin, T.L., B.J. Murray, A.V. Brukhno, J. Anwar, and C.G. Salzmann, *Structure of ice crystallized from supercooled water.* Proceedings of the National Academy of Sciences, 2012. **109**(4): p. 1041-1045, doi: 10.1073/pnas.1113059109.
62. Pruppacher, H.R., *A New Look at Homogeneous Ice Nucleation in Supercooled Water Drops.* Journal of the Atmospheric Sciences, 1995. **52**(11): p. 1924-1933, doi: 10.1175/1520-0469(1995)052<1924:ANLAHI>2.0.CO;2.
63. Hallett, J., *The Temperature Dependence of the Viscosity of Supercooled Water.* Proceedings of the Physical Society, 1963. **82**(6): p. 1046, doi: 10.1088/0370-1328/82/6/326.
64. *CRC Handbook of Chemistry and Physics*. 88th ed., 2007, Boca Raton, London, New York: CRC Press.
65. Burke, E., J.Q. Broughton, and G.H. Gilmer, *Crystallization of fcc (111) and (100) crystal‐melt interfaces: A comparison by molecular dynamics for the Lennard‐Jones system.* Journal of Chemical Physics, 1988. **89**(2): p. 1030-1041, doi: 10.1063/1.455254.
66. Koop, T., B.P. Luo, U.M. Biermann, P.J. Crutzen, and T. Peter, *Freezing of HNO3/H2SO4/H2O solutions at stratospheric temperatures: Nucleation statistics and experiments.* Journal of Physical Chemistry, 1997. **101**(6): p. 1117-1133, doi: 10.1021/jp9626531.
67. Vali, G. and E.J. Stansbury, *Time-dependent characteristics of heterogeneous nucleation of ice.* Canadian Journal of Physics, 1966. **44**(3): p. 477-&, doi: 10.1139/p66-044.
68. Vali, G., *Quantitative Evaluation of Experimental Results an the Heterogeneous Freezing Nucleation of Supercooled Liquids.* Journal of the Atmospheric Sciences, 1971. **28**(3): p. 402-409, doi: 10.1175/1520-0469(1971)028<0402:qeoera>2.0.co;2.
69. Stöckel, P., I.M. Weidinger, H. Baumgärtel, and T. Leisner, *Rates of homogeneous ice nucleation in levitated H2O and D2O droplets.* Journal of Physical Chemistry, 2005. **109**(11): p. 2540-2546, doi: 10.1021/jp047665y.
70. Krämer, B., O. Hübner, H. Vortisch, L. Wöste, T. Leisner, M. Schwell, E. Rühl, and H. Baumgärtel, *Homogeneous nucleation rates of supercooled water measured in single levitated microdroplets.* Journal of Chemical Physics, 1999. **111**(14): p. 6521-6527, doi: 10.1063/1.479946.
71. Demott, P.J. and D.C. Rogers, *Freezing Nucleation Rates of Dilute-Solution Droplets Measured between -30 °C and -40 °C in Laboratory Simulations of Natural Clouds.* Journal of the Atmospheric Sciences, 1990. **47**(9): p. 1056-1064, doi: 10.1175/1520-0469(1990)047<1056:FNRODS>2.0.CO;2.
72. Taborek, P., *Nucleation in Emulsified Supercooled Water.* Physical Review B, 1985. **32**(9): p. 5902-5906, doi: 10.1103/PhysRevB.32.5902.
73. Butorin, G.T. and V.P. Skripov, *Crystallization in supercooled water.* Kristallografiya, 1972. **17**(2): p. 379-&, doi.
74. Wood, G.R. and A.G. Walton, *Homogeneous nucleation kinetics of ice from water.* Journal of Applied Physics, 1970. **41**(7): p. 3027-3036, doi: 10.1063/1.1659359.
75. Benz, S., K. Megahed, O. Möhler, H. Saathoff, R. Wagner, and U. Schurath, *T-dependent rate measurements of homogeneous ice nucleation in cloud droplets using a large atmospheric simulation chamber.* Journal of Photochemistry and Photobiology A: Chemistry, 2005. **176**(1-3): p. 208-217, doi: 10.1016/j.jphotochem.2005.08.026.

76. Stan, C.A., G.F. Schneider, S.S. Shevkoplyas, M. Hashimoto, M. Ibanescu, B.J. Wiley, and G.M. Whitesides, *A microfluidic apparatus for the study of ice nucleation in supercooled water drops.* Lab on a Chip, 2009. **9**(16): p. 2293-2305, doi: 10.1039/b906198c.
77. Duft, D. and T. Leisner, *Laboratory evidence for volume-dominated nucleation of ice in supercooled water microdroplets.* Atmos. Chem. Phys., 2004. **4**: p. 1997-2000, doi: 10.5194/acp-4-1997-2004.
78. Rzesanke, D., J. Nadolny, D. Duft, R. Müller, A. Kiselev, and T. Leisner, *On the role of surface charges for homogeneous freezing of supercooled water microdroplets.* Physical Chemistry Chemical Physics, 2012. **14**(26): p. 9359-9363, doi: 10.1039/c2cp23653b.
79. Ladino, L., O. Stetzer, F. Lüönd, A. Welti, and U. Lohmann, *Contact freezing experiments of kaolinite particles with cloud droplets.* Journal of Geophysical Research: Atmospheres, 2011. **116**(D22): p. D22202, doi: 10.1029/2011jd015727.
80. Hoyle, C.R., V. Pinti, A. Welti, B. Zobrist, C. Marcolli, B. Luo, Á. Höskuldsson, H.B. Mattsson, O. Stetzer, T. Thorsteinsson, G. Larsen, and T. Peter, *Ice nucleation properties of volcanic ash from Eyjafjallajökull.* Atmos. Chem. Phys., 2011. **11**(18): p. 9911-9926, doi: 10.5194/acp-11-9911-2011.
81. Earle, M.E., T. Kuhn, A.F. Khalizov, and J.J. Sloan, *Volume nucleation rates for homogeneous freezing in supercooled water microdroplets: results from a combined experimental and modelling approach.* Atmos. Chem. Phys., 2010. **10**(16): p. 7945-7961, doi: 10.5194/acp-10-7945-2010.
82. Wood, S.E., M.B. Baker, and B.D. Swanson, *Instrument for studies of homogeneous and heterogeneous ice nucleation in free-falling supercooled water droplets.* Review of Scientific Instruments, 2002. **73**(11): p. 3988-3996, doi: 10.1063/1.1511796
83. Djikaev, Y.S., A. Tabazadeh, P. Hamill, and H. Reiss, *Thermodynamic conditions for the surface-stimulated crystallization of atmospheric droplets.* Journal of Physical Chemistry, 2002. **106**(43): p. 10247-10253, doi: 10.1021/jp021044s.
84. Vrbka, L. and P. Jungwirth, *Homogeneous Freezing of Water Starts in the Subsurface.* Journal of Physical Chemistry, 2006. **110**(37): p. 18126-18129, doi: 10.1021/jp064021c.
85. Sun, C.Q., X. Zhang, J. Zhou, Y. Huang, Y. Zhou, and W. Zheng, *Density, Elasticity, and Stability Anomalies of Water Molecules with Fewer than Four Neighbors.* The Journal of Physical Chemistry Letters, 2013. **4**(15): p. 2565-2570, doi: 10.1021/jz401029z.
86. Kuhn, T., M.E. Earle, A.F. Khalizov, and J.J. Sloan, *Size dependence of volume and surface nucleation rates for homogeneous freezing of supercooled water droplets.* Atmos. Chem. Phys., 2011. **11**(6): p. 2853-2861, doi: 10.5194/acp-11-2853-2011.
87. Vali, G., *Nucleation terminology.* Journal of Aerosol Science, 1985. **16**(6): p. 575-576, doi: 10.1016/0021-8502(85)90009-6.
88. Kovács, T., F.C. Meldrum, and H.K. Christenson, *Crystal Nucleation without Supersaturation.* The Journal of Physical Chemistry Letters, 2012. **3**(12): p. 1602-1606, doi: 10.1021/jz300450g.
89. Zobrist, B., T. Koop, B.P. Luo, C. Marcolli, and T. Peter, *Heterogeneous ice nucleation rate coefficient of water droplets coated by a nonadecanol monolayer.* Journal of Physical Chemistry, 2007. **111**(5): p. 2149-2155, doi: 10.1021/jp066080w.
90. Durant, A.J. and R.A. Shaw, *Evaporation freezing by contact nucleation inside-out.* Geophys. Res. Lett., 2005. **32**(20): p. L20814, doi: 10.1029/2005gl024175.

91. Fornea, A.P., S.D. Brooks, J.B. Dooley, and A. Saha, *Heterogeneous freezing of ice on atmospheric aerosols containing ash, soot, and soil.* Journal of Geophysical Research: Atmospheres, 2009. **114**(D13): p. D13201, doi: 10.1029/2009jd011958.
92. Westbrook, C.D. and A.J. Illingworth, *Evidence that ice forms primarily in supercooled liquid clouds at temperatures > −27°C.* Geophys. Res. Lett., 2011. **38**(14): p. L14808, doi: 10.1029/2011gl048021.
93. de Boer, G., H. Morrison, M.D. Shupe, and R. Hildner, *Evidence of liquid dependent ice nucleation in high-latitude stratiform clouds from surface remote sensors.* Geophys. Res. Lett., 2011. **38**(1): p. L01803, doi: 10.1029/2010gl046016.
94. Prenni, A.J., P.J. Demott, D.C. Rogers, S.M. Kreidenweis, G.M. McFarquhar, and G. Zhang, *Ice nuclei characteristics from M-PACE and their relation to ice formation in clouds.* Tellus, 2009. **61**(2): p. 436–448, doi: 10.1111/j.1600-0889.2009.00415.x.
95. Ansmann, A., M. Tesche, P. Seifert, D. Althausen, R. Engelmann, J. Fruntke, U. Wandinger, I. Mattis, and D. Müller, *Evolution of the ice phase in tropical altocumulus: SAMUM lidar observations over Cape Verde.* Journal of Geophysical Research: Atmospheres, 2009. **114**(D17): p. D17208, doi: 10.1029/2008jd011659.
96. Field, P.R., O. Möhler, P. Connolly, M. Krämer, R. Cotton, A.J. Heymsfield, H. Saathoff, and M. Schnaiter, *Some ice nucleation characteristics of Asian and Saharan desert dust.* Atmos. Chem. Phys., 2006. **6**: p. 2991-3006, doi: 10.5194/acp-6-2991-2006.
97. Sassen, K. and V. Khvorostyanov, *Cloud effects from boreal forest fire smoke: evidence for ice nucleation from polarization lidar data and cloud model simulations.* Environmental Research Letters, 2008. **3**(2): p. 025006, doi: 10.1088/1748-9326/3/2/025006.
98. Ansmann, A., I. Mattis, D. Müller, U. Wandinger, M. Radlach, D. Althausen, and R. Damoah, *Ice formation in Saharan dust over central Europe observed with temperature/humidity/aerosol Raman lidar.* Journal of Geophysical Research: Atmospheres, 2005. **110**(D18): p. D18S12, doi: 10.1029/2004jd005000.
99. Hobbs, P.V. and A.L. Rangno, *Ice Particle Concentrations in Clouds.* Journal of the Atmospheric Sciences, 1985. **42**(23): p. 2523-2549, doi: 10.1175/1520-0469(1985)042<2523:ipcic>2.0.co;2.
100. Seifert, P., A. Ansmann, S. Groß, V. Freudenthaler, B. Heinold, A. Hiebsch, I. Mattis, J. Schmidt, F. Schnell, M. Tesche, U. Wandinger, and M. Wiegner, *Ice formation in ash-influenced clouds after the eruption of the Eyjafjallajökull volcano in April 2010.* Journal of Geophysical Research: Atmospheres, 2011. **116**(D20): p. D00U04, doi: 10.1029/2011jd015702.
101. Philips, V.T.J., L.J. Donner, and S.T. Garner, *Nucleation Processes in Deep Convection Simulated by a Cloud-System-Resolving Model with Double-Moment Bulk Microphysics.* Journal of the Atmospheric Sciences, 2007. **64**(3): p. 738-761, doi: 10.1175/jas3869.1.
102. Hoose, C., J.E. Kristjánsson, J.-P. Chen, and A. Hazra, *A Classical-Theory-Based Parameterization of Heterogeneous Ice Nucleation by Mineral Dust, Soot, and Biological Particles in a Global Climate Model.* Journal of the Atmospheric Sciences, 2010. **67**(8): p. 2483-2503, doi: 10.1175/2010jas3425.1.
103. Field, P.R., A.J. Heymsfield, B.J. Shipway, P.J. DeMott, K.A. Pratt, D.C. Rogers, J. Stith, and K.A. Prather, *Ice in Clouds Experiment–Layer Clouds. Part II: Testing Characteristics of Heterogeneous Ice Formation in Lee Wave Clouds.* Journal of the Atmospheric Sciences, 2011. **69**(3): p. 1066-1079, doi: 10.1175/jas-d-11-026.1.
104. Twohy, C.H., P.J. DeMott, K.A. Pratt, R. Subramanian, G.L. Kok, S.M. Murphy, T. Lersch, A.J. Heymsfield, Z. Wang, K.A. Prather, and J.H. Seinfeld, *Relationships of*

Biomass-Burning Aerosols to Ice in Orographic Wave Clouds. Journal of the Atmospheric Sciences, 2010. **67**(8): p. 2437-2450, doi: 10.1175/2010jas3310.1.

105. Morrison, H., M.D. Shupe, J.O. Pinto, and J.A. Curry, *Possible roles of ice nucleation mode and ice nuclei depletion in the extended lifetime of Arctic mixed-phase clouds.* Geophys. Res. Lett., 2005. **32**(18): p. L18801, doi: 10.1029/2005gl023614.
106. Hartmann, S., S. Augustin, T. Clauss, H. Wex, T. Šantl-Temkiv, J. Voigtländer, D. Niedermeier, and F. Stratmann, *Immersion freezing of ice nucleation active protein complexes.* Atmos. Chem. Phys., 2013. **13**(11): p. 5751-5766, doi: 10.5194/acp-13-5751-2013.
107. Atkinson, J.D., B.J. Murray, M.T. Woodhouse, T.F. Whale, K.J. Baustian, K.S. Carslaw, S. Dobbie, D. O'Sullivan, and T.L. Malkin, *The importance of feldspar for ice nucleation by mineral dust in mixed-phase clouds.* Nature, 2013. **498**(7454): p. 355-358, doi: 10.1038/nature12278.
108. Fletcher, N.H., *Size Effect in Heterogeneous Nucleation.* Journal of Chemical Physics, 1958. **29**(3): p. 572-576, doi: 10.1063/1.1744540.
109. Connolly, P.J., O. Möhler, P.R. Field, H. Saathoff, R. Burgess, T. Choularton, and M. Gallagher, *Studies of heterogeneous freezing by three different desert dust samples.* Atmos. Chem. Phys., 2009. **9**(8): p. 2805-2824, doi: 10.5194/acp-9-2805-2009.
110. Demott, P.J., *Quantitative Descriptions of Ice Formation Mechanisms of Silver Iodide-Type Aerosols.* Atmospheric Research, 1995. **38**(1-4): p. 63-99, doi: 10.1016/0169-8095(94)00088-U.
111. O'Sullivan, D., B.J. Murray, T.L. Malkin, T. Whale, N.S. Umo, J.D. Atkinson, H.C. Price, K.J. Baustian, J. Browse, and M.E. Webb, *Ice nucleation by soil dusts: relative importance of mineral dust and biogenic components.* Atmos. Chem. Phys. Discuss., 2013. **13**(8): p. 20275-20317, doi: 10.5194/acpd-13-20275-2013.
112. Vali, G., *Principles of Ice Nucleation*, in *Biological Ice Nucleation and Its Applications*, R. Lee Jr, Warren, G. J., and Gusta, L. V., Editor 1995, American Phytopathological Society: St. Paul, Mn, USA. p. 1-28.
113. Lindow, S.E., E. Lahue, A.G. Govindarajan, N.J. Panopoulos, and D. Gies, *Localization of Ice Nucleation Activity and the iceC Gene Product in Pseudomonas syringae and Escherichia coli.* Mol. Plant-Microbe Interact, 1989. **2**(5): p. 262-272, doi: 10.1094/MPMI-2-262.
114. Conen, F., C.E. Morris, J. Leifeld, M.V. Yakutin, and C. Alewell, *Biological residues define the ice nucleation properties of soil dust.* Atmos. Chem. Phys., 2011. **11**(18): p. 9643-9648, doi: 10.5194/acp-11-9643-2011.
115. DeMott, P.J., A.J. Prenni, X. Liu, S.M. Kreidenweis, M.D. Petters, C.H. Twohy, M.S. Richardson, T. Eidhammer, and D.C. Rogers, *Predicting global atmospheric ice nuclei distributions and their impacts on climate.* Proceedings of the National Academy of Sciences, USA, 2010. **107**(25): p. 11217-11222, doi: 10.1073/pnas.0910818107.
116. Spracklen, D.V., K.S. Carslaw, U. Pöschl, A. Rap, and P.M. Forster, *Global cloud condensation nuclei influenced by carbonaceous combustion aerosol.* Atmos. Chem. Phys., 2011. **11**(17): p. 9067-9087, doi: 10.5194/acp-11-9067-2011.
117. Kumai, M., *Electron-microscope study of snow-crystal nuclei.* Journal of Meteorology, 1951. **8**(3): p. 151-156, doi: 10.1175/1520-0469(1951)008<0151:emsosc>2.0.co;2.
118. Kumai, M., *Snow crystals and the identification of the nuclei in the northern United States of America.* Journal of Meteorology, 1961. **18**(2): p. 139-150, doi: 10.1175/1520-0469(1961)018<0139:scatio>2.0.co;2.

119. Isono, K., M. Komabayasi, and A. Ono, *The Nature and the Origin of Ice Nuclei in the .Atmosphere.* Journal of the Meteorological Society of Japan. Ser. II, 1959. **37**(6): p. 211-233, doi.

120. Cziczo, D.J., P.J. DeMott, C. Brock, P.K. Hudson, B. Jesse, S.M. Kreidenweis, A.J. Prenni, J. Schreiner, D.S. Thomson, and D.M. Murphy, *A method for single particle mass spectrometry of ice nuclei.* Aerosol Science and Technology, 2003. **37**(5): p. 460-470, doi: 10.1080/02786820300976.

121. Cziczo, D.J., P.J. DeMott, S.D. Brooks, A.J. Prenni, D.S. Thomson, D. Baumgardner, J.C. Wilson, S.M. Kreidenweis, and D.M. Murphy, *Observations of organic species and atmospheric ice formation.* Geophys. Res. Lett., 2004. **31**(12), doi: 10.1029/2004GL019822.

122. Cziczo, D.J., D.M. Murphy, P.K. Hudson, and D.S. Thomson, *Single particle measurements of the chemical composition of cirrus ice residue during CRYSTAL-FACE.* Journal of Geophysical Research, 2004. **109**(D4), doi: 10.1029/2003JD004032.

123. DeMott, P.J., D.J. Cziczo, A.J. Prenni, D.M. Murphy, S.M. Kreidenweis, D.S. Thomson, R. Borys, and D.C. Rogers, *Measurements of the concentration and composition of nuclei for cirrus formation.* Proceedings of the National Academy of Sciences of the United States of America, 2003. **100**(25): p. 14655-14660, doi: 10.1073/pnas.2532677100.

124. Seifert, A., C. Köhler, and K.D. Beheng, *Aerosol-cloud-precipitation effects over Germany as simulated by a convective-scale numerical weather prediction model.* Atmos. Chem. Phys., 2012. **12**(2): p. 709-725, doi: 10.5194/acp-12-709-2012.

125. Harrington, J.Y. and P.Q. Olsson, *On the potential influence of ice nuclei on surface-forced marine stratocumulus cloud dynamics.* Journal of Geophysical Research: Atmospheres, 2001. **106**(D21): p. 27473-27484, doi: 10.1029/2000jd000236.

126. Ovchinnikov, M., A. Korolev, and J. Fan, *Effects of ice number concentration on dynamics of a shallow mixed-phase stratiform cloud.* Journal of Geophysical Research: Atmospheres, 2011. **116**(D1): p. D00T06, doi: 10.1029/2011jd015888.

127. Storelvmo, T., C. Hoose, and P. Eriksson, *Global modeling of mixed-phase clouds: The albedo and lifetime effects of aerosols.* Journal of Geophysical Research: Atmospheres, 2011. **116**(D5): p. D05207, doi: 10.1029/2010jd014724.

128. Murray, B.J., S.L. Broadley, and G.J. Morris, *Supercooling of water droplets in jet aviation fuel.* Fuel, 2011. **90**(1): p. 433-435, doi: 10.1016/j.fuel.2010.08.018.

129. Hama, K. and K. Itoo, *Freezing of Supercooled Water-droplets.* Japan Meteorological Agency: Meteorological Research Institute, 1956. **7**, doi.

130. Morris, C.E., A. Wen, X. Xu, and Y.-B. Di, *Ice nucleation-active bacteria on Chinese cabbage in northern China: Population dynamics and characteristics and their possible role in storage decay.* Phytopathology, 1992. **82**(7): p. 739-746, doi: 10.1094/Phyto-82-739.

131. Koop, T., H.P. Ng, L.T. Molina, and M.J. Molina, *A new optical technique to study aerosol phase transitions: The nucleation of ice from H2SO4 aerosols.* Journal of Physical Chemistry, 1998. **102**(45): p. 8924-8931, doi: 10.1021/jp9828078.

132. Suzuki, S., A. Nakajima, N. Yoshida, M. Sakai, A. Hashimoto, Y. Kameshima, and K. Okada, *Freezing of water droplets on silicon surfaces coated with various silanes.* Chemical Physics Letters, 2007. **445**(1–3): p. 37-41, doi: 10.1016/j.cplett.2007.07.066.

133. Gurganus, C., A.B. Kostinski, and R.A. Shaw, *Fast Imaging of Freezing Drops: No Preference for Nucleation at the Contact Line.* The Journal of Physical Chemistry Letters, 2011. **2**(12): p. 1449-1454, doi: 10.1021/jz2004528.

134. Gurganus, C., A.B. Kostinski, and R.A. Shaw, *High-Speed Imaging of Freezing Drops: Still No Preference for the Contact Line.* Journal of Physical Chemistry, 2013. **117**(12): p. 6195-6200, doi: 10.1021/jp311832d.
135. Johnson, D.A. and J. Hallett, *Freezing and shattering of supercooled water drops.* Quarterly Journal of the Royal Meteorological Society, 1968. **94**(402): p. 468-482, doi: 10.1002/qj.49709440204.
136. Langham, E.J. and B.J. Mason, *The Heterogeneous and Homogeneous Nucleation of Supercooled Water.* Proceedings of the Royal Society of London. Series A, Mathematical and Physical Sciences, 1958. **247**(1251): p. 493-504, doi: 10.2307/100640.
137. Gay, M.J. and J. Latham, *The freezing behaviour of supercooled water drops.* Journal of Glaciology, 1976. **17**(75): p. 99-109, doi.
138. Whale, T.F., B.J. Murray, D. O'Sullivan, N.S. Umo, K.J. Baustian, J.D. Atkinson, and G.J. Morris, *A technique for quantifying rare heterogeneous ice nucleation events in supercooled water droplets.* In prep., 2013, doi.
139. Niedermeier, D., S. Hartmann, R.A. Shaw, D. Covert, T.F. Mentel, J. Schneider, L. Poulain, P. Reitz, C. Spindler, T. Clauss, A. Kiselev, E. Hallbauer, H. Wex, K. Mildenberger, and F. Stratmann, *Heterogeneous freezing of droplets with immersed mineral dust particles - measurements and parameterization.* Atmos. Chem. Phys., 2010. **10**(8): p. 3601-3614, doi: 10.5194/acp-10-3601-2010.
140. Pummer, B.G., H. Bauer, J. Bernardi, S. Bleicher, and H. Grothe, *Suspendable macromolecules are responsible for ice nucleation activity of birch and conifer pollen.* Atmos. Chem. Phys., 2012. **12**(5): p. 2541-2550, doi: 10.5194/acp-12-2541-2012.
141. Iannone, R., D.I. Chernoff, A. Pringle, S.T. Martin, and A.K. Bertram, *The ice nucleation ability of one of the most abundant types of fungal spores found in the atmosphere.* Atmos. Chem. Phys., 2011. **11**(3): p. 1191-1201, doi: 10.5194/acp-11-1191-2011.
142. Hukins, D.W.L., *X-ray Diffraction by Disordered and Ordered Systems* 1981, Oxford, UK: Pergamon Press Ltd.
143. Hillier, S., *Accurate quantitative analysis of clay and other minerals in sandstones by XRD: comparison of a Rietveld and a reference intensity ratio (RIR) method and the importance of sample preparation.* Clay Minerals, 2000. **35**(1): p. 291-302, doi.
144. Hillier, S., *Quantitative Analysis of Clay and other Minerals in Sandstones by X-Ray Powder Diffraction (XRPD)*, in *Clay Mineral Cements in Sandstones*, R.H. Worden and S. Morad, Editors. 2003, Blackwell Publishing Ltd. p. 213-251.
145. Data, I.C.f.D. *PDF-2*, 2009. [cited 2009]. Available from: http://www.icdd.com/.
146. Gregg, S.J. and K.S.W. Sing, *Adsorption, surface area, and porosity*. 2 ed., 1982, London, UK: Academic Press. 303.
147. Wu, Q., M. Borkovec, and H. Sticher, *On Particle-Size Distributions in Soils.* Soil Science Society of America Journal, 1993. **57**(4): p. 883-890, doi: 10.2136/sssaj1993.03615995005700040001x.
148. Deer, W.A., R.A. Howie, and J. Zussman, *An introduction to the rock forming minerals*. 2nd ed., 1992, Harlow, UK: Addison Wesley Longman.
149. Mason, B., *The Physics of Clouds* 1971, Oxford, UK: Clardendon Press.
150. Tabazadeh, A., Y.S. Djikaev, P. Hamill, and H. Reiss, *Laboratory evidence for surface nucleation of solid polar stratospheric cloud particles.* Journal of Physical Chemistry, 2002. **106**(43): p. 10238-10246, doi: 10.1021/jp021045k.
151. Djikaev, Y.S., A. Tabazadeh, and H. Reiss, *Thermodynamics of crystal nucleation in multicomponent droplets: Adsorption, dissociation, and surface-stimulated*

nucleation. Journal of Chemical Physics, 2003. **118**(14): p. 6572-6581, doi: 10.1063/1.1559034.

152. Tabazadeh, A., *Commentary on "Homogeneous nucleation of NAD and NAT in liquid stratospheric aerosols: insufficient to explain denitrification" by Knopf et al.* Atmos. Chem. Phys. Discuss., 2003. **3**(1): p. 827-833, doi: 10.5194/acpd-3-827-2003.
153. Hess, M., P. Koepke, and I. Schult, *Optical Properties of Aerosols and Clouds: The Software Package OPAC.* Bulletin of the American Meteorological Society, 1998. **79**(5): p. 831-844, doi: 10.1175/1520-0477(1998)079<0831:opoaac>2.0.co;2.
154. Miles, N.L., J. Verlinde, and E.E. Clothiaux, *Cloud Droplet Size Distributions in Low-Level Stratiform Clouds.* Journal of the Atmospheric Sciences, 2000. **57**(2): p. 295-311, doi: 10.1175/1520-0469(2000)057<0295:cdsdil>2.0.co;2.
155. Kärcher, B. and U. Lohmann, *A parameterization of cirrus cloud formation: Homogeneous freezing of supercooled aerosols.* Journal of Geophysical Research: Atmospheres, 2002. **107**(D2): p. AAC 4-1-AAC 4-10, doi: 10.1029/2001jd000470.
156. Koop, T., B.P. Luo, A. Tsias, and T. Peter, *Water activity as the determinant for homogeneous ice nucleation in aqueous solutions.* Nature, 2000. **406**(6796): p. 611-614, doi.
157. Ehre, D., E. Lavert, M. Lahav, and I. Lubomirsky, *Water Freezes Differently on Positively and Negatively Charged Surfaces of Pyroelectric Materials.* Science, 2010. **327**(5966): p. 672-675, doi: 10.1126/science.1178085.
158. Ginoux, P., J.M. Prospero, T.E. Gill, N.C. Hsu, and M. Zhao, *Global-scale attribution of anthropogenic and natural dust sources and their emission rates based on MODIS Deep Blue aerosol products.* Reviews of Geophysics, 2012. **50**(3): p. RG3005, doi: 10.1029/2012rg000388.
159. Prospero, J.M., P. Ginoux, O. Torres, S.E. Nicholson, and T.E. Gill, *Environmental characterization of global sources of atmospheric soil dust identified with the NIMBUS 7 Total Ozone Mapping Spectrometer (TOMS) absorbing aerosol product.* Rev. Geophys., 2002. **40**(1): p. 1002, doi: 10.1029/2000rg000095.
160. DeMott, P.J., K. Sassen, M.R. Poellot, D. Baumgardner, D.C. Rogers, S.D. Brooks, A.J. Prenni, and S.M. Kreidenweis, *African dust aerosols as atmospheric ice nuclei.* Geophys. Res. Lett., 2003. **30**(14): p. 1732, doi: 10.1029/2003GL017410.
161. Zimmermann, F., S. Weinbruch, L. Schütz, H. Hofmann, M. Ebert, K. Kandler, and A. Worringen, *Ice nucleation properties of the most abundant mineral dust phases.* Journal of Geophysical Research: Atmospheres, 2008. **113**(D23): p. D23204, doi: 10.1029/2008jd010655.
162. Prospero, J.M., J.E. Bullard, and R. Hodgkins, *High-Latitude Dust Over the North Atlantic: Inputs from Icelandic Proglacial Dust Storms*. Science, 2012. **335**(6072): p. 1078-1082, doi: 10.1126/science.1217447.
163. Pettijohn, F.J., *Sedimentary Rocks*. 3rd ed., 1975, New York: Harper & Row.
164. Marsham, J.H., P. Knippertz, N.S. Dixon, D.J. Parker, and G.M.S. Lister, *The importance of the representation of deep convection for modeled dust-generating winds over West Africa during summer.* Geophys. Res. Lett., 2011. **38**(16): p. L16803, doi: 10.1029/2011gl048368.
165. Zender, C.S., D. Newman, and O. Torres, *Spatial heterogeneity in aeolian erodibility: Uniform, topographic, geomorphic, and hydrologic hypotheses.* J. Geophys. Res., 2003. **108**(D17): p. 4543, doi: 10.1029/2002jd003039.
166. Prospero, J.M. and P.J. Lamb, *African Droughts and Dust Transport to the Caribbean: Climate Change Implications.* Science, 2003. **302**(5647): p. 1024-1027, doi: 10.1126/science.1089915.

167. Prospero, J.M. and D.L. Savoie. *Glory Science: GACP Datasets: Prospero and Savoie*, 2013. [cited 16/07/2013]. Available from: http://gacp.giss.nasa.gov/data_sets/Joseph_Prospero.html.
168. Woodward, S., *Modeling the atmospheric life cycle and radiative impact of mineral dust in the Hadley Centre climate model.* J. Geophys. Res., 2001. **106**(D16): p. 18155-18166, doi: 10.1029/2000jd900795.
169. Schepanski, K., I. Tegen, B. Laurent, B. Heinold, and A. Macke, *A new Saharan dust source activation frequency map derived from MSG-SEVIRI IR-channels.* Geophys. Res. Lett., 2007. **34**(18): p. L18803, doi: 10.1029/2007gl030168.
170. Knippertz, P. and M.C. Todd, *Mineral dust aerosols over the Sahara: Meteorological controls on emission and transport and implications for modeling.* Rev. Geophys., 2012. **50**(1): p. RG1007, doi: 10.1029/2011rg000362.
171. Mann, G.W., K.S. Carslaw, D.V. Spracklen, D.A. Ridley, P.T. Manktelow, M.P. Chipperfield, S.J. Pickering, and C.E. Johnson, *Description and evaluation of GLOMAP-mode: a modal global aerosol microphysics model for the UKCA composition-climate model.* Geosci. Model Dev., 2010. **3**(2): p. 519-551, doi: 10.5194/gmd-3-519-2010.
172. Glaccum, R.A. and J.M. Prospero, *Saharan aerosols over the tropical north-Atlantic - mineralogy.* Marine Geology, 1980. **37**(3-4): p. 295-321, doi: 10.1016/0025-3227(80)90107-3.
173. Prospero, J.M., R.A. Glaccum, and R.T. Nees, *Atmospheric transport of soil dust from Africa to South-America.* Nature, 1981. **289**(5798): p. 570-572, doi: 10.1038/289570a0.
174. Blank, M., M. Leinen, and J.M. Prospero, *Major Asian aeolian inputs indicated by the mineralogy of aerosols and sediments in the western North Pacific.* Nature, 1985. **314**(6006): p. 84-86, doi: 10.1038/314084a0.
175. Schütz, L. and M. Sebert, *Mineral aerosols and source identification.* Journal of Aerosol Science, 1987. **18**(1): p. 1-&, doi: 10.1016/0021-8502(87)90002-4.
176. Leinen, M., J.M. Prospero, E. Arnold, and M. Blank, *Mineralogy of aeolian dust reaching the north Pacific-Ocean. 1. Sampling and analysis.* J. Geophys. Res., 1994. **99**(D10): p. 21017-21023, doi: 10.1029/94jd01735.
177. Arnold, E., J. Merrill, M. Leinen, and J. King, *The effect of source area and atmospheric transport on mineral aerosol collected over the North Pacific Ocean.* Global and Planetary Change, 1998. **18**(3-4): p. 137-159, doi: 10.1016/S0921-8181(98)00013-7.
178. Jeong, G.Y., *Bulk and single-particle mineralogy of Asian dust and a comparison with its source soils.* J. Geophys. Res., 2008. **113**(D2): p. D02208, doi: 10.1029/2007jd008606.
179. Kandler, K., L. Schütz, C. Deutscher, M. Ebert, H. Hofmann, S. Jäckel, R. Jaenicke, P. Knippertz, K. Lieke, A. Massling, A. Petzold, A. Schladitz, B. Weinzierl, A. Wiedensohler, S. Zorn, and S. Weinbruch, *Size distribution, mass concentration, chemical and mineralogical composition and derived optical parameters of the boundary layer aerosol at Tinfou, Morocco, during SAMUM 2006.* Tellus, 2009. **61B**(1): p. 32-50, doi: 10.1111/j.1600-0889.2008.00385.x.
180. Kandler, K., L. Schütz, S. Jäckel, K. Lieke, C. Emmel, D. Müller-Ebert, M. Ebert, D. Scheuvens, A. Schladitz, B. Šegvić, A. Wiedensohler, and S. Weinbruch, *Ground-based off-line aerosol measurements at Praia, Cape Verde, during the Saharan Mineral Dust Experiment: microphysical properties and mineralogy.* Tellus, 2011. **63B**(4): p. 459-474, doi: 10.1111/j.1600-0889.2011.00546.x.
181. Díaz-Hernández, J.L., J.D. Martín-Ramos, and A. López-Galindo, *Quantitative analysis of mineral phases in atmospheric dust deposited in the south-eastern*

Iberian Peninsula. Atmospheric Environment, 2011. **45**(18): p. 3015-3024, doi: 10.1016/j.atmosenv.2011.03.024.

182. Meunier, A., *Clays* 2005, Berlin, Germany: Springer.
183. Borden, D. and R.F. Giese, *Baseline studies of The Clay Minerals Society Source Clays: Cation exchange capacity measurements by the ammonia-electrode method.* Clays and Clay Minerals, 2001. **49**(5): p. 444-445, doi: 10.1346/ccmn.2001.0490510.
184. Downs, R.T. and M. Hall-Wallace, *The American Mineralogist crystal structure database.* American Mineralogist, 2003. **88**(1): p. 247-250, doi.
185. Rickwood, P.C., *The largest crystals.* American Mineralogist, 1981. **66**(9): p. 885-907, doi.
186. Zoltai, T. and J.H. Stout, *Mineralogy: Concepts and Principles* 1984, Minneapolis, USA: Burgess Publishing Company.
187. Zhu, C., D.R. Veblen, A.E. Blum, and S.J. Chipera, *Naturally weathered feldspar surfaces in the Navajo Sandstone aquifer, Black Mesa, Arizona: Electron microscopic characterization.* Geochimica et Cosmochimica Acta, 2006. **70**(18): p. 4600-4616, doi: 10.1016/j.gca.2006.07.013.
188. Nugent, M.A., S.L. Brantley, C.G. Pantano, and P.A. Maurice, *The influence of natural mineral coatings on feldspar weathering.* Nature, 1998. **395**(6702): p. 588-591, doi: 10.1038/26951.
189. Welch, S.A. and W.J. Ullman, *The effect of organic acids on plagioclase dissolution rates and stoichiometry.* Geochimica et Cosmochimica Acta, 1993. **57**(12): p. 2725-2736, doi: 10.1016/0016-7037(93)90386-B.
190. Bouchelaghem, F., *A numerical and analytical study on calcite dissolution and gypsum precipitation.* Applied Mathematical Modelling, 2010. **34**(2): p. 467-480, doi: 10.1016/j.apm.2009.06.004.
191. Niedermeier, D., S. Hartmann, T. Clauss, H. Wex, A. Kiselev, R.C. Sullivan, P.J. DeMott, M.D. Petters, P. Reitz, J. Schneider, E. Mikhailov, B. Sierau, O. Stetzer, B. Reimann, U. Bundke, R.A. Shaw, A. Buchholz, T.F. Mentel, and F. Stratmann, *Experimental study of the role of physicochemical surface processing on the IN ability of mineral dust particles.* Atmos. Chem. Phys., 2011. **11**(21): p. 11131-11144, doi: 10.5194/acp-11-11131-2011.
192. Marcolli, C., S. Gedamke, T. Peter, and B. Zobrist, *Efficiency of immersion mode ice nucleation on surrogates of mineral dust.* Atmos. Chem. Phys., 2007. **7**: p. 5081-5091, doi: 10.5194/acp-7-5081-2007.
193. Chipera, S.J. and D.L. Bish, *Baseline studies of The Clay Minerals Society Source Clays: Powder X-ray diffraction analyses.* Clays and Clay Minerals, 2001. **49**(5): p. 398-409, doi: 10.1346/ccmn.2001.0490507.
194. Crawford, I., K.N. Bower, T.W. Choularton, C. Dearden, J. Crosier, C. Westbrook, G. Capes, H. Coe, P.J. Connolly, J.R. Dorsey, M.W. Gallagher, P. Williams, J. Trembath, Z. Cui, and A. Blyth, *Ice formation and development in aged, wintertime cumulus over the UK: observations and modelling.* Atmos. Chem. Phys., 2012. **12**(11): p. 4963-4985, doi: 10.5194/acp-12-4963-2012.
195. Hallett, J. and S.C. Mossop, *Production of secondary ice particles during the riming process.* Nature, 1974. **249**(5452): p. 26-28, doi: 10.1038/249026a0.
196. Nickovic, S., A. Vukovic, M. Vujadinovic, V. Djurdjevic, and G. Pejanovic, *Technical Note: High-resolution mineralogical database of dust-productive soils for atmospheric dust modeling.* Atmos. Chem. Phys., 2012. **12**(2): p. 845-855, doi: 10.5194/acp-12-845-2012.
197. Spracklen, D.V., K.J. Pringle, K.S. Carslaw, M.P. Chipperfield, and G.W. Mann, *A global off-line model of size-resolved aerosol microphysics: I. Model development*

and prediction of aerosol properties. Atmos. Chem. Phys., 2005. **5**(8): p. 2227-2252, doi: 10.5194/acp-5-2227-2005.

198. Arnold, S.R., M.P. Chipperfield, and M.A. Blitz, *A three-dimensional model study of the effect of new temperature-dependent quantum yields for acetone photolysis.* J. Geophys. Res., 2005. **110**(D22): p. D22305, doi: 10.1029/2005jd005998.
199. Shi, Z.B., M.T. Woodhouse, K.S. Carslaw, M.D. Krom, G.W. Mann, A.R. Baker, I. Savov, G.R. Fones, B. Brooks, N. Drake, T.D. Jickells, and L.G. Benning, *Minor effect of physical size sorting on iron solubility of transported mineral dust.* Atmos. Chem. Phys., 2011. **11**(16): p. 8459-8469, doi: 10.5194/acp-11-8459-2011.
200. Uppala, S.M., P.W. Kållberg, A.J. Simmons, U. Andrae, V. Da Costa Bechtold, M. Fiorino, J.K. Gibson, J. Haseler, A. Hernandez, G.A. Kelly, X. Li, K. Onogi, S. Saarinen, N. Sokka, R.P. Allan, E. Andersson, K. Arpe, M.A. Balmaseda, A.C.M. Beljaars, L.V.D. Berg, J. Bidlot, N. Bormann, S. Caires, F. Chevallier, A. Dethof, M. Dragosavac, M. Fisher, M. Fuentes, S. Hagemann, E. Hólm, B.J. Hoskins, L. Isaksen, P.A.E.M. Janssen, R. Jenne, A.P. McNally, J.F. Mahfouf, J.-J. Morcrette, N.A. Rayner, R.W. Saunders, P. Simon, A. Sterl, K.E. Trenberth, A. Untch, D. Vasiljevic, P. Viterbo, and J. Woollen, *The ERA-40 re-analysis.* Quarterly Journal of the Royal Meteorological Society, 2005. **131**(612): p. 2961-3012, doi: 10.1256/qj.04.176.
201. Dentener, F., S. Kinne, T. Bond, O. Boucher, J. Cofala, S. Generoso, P. Ginoux, S. Gong, J.J. Hoelzemann, A. Ito, L. Marelli, J.E. Penner, J.-P. Putaud, C. Textor, M. Schulz, G.R. van der Werf, and J. Wilson, *Emissions of primary aerosol and precursor gases in the years 2000 and 1750 prescribed data-sets for AeroCom.* Atmos. Chem. Phys., 2006. **6**(12): p. 4321-4344, doi: 10.5194/acp-6-4321-2006.
202. Claquin, T., M. Schulz, and Y.J. Balkanski, *Modeling the mineralogy of atmospheric dust sources.* J. Geophys. Res., 1999. **104**(D18): p. 22243-22256, doi: 10.1029/1999jd900416.
203. Jackson, M.L.R. and P. Barak, *Soil Chemical Analysis: Advanced Course* 2005: Parallel Press, University of Wisconsin-Madison Libraries. Page 105.
204. Choi, Y.-S., R.S. Lindzen, C.-H. Ho, and J. Kim, *Space observations of cold-cloud phase change.* Proceedings of the National Academy of Sciences, USA, 2010. **107**(25): p. 11211-11216, doi: 10.1073/pnas.1006241107.
205. Kanitz, T., P. Seifert, A. Ansmann, R. Engelmann, D. Althausen, C. Casiccia, and E.G. Rohwer, *Contrasting the impact of aerosols at northern and southern midlatitudes on heterogeneous ice formation.* Geophys. Res. Lett., 2011. **38**(17): p. L17802, doi: 10.1029/2011gl048532.
206. Bigg, E.K., *Ice Nucleus Concentrations in Remote Areas.* Journal of the Atmospheric Sciences, 1973. **30**(6): p. 1153-1157, doi: 10.1175/1520-0469(1973)030<1153:incira>2.0.co;2.
207. Rosinski, J., P.L. Haagenson, C.T. Nagamoto, and F. Parungo, *Nature of ice-forming nuclei in marine air masses.* Journal of Aerosol Science, 1987. **18**(3): p. 291-309, doi: 10.1016/0021-8502(87)90024-3.
208. Rosinski, J., C.T. Nagamoto, and M.Y. Zhou, *Ice-forming nuclei over the East China Sea.* Atmospheric Research, 1995. **36**(1–2): p. 95-105, doi: 10.1016/0169-8095(94)00029-D.
209. Schnell, R.C., *Ice Nuclei in Seawater, Fog Water and Marine Air off the Coast of Nova Scotia: Summer 1975.* Journal of the Atmospheric Sciences, 1977. **34**(8): p. 1299-1305, doi: 10.1175/1520-0469(1977)034<1299:inisfw>2.0.co;2.
210. Burrows, S.M., C. Hoose, U. Pöschl, and M.G. Lawrence, *Ice nuclei in marine air: biogenic particles or dust?* Atmos. Chem. Phys., 2013. **13**(1): p. 245-267, doi: 10.5194/acp-13-245-2013.

211. Sullivan, R.C., M.D. Petters, P.J. DeMott, S.M. Kreidenweis, H. Wex, D. Niedermeier, S. Hartmann, T. Clauss, F. Stratmann, P. Reitz, J. Schneider, and B. Sierau, *Irreversible loss of ice nucleation active sites in mineral dust particles caused by sulphuric acid condensation.* Atmos. Chem. Phys., 2010. **10**(23): p. 11471-11487, doi: 10.5194/acp-10-11471-2010.

212. Mahowald, N.M., S. Kloster, S. Engelstaedter, J.K. Moore, S. Mukhopadhyay, J.R. McConnell, S. Albani, S.C. Doney, A. Bhattacharya, M.A.J. Curran, M.G. Flanner, F.M. Hoffman, D.M. Lawrence, K. Lindsay, P.A. Mayewski, J. Neff, D. Rothenberg, E. Thomas, P.E. Thornton, and C.S. Zender, *Observed 20th century desert dust variability: impact on climate and biogeochemistry.* Atmos. Chem. Phys., 2010. **10**(22): p. 10875-10893, doi: 10.5194/acp-10-10875-2010.

213. Klüser, L., P. Kleiber, T. Holzer-Popp, and V.H. Grassian, *Desert dust observation from space – Application of measured mineral component infrared extinction spectra.* Atmospheric Environment, 2012. **54**(0): p. 419-427, doi: 10.1016/j.atmosenv.2012.02.011.

214. Popovitz-Biro, R., J.L. Wang, J. Majewski, E. Shavit, L. Leiserowitz, and M. Lahav, *Induced freezing of supercooled water into ice by self-assembled crystalline monolayers of amphiphilic alcohols at the air-water interface.* Journal of the American Chemical Society, 1994. **116**(4): p. 1179-1191, doi: 10.1021/ja00083a003.

215. Gavish, M., R. Popovitz-Biro, M. Lahav, and L. Leiserowitz, *Ice Nucleation by Alcohols Arranged in Monolayers at the Surface of Water Drops.* Science, 1990. **250**(4983): p. 973-975, doi: 10.2307/2878239.

216. Hu, X.L. and A. Michaelides, *Ice formation on kaolinite: Lattice match or amphoterism?* Surface Science, 2007. **601**(23): p. 5378-5381, doi: 10.1016/j.susc.2007.09.012.

217. Campbell, J.M., F.C. Meldrum, and H.K. Christenson, *Characterization of Preferred Crystal Nucleation Sites on Mica Surfaces.* Crystal Growth & Design, 2013. **13**(5): p. 1915-1925, doi: 10.1021/cg301715n.

218. Hu, X.L. and A. Michaelides, *Water on the hydroxylated (0 0 1) surface of kaolinite: From monomer adsorption to a flat 2D wetting layer.* Surface Science, 2008. **602**(4): p. 960-974, doi: 10.1016/j.susc.2007.12.032.

219. *Monitoring atmospheric composition & climate*, 2013. [cited 6/08/2013]. Available from: http://www.gmes-atmosphere.eu/.

220. Holdren Jr, G.R. and R.A. Berner, *Mechanism of feldspar weathering—I. Experimental studies.* Geochimica et Cosmochimica Acta, 1979. **43**(8): p. 1161-1171, doi: 10.1016/0016-7037(79)90109-1.